Advanced Beam Dynamics and Diagnostics Concepts for Laser-Plasma Accelerators

Dissertation

zur Erlangung des Doktorgrades
an der Fakultät für Mathematik, Informatik und Naturwissenschaften
Fachbereich Physik
der Universität Hamburg

vorgelegt von

Irene Dornmair

aus Tübingen

Hamburg
2017

Gutachter der Dissertation	Prof. Dr. Florian Grüner Dr. Klaus Flöttmann Prof. Dr. Kwang-Je Kim
Gutachter der Disputation	Prof. Dr. Robin Santra Prof. Dr. Florian Grüner Dr. Klaus Flöttmann Prof. Dr. Wolfgang Hillert Dr. Andreas R. Maier
Datum der Disputation	08. Mai 2017
Vorsitzender des Prüfungsausschusses	Prof. Dr. Robin Santra
Vorsitzender des Promotionsausschusses	Prof. Dr. Wolfgang Hansen
Dekan der Fakultät für Mathematik, Informatik und Naturwissenschaften	Prof. Dr. Heinrich Graener

Abstract

Laser-**P**lasma **A**ccelerators (LPAs) combine a multitude of unique features, which makes them very attractive as drivers for next generation brilliant light sources including compact X-ray free-electron lasers. They provide high accelerating gradients, thereby drastically shrinking the accelerator size, while at the same time the produced electron bunches are intrinsically as short as a few femtoseconds and carry high peak currents. LPA are subject of very active research, yet, the field currently faces the challenge of improving the beam quality, and achieving stable and well-controlled injection and acceleration. This thesis tackles this issue from three different sides. A novel longitudinal phase space diagnostics is proposed that employs the strong fields present in plasma wakefields to streak ultrashort electron bunches. This allows for a temporal resolution down to the attosecond range, enabling direct determination to the current profile and the slice energy spread, both crucial quantities for the performance of free-electron lasers. Furthermore, adiabatic matching sections at the plasma-vacuum boundary are investigated. These can drastically reduce the beam divergence and thereby relax the constraints on the subsequent beam optics. For externally injected beams, the matching sections could even provide the key technology that permits emittance conservation by increasing the matched beam size to a level achievable with currently available magnetic optics. Finally, a new method is studied that allows to modify the wakefield shape. To this end, the plasma density is periodically modulated. One possible application can be to remove the linearly correlated energy spread, or chirp, from the accelerated bunch, which is suspected of being responsible for the main part of the often large energy spread of plasma accelerated beams.

Zusammenfassung

Mehrere ihrer Eigenschaften machen Laser-Plasma Beschleuniger zu attraktiven Kandidaten, um die nächste Generation brillanter Lichtquellen, einschließlich kompakter Freie-Elektronen Laser zur Erzeugung hochintensiver Röntgenstrahlung, zu treiben. Sie können extrem große Beschleunigungsgradienten erzeugen, weshalb die Beschleunigerlänge teils um Größenordnungen verkürzt werden kann. Des Weiteren sind die erzeugten Elektronenbunche typischerweise nur einige Femtosekunden lang und weisen hohe Spitzenströme auf. Das Forschungsfeld rund um Laser-Plasma Beschleuniger ist zur Zeit mit der Herausforderung konfrontiert die Strahlqualität der erzeugten Elektronenbunche, sowie die Kontrolle über und die Stabilität der Injektion und der Beschleunigung zu verbessern. Diese Herausforderungen sind Gegenstand der vorliegenden Dissertation. Mithilfe der starken tansversalen Felder in Laser-Plasma Wakefields kann der longitudinale Phasenraum ultrakurzer Elektronenbunche diagnostiziert werden. Mit einer zeitlichen Auflösung bis in den Attosekundenbereich kann direkt das Stromprofil und der Slice Energy Spread gemessen werden, beides Größen, die entscheidend dafür sind, ob ein Freie-Elektronen Laser mit solchen Bunchen betrieben werden kann. Des Weiteren werden adiabatische Rampen an den Plasma-Vakuum-Übergängen untersucht. Diese reduzieren drastisch die Divergenz des Elektronenstrahls, was die Anforderungen an die folgenden magnetischen Optiken senkt. Gerade für extern injizierte Elektronenbunche könnten adiabatische Rampen sogar unabdingbar sein, um die Emittanz des Strahls zu erhalten, da sie die für die Injektion benötigte Strahlgröße überhaupt erst auf ein Niveau anheben, das mit der verfügbaren Strahloptik erreichbar ist. Drittens wird die Möglichkeit untersucht, die Form des Wakefields mittels periodischer Dichtemodulationen zu beeinflussen. Eine Anwendung hiervon ist die Beseitigung der linearen Korrelation des longitudinalen Phasenraums, welche häufig für den Hauptteil der großen Energiebreite von Laser-Plasma beschleunigten Elektronenbunchen verantwortlich gemacht wird.

Contents

1 Introduction

Laser-**P**lasma **A**ccelerators (LPA) have experienced a surge of popularity over the last decade, owing to their ability to provide accelerating gradients orders of magnitude higher than possible with conventional accelerator technology. Furthermore, electron beams created by LPA intrinsically exhibit bunch lengths of only a few femtoseconds [1, 2] while providing high peak currents. These features make them attractive as drivers for next generation brilliant X-ray sources [3–6], promising to shrink both size and cost of **F**ree-**E**lectron **L**asers (FEL) to a scale accessible to universities and smaller research institutes. The generation of undulator radiation of few-nm wavelength from LPA beams has already been demonstrated [7, 8].

In an LPA, a high power laser pulse is focused into a plasma target. In the most simple case the target can be a gas jet or a small volume filled with gas, and typically a low-Z gas like hydrogen or helium is used. Already the prepulses of the laser or the rising edge of the main pulse are sufficient to fully ionize these gas species, and the ponderomotive force of the main pulse pushes aside the plasma electrons. The resulting charge separation causes strong electric fields in both longitudinal and transverse direction. This wakefield, or wake, trails the laser pulse, which moves through the plasma at almost the speed of light in vacuum. A short introduction into the LPA physics relevant for this thesis is given in chapter 2.

Typically, electron bunches are created from the plasma background. In order to gain energy in the strong longitudinal fields of the wake, the bunches have to be fast enough to co-propagate with the wakefield, i.e., they have to be injected into the wake. The acceleration of electron bunches to GeV kinetic energies over few cm distances has been shown in several laboratories [9–11]. However, while the energy gain is indeed orders of magnitude higher than in conventional accelerators, so far LPA cannot compete with these in terms of beam quality. Mainly two properties differ significantly – the energy spread and the divergence. Among the reasons for this are the injection process, which is often of statistical nature and hard to control experimentally, but also the small length scale given by the plasma wavelength and the high fields present in the wakefield.

The injection process determines the initial phase space, and many approaches have been proposed to control this trapping of plasma electrons in the wakefield. In general, the aim is to trigger injection at a well-defined position in the plasma target, in order to create a bunch that is much shorter than the plasma wavelength. This can be achieved, for example, by introducing a density down ramp that reduces the phase velocity of the wake [12], by optical techniques using several laser pulses that can create a beat wave or locally enhance the wakefield [13–15], or also by ionization injection, i.e., by doping the low-Z gas with a high-Z species [16–20]. A different approach are hybrid accelerators where it is planned to inject ultrashort electron bunches from a conventional machine into a laser-driven plasma wakefield where they are boosted to higher energy [21–24]. This substitutes the internal injection process with a well controlled conventional accelerator, while at the same time retains the most appealing feature of LPA, the high accelerating gradients. Such an injection mechanism is referred to as external injection, as the bunch is not created in the plasma itself. Yet, the term external injection also includes electron beams from a previous LPA stage that are post-accelerated in another plasma target, like demonstrated recently [25].

The focus of this thesis lies on the improvement of beam quality in laser-plasma acceleration. To this end, three different aspects are considered. First, a new diagnostics concept is proposed to gain access to the longitudinal phase space of femtosecond electron bunches in order to improve the injection process. Second, adiabatic matching strategies are examined to increase the beam size and thereby reduce the beam divergence at the plasma to vacuum interfaces. Finally, a new approach to remove the correlated energy spread with the help of a modulated density target is investigated.

LPA beams typically exhibit a relative energy spread of several percent, although beams featuring a spread around $1 - 2\,\%$ have also been measured using colliding pulse injection [26] or density down ramp injection [27]. In order to optimize either the internal injection process or the externally injected bunch, it is essential to gain information on the longitudinal phase space. For example, from simulations and from the finite bunch length compared to the plasma wavelength, it can be expected that a large fraction of the measured projected energy spread is actually a longitudinally correlated energy spread. This would be a vital information for the design of LPA-driven FELs, as the crucial quantity for the FEL mechanism is the slice energy spread. Furthermore, even though the bunch length has been measured to be a few femtoseconds [1, 2], the peak current – another crucial parameter for the FEL design – is also unknown. However, gaining direct access to the longitudinal phase space of femtosecond electron bunches is very challenging. The best resolution achieved so far in a direct measurement is as low as 1 fs [28] at LCLS, and requires X-band transverse deflecting cavities of several meters length. Chapter 3 of this thesis presents a new concept how to achieve femtosecond or even attosecond resolution by applying plasma wakefields.

The large accelerating gradients present in plasma wakefields are accompanied by strong transverse fields that focus the trapped electron bunches to extremely small beam sizes. This causes highly divergent electron beams at the plasma-vacuum boundary, which is not only a challenge for the beam optics that capture the beams, but, in combination with the typically large energy spread, also leads to fast chromatic emittance growth in the drift after the plasma [29]. The divergence therefore has to be reduced before the extraction from the plasma. This is possible by tapering the focusing forces at the end of the plasma to adiabatically expand the beam size, and is discussed in chapter 4.

The last part of this thesis is concerned with a new approach to reduce the correlated energy spread of LPA beams. This is achieved by modulating the plasma density and thereby changing the effective accelerating field of the wake. The identification of a parameter set for demonstration and the limitations in terms of bunch charge are subject of chapter 5.

2 Introduction to Laser-Plasma Acceleration

This chapter shall briefly review the field of laser-plasma acceleration and provide the reader with the mathematical description of plasma wakefields needed for the subsequent chapters. For the linear wakefield regime, analytical equations describing the electromagnetic fields present in the wake are given. For the nonlinear regime, no closed analytical solution exists, and the arising fields are therefore described using Particle-In-Cell (PIC) simulations.

2.1 Plasma Properties

An ionized gas is called a plasma. The exact degree of ionization that marks the border between a partly ionized gas and a plasma is not strictly defined, though [30]. In this thesis, the word is used with the concept of a fully ionized gas in mind.

In this state of matter the electrons are not bound to the atoms and can move freely. Currents in the plasma or charge separation between electrons and ions can then cause long-range electromagnetic fields. The characteristic time scale of plasma responses is determined by the plasma frequency

$$\omega_p = \sqrt{\frac{ne^2}{m\epsilon_0}}\,, \tag{2.1}$$

where n is the plasma density in units of particles per volume, e the elementary charge, m the mass of the considered particle kind and ϵ_0 the vacuum permittivity. If a charge separation is introduced in the plasma the particles will start to oscillate at this frequency. The length scale associated with it is the plasma period $\lambda_p = 2\pi c/\omega_p$.

The plasma frequency connected to electrons is much larger than the one connected to protons or even to ions of larger atomic number due to the dependence on the particle mass. The response of the plasma electrons to a perturbation then is roughly a factor

of 43 faster than the response of protons. For laser-plasma acceleration the ion motion therefore is usually neglected and a static ion background is assumed.

Experimentally, the plasma for plasma acceleration experiments can be created in several ways. For laser-driven plasma acceleration, as discussed here, the prepulses of the driver laser suffice to create a plasma. Typically, these laser systems provide a peak intensity around or above the intensity where the plasma electron motion becomes relativistic within one laser oscillation at $\sim 10^{18}\,\mathrm{W/cm^2}$. The ionization threshold of gases, however, is four orders of magnitude below this value at an intensity of $\sim 10^{14}\,\mathrm{W/cm^2}$.
Especially in beam driven plasma acceleration, the use of a dedicated ionization laser is an option, since the driver beam does not sufficiently ionize gas. Plasma can also be created by an electrical discharge that is pulsed through a gas capillary. This offers the possibility to form a plasma channel that counteracts laser diffraction (see e.g. [31, 9]).

2.2 Ponderomotive Force

The origin of the plasma wakefield excitation is the so-called ponderomotive force, which is present in tightly focused, short, high power laser pulses.
A charged particle in a plane electromagnetic wave of frequency ω is subject to the Lorentz force and will oscillate around its rest position. If there is a gradient present in the intensity of the wave, the ponderomotive force arises. In one half-period of the wave the particle is deflected to a region of lower intensity, and the restoring force is too small to compensate the complete deflection in the other half-period. Consequently, the particle drifts towards the region of lower intensity while oscillating. In LPA one typically is not interested in the particle oscillation. It is then convenient to describe the interaction of the laser with the plasma not with the exact Lorentz force but with the ponderomotive force (see e.g. [32])

$$F_p = -\frac{e}{4m_e\omega}\nabla E^2 = -m_e c^2 \nabla \frac{a^2}{2}, \tag{2.2}$$

that gives the force after averaging over one oscillation period and causes the drift motion. a is the normalized vector potential $a = eA/m_e c^2$ of the wave.

Due to the ponderomotive force the short laser pulse pushes plasma electrons longitudinally and transversely away from their rest position. The induced charge separation gives rise to large electric fields that cause the electrons to oscillate at the scale of the plasma period. A wakefield is excited in the plasma.

Wakefields can also be driven by particle beams. There, the wakefield is excited not by the ponderomotive force but directly by the Lorentz force, i.e., by the electric and magnetic field of the driver bunch.

2.3 Linear Wakefield Regime

In the linear wakefield regime, the peak normalized vector potential of the laser a_0 fulfills $a_0^2 \ll 1$, and the electrostatic potential of the wake can be derived (see e.g. [32, 33]) using the cold fluid equations. These are the continuity equation, eq. (2.3), that ensures particle conservation, the fluid momentum equation, eq. (2.4), that accounts for changes of momentum owed to the electrostatic force and the ponderomotive force, and Poisson's equation, eq. (2.5), that describes the electrostatic potential created by the charge density,

$$\frac{\partial}{\partial t}\delta n + n_0 \nabla \vec{u} = 0, \tag{2.3}$$

$$\frac{1}{c^2}\frac{\partial}{\partial t}\vec{u} = \nabla\phi - \nabla\frac{a^2}{2}, \tag{2.4}$$

$$\nabla^2\phi = k_p^2\frac{\delta n}{n_0}, \tag{2.5}$$

with $\delta n/n_0 = (n - n_0)/n_0$ the normalized density perturbation, $\vec{u} = \vec{p}/(m_e c)$ the normalized momentum, and $k_p = 2\pi/\lambda_p$ the plasma wave number. $\phi = \Phi e/(m_e c^2)$ is the normalized electrostatic potential of the wake. By eliminating $\vec{u}$ and $\delta n/n_0$ an equation for the electrostatic potential of the wakefield is obtained as

$$\left(\frac{\partial^2}{\partial t^2} + \omega_p^2\right)\phi = \omega_p^2\frac{a^2}{2}. \tag{2.6}$$

Assuming the wakefield driver moving in the z-direction, the solution for the normalized electrostatic potential can be found as

$$\phi = k_p/2\int_{\zeta_0}^{\zeta} \sin\left[k_p(\zeta - \zeta')\right]a^2(x, y, \zeta')\mathrm{d}\zeta'. \tag{2.7}$$

Here, a transformation to the co-moving frame with $\zeta = z - ct$ has been performed. In the quasi-static approximation the laser pulse is assumed to vary only slowly with time, so that the derivative with respect to time can be neglected with $\partial/\partial z = \partial/\partial\zeta$ (see for example [34, 35]). In the integration, ζ_0 is a position far in front of the laser where a^2 is still zero.

For a laser pulse of Gaussian shape in all dimensions $a^2(x, y, \zeta)$ is given by

$$a^2(x, y, \zeta) = a_0^2 \exp\left(-\frac{2r^2}{w_0^2}\right) \exp\left(-\frac{\zeta^2}{2\sigma_{z,l}^2}\right), \tag{2.8}$$

where $w_0/2$ denotes the transverse rms width and $\sigma_{z,l}$ denotes the longitudinal rms width of the intensity, and $r^2 = x^2 + y^2$. This expression is valid for a circularly polarized laser pulse. Since a_0 is defined via the vector potential and consequently the electric field amplitude of the laser, a linearly polarized laser of same a_0 as a circularly polarized laser has only half the intensity. The right hand side of equation (2.8) is therefore divided by 2 for a linearly polarized laser, which will be done from now on.

For positions ζ where a^2 is again zero, that is far behind the laser, the integration in eq. (2.7) can be performed within the limits from ∞ to $-\infty$ and solved to

$$\Phi = -\frac{a_0^2 k_p m_e c^2 \sigma_{z,l}}{2e} \sqrt{\frac{\pi}{2}} \exp\left(-\frac{k_p^2 \sigma_{z,l}^2}{2}\right) \exp\left(-\frac{2r^2}{w_0^2}\right) \sin(k_p \zeta). \tag{2.9}$$

The electric fields present in the laser-driven wakefield are given by $\vec{E} = -\nabla\Phi$ as

$$E_z(x, y, \zeta) = \frac{a_0^2 k_p^2 m_e c^2 \sigma_{z,l}}{2e} \sqrt{\frac{\pi}{2}} \exp\left(-\frac{k_p^2 \sigma_{z,l}^2}{2} - \frac{2r^2}{w_0^2}\right) \cos(k_p \zeta), \tag{2.10}$$

$$E_x(x, y, \zeta) = -x \frac{2a_0^2 k_p m_e c^2 \sigma_{z,l}}{e w_0^2} \sqrt{\frac{\pi}{2}} \exp\left(-\frac{k_p^2 \sigma_{z,l}^2}{2} - \frac{2r^2}{w_0^2}\right) \sin(k_p \zeta), \tag{2.11}$$

$$E_y(x, y, \zeta) = -y \frac{2a_0^2 k_p m_e c^2 \sigma_{z,l}}{e w_0^2} \sqrt{\frac{\pi}{2}} \exp\left(-\frac{k_p^2 \sigma_{z,l}^2}{2} - \frac{2r^2}{w_0^2}\right) \sin(k_p \zeta). \tag{2.12}$$

The electric fields in the linear wake scale directly proportional to the laser intensity, or to a_0^2, since they are caused by the ponderomotive force, which also scales with the intensity, or a_0^2. A numerical solution of eq. (2.7) showing the electric field components can be found in fig. 2.1. The accelerating field E_z is shifted by $\pi/2$ with respect to the focusing field $\partial_r E_r$. For stable beam transport, however, the beam needs to be placed in the constant focusing region. This implies positioning the beam at the slope of the longitudinal field E_z, which leads to a correlated energy spread (chirp) due to the finite bunch length compared to the plasma wavelength.

The linear regime is valid for $a_0^2 \ll 1$. In the quasi-linear regime, i.e., for a_0^2 near 1, the relativistic correction $a_0^2 \to a_0^2 \left(1 + a_0^2/2\right)^{-1/2}$ can be used to correct the wakefield amplitude. The laser-driven linear wakefield is purely electrostatic to order a_0^2. The magnetic field appears only for fourth order of a_0 [36] and is small compared to the electric fields, as $a_0^2 \ll 1$.

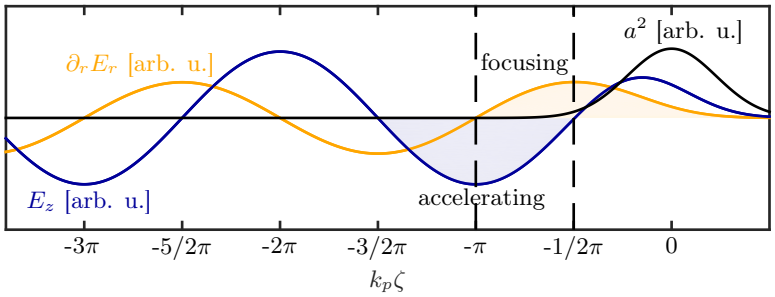

Figure 2.1 – Electric fields present in a laser-driven linear wakefield, calculated from eq. (2.7). The accelerating field E_z and the focusing field $\partial_r E_r$ are given on axis ($r = 0$). The focusing area (shaded yellow) overlaps only partially with the accelerating region in the wake (shaded blue).

Beam-Driven Linear Wakefield

Beam drivers of peak density n_{b0} lower than the plasma density ($n_{b0}/n_0 \ll 1$) excite a wakefield of similar shape as the laser-driven linear wake. The beam shape is defined analogously to the laser shape as

$$n_b(x, y, z) = n_{b0} \exp\left(-\frac{r^2}{2\sigma_r^2}\right) \exp\left(-\frac{z^2}{2\sigma_z^2}\right). \tag{2.13}$$

For a wide ($k_p\sigma_r \gg 1$) Gaussian driver situated at $\zeta = 0$, the wakefield far behind the driver is given as [37]

$$E_z(x, y, \zeta) = \frac{\sqrt{2\pi}\, n_{b0} k_p^2 m_e c^2 \sigma_z}{e n_0} \exp\left(-\frac{k_p^2\sigma_z^2}{2} - \frac{r^2}{2\sigma_r^2}\right) \cos(k_p\zeta), \tag{2.14}$$

$$(E_x - cB_y)(x, y, \zeta) = -x\frac{\sqrt{2\pi}\, n_{b0} k_p m_e c^2 \sigma_z}{e n_0 \sigma_r^2} \exp\left(-\frac{k_p^2\sigma_z^2}{2} - \frac{r^2}{2\sigma_r^2}\right) \sin(k_p\zeta), \tag{2.15}$$

and $E_y + cB_x$ analogously. In contrast to the laser-driven wake, here a significant magnetic field is present that is excited by the current of the driver beam.

2.4 Nonlinear Wakefield Regime

For high laser intensity, $a_0^2 \gtrsim 1$, the wakefield enters the so-called nonlinear regime. Here, an analytical description exists only in one dimension. In this regime, the plasma

electrons gain relativistic velocities during their interaction with the laser pulse. The fluid momentum equation then modifies to [38]

$$\frac{1}{c}\frac{\mathrm{d}(\gamma\beta_z)}{\mathrm{dt}} = \frac{\partial\phi}{\partial z} - \frac{1}{\gamma}\frac{\partial}{\partial z}\frac{a^2}{2}, \tag{2.16}$$

which is nonlinear in the sense that the relativistic Lorentz factor γ appears in the denominator on the right hand side. $\beta_z c$ is the longitudinal velocity component of the plasma electrons. One can derive Poisson's equation [32]

$$k_p^{-2}\frac{\partial^2\phi}{\partial\zeta^2} = \gamma_p^2\left\{\beta_p\left[1 - \frac{(1+a^2)^2}{\gamma_p^2(1+\phi)^2}\right]^{-1/2} - 1\right\}, \tag{2.17}$$

where $\beta_p = v_p/c$ is the normalized phase velocity of the plasma wake, and γ_p is the corresponding relativistic Lorentz factor.

The analytical treatment is purely one-dimensional, which means that it assumes an infinitely broad uniform plasma density and driver laser. In reality, the driver is a tightly focused high power laser, and three dimensional effects cannot be neglected. To analyze this one has to resort to PIC simulations.

In contrast to the linear regime where the plasma wake is a sinusoidal oscillation, the density maxima are much larger and narrower in the nonlinear regime, which causes a saw-tooth-like accelerating field. Apart from this steepening of the plasma wake, one significant difference between the linear and the nonlinear regime is the curvature of the wave fronts. In the linear regime, the plasma wavelength is everywhere the same and therefore the wave fronts are flat. In the nonlinear regime the plasma wavelength is elongated as the plasma electrons gain relativistic energies in the laser. For a Gaussian laser pulse the intensity is lower off-axis, and therefore also the nonlinear plasma wavelength is shorter there. This causes a curvature of the wave fronts that increases further behind the driver.

For sufficiently high laser intensity and small laser spot size ($a_0^2/(1+a_0^2)^{1/2} \geq k_p^2 w_0^2/4$ [32]), the so-called bubble regime is accessed. Here, all plasma electrons are expelled from the region behind the driver, and a nearly spherical ion cavity is formed. The electromagnetic fields can then be approximated as those of a homogeneously charged sphere moving at almost the speed of light, and the longitudinal field E_z is independent of r and linear in ζ in the bubble, while the focusing fields are independent of ζ and linear in r [32].

For illustration, a PIC simulation of a nonlinear wakefield using WARP [39] in 2D can be seen in figure 2.2. The laser parameters are $w_0 = 18\,\mu$m, $a_0 = 2.0$, and $\tau = 25\,$fs (FWHM), and the plasma density is $n = 3\cdot10^{18}\,\mathrm{cm}^{-3}$. The curvature of the wave fronts

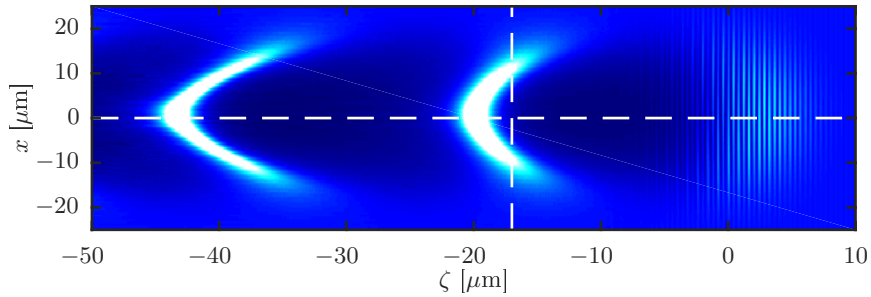

(a) Plasma density (arb. u.).

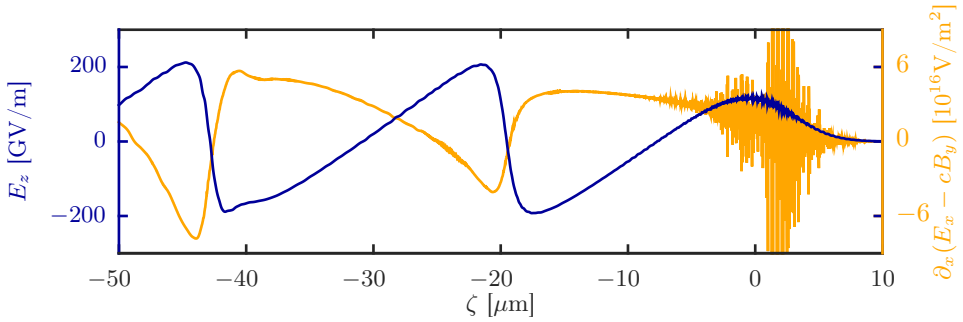

(b) Longitudinal field lineout.

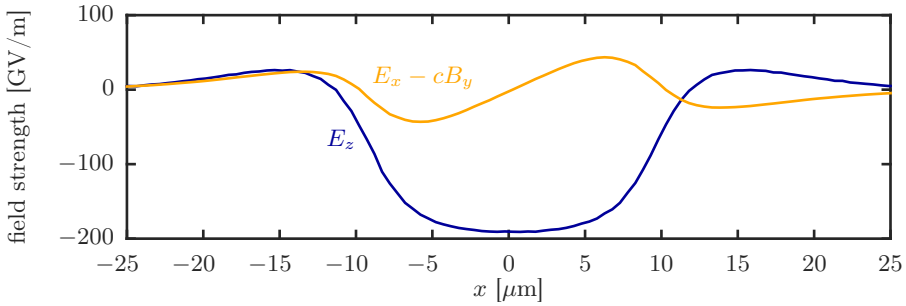

(c) Transverse field lineout.

Figure 2.2 – 2D PIC simulation with WARP of a nonlinear laser wakefield. Laser parameters are $w_0 = 18\,\mu$m, $a_0 = 2.0$, $\tau = 25\,$fs (FWHM), with a plasma density of $n = 3 \cdot 10^{18}\,\mathrm{cm}^{-3}$.

is clearly visible in the density. Lineouts of the electromagnetic fields along the white lines indicated in 2.2(a) can be found in (b) and (c). With $k_p^2 w_0^2/4 = 8.8$ the laser intensity here is not large enough to access the bubble regime. The fields, however, already exhibit some features of this regime. The accelerating field is of saw-tooth-like shape, while the focusing fields are nearly constant along ζ in the first bucket. Also, as shown in fig. 2.2(c), the accelerating field does not change significantly transversely near the axis, and the focusing forces are linear there.

2.5 Description of the electron beam

Throughout this thesis, the Courant-Snyder parameters [40] are used to describe the electron beam, and are therefore defined here for reference. The Courant-Snyder parameters are given by

$$\alpha_{\mathrm{CS}} = -\frac{\langle x x' \rangle}{\epsilon_{\mathrm{tr},x}}, \quad \beta_{\mathrm{CS}} = \frac{\langle x^2 \rangle}{\epsilon_{\mathrm{tr},x}}, \quad \text{and } \gamma_{\mathrm{CS}} = \frac{\langle x'^2 \rangle}{\epsilon_{\mathrm{tr},x}}, \tag{2.18}$$

with the geometric trace space emittance $\epsilon_{\mathrm{tr},x}$ defined as

$$\epsilon_{\mathrm{tr},x} = \sqrt{\langle x^2 \rangle \langle x'^2 \rangle - \langle x x' \rangle^2}. \tag{2.19}$$

For an ensemble of discrete particles, the angular brackets to denote the second central moment according to

$$\langle x x' \rangle = \frac{\sum_{i=1}^{n} x_i x_i'}{n} - \frac{\sum_{i=1}^{n} x_i \sum_{i=1}^{n} x_i'}{n^2}, \tag{2.20}$$

with the sum over all n particles of the bunch.

For simplicity, only the x-coordinate is shown here. The same parameters can of course also be defined for the y-plane. The beta function β_{CS} is a measure for the beam size, while α_{CS} correlates the particle coordinates with their slope and is zero in the electron focus. γ_{CS} can be expressed through the other two parameters as $\gamma_{\mathrm{CS}} = (1 + \alpha_{\mathrm{CS}}^2)\beta_{\mathrm{CS}}^{-1}$.

Of particular importance in the context of this work is the phase advance. It can be calculated from the beta function as (see e.g. [41])

$$\psi(z) = \int_0^z \frac{1}{\beta_{\mathrm{CS}}(z')} \, \mathrm{d}z'. \tag{2.21}$$

In a heuristic way of speaking, the phase advance describes the change of angle a particle undergoes in the trace space over a propagation distance z. Yet, this can be

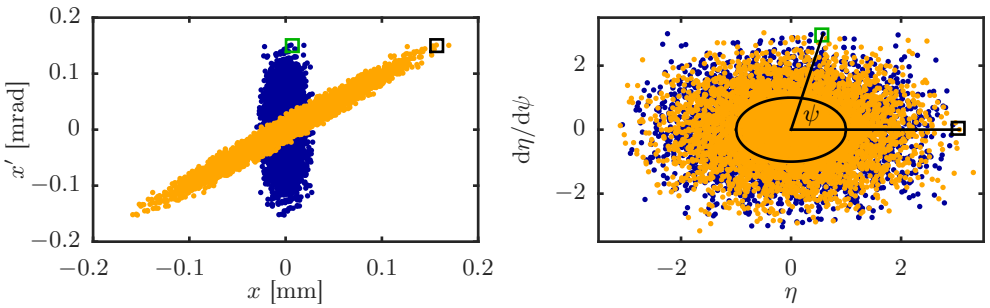

(a) Trace space.

(b) Transformed space.

Figure 2.3 – Beam in trace space and in transformed coordinates. Initially in focus (blue) the bunch propagates for 1 m (yellow) in a free drift. The phase advance amounting to $\psi = 78°$ corresponds to the angle described by a particle in Floquet coordinates. The circle of radius 1 (black) includes the particles in ± one standard deviation in both η and $\mathrm{d}\eta/\mathrm{d}\psi$ and indicates the beam emittance.

deceiving, as in trace space also the beam ellipse as a whole undergoes shearing or rotation. In contrast, the phase advance does not refer to the angle of the complete beam trace space, but to the angle of a single particle or feature in the beam. For example, after the propagation through a suitable beam optics, the phase space orientation can be the same as before, but a certain particle ends up at a different angle. In order to eliminate the movement of the complete bunch, the coordinates x and x' have to be transformed to the so-called Floquet coordinates via

$$\eta = \frac{x}{\sqrt{\epsilon_{\mathrm{tr},x}\beta_{\mathrm{CS}}}}, \tag{2.22}$$

$$\frac{\mathrm{d}\eta}{\mathrm{d}\psi} = \alpha_{\mathrm{CS}}\frac{x}{\sqrt{\epsilon_{\mathrm{tr},x}\beta_{\mathrm{CS}}}} + \sqrt{\frac{\beta_{\mathrm{CS}}}{\epsilon_{\mathrm{tr},x}}}\,x'. \tag{2.23}$$

Here, the coordinates are normalized by the square root of the emittance to achieve a standard deviation of 1 in η and in $\mathrm{d}\eta/\mathrm{d}\psi$. The change of angle in these transformed coordinates then indicates the phase advance. Details can be found for example in [41]. As an illustration, the simulation of a beam in a free drift is shown in figure 2.3. Initially, the beam is in focus (blue) with $\sigma_x = 10\,\mu\mathrm{m}$ and $\sigma_{x'} = 50\,\mu\mathrm{rad}$. The drift is 1 m long, and the phase advance amounts to $\psi = 78°$ over this distance. In the transformed coordinates, the phase advance can be identified as the angle described by an exemplary particle of the bunch.

Generally, especially the case of a phase advance of multiples of 90° is relevant. For example in electron diffraction experiments or when streaking the bunch as in chapter 3, the relevant information is encoded in the change of particle momentum. The aim is therefore to translate the momentum into a pure change of position at the detector. The transverse phase space then needs to be rotated by 90°, so that information previously encoded in the x' (or momentum) coordinate is transferred to the x (or space) coordinate.
Another example would be **T**ransmission **E**lectron **M**icroscopy (TEM), where a low energy electron beam is focused on a very thin sample that absorbs or strongly scatters part of the electrons. From the amount of particles passing straight through the sample one can deduce the sample thickness or material at different (transverse) positions in the sample. Only those electrons are diagnosed that pass the sample unaffected, and the relevant information therefore is encoded in the space coordinate. The phase advance between the sample and the detector then needs to be 180°, so that the x coordinate is again transferred into x.
In both cases it is also allowed to add multiples of 180° to the required phase advance, as this would only flip the phase space.

3 Ultrashort Bunch Diagnostics

The characteristic length scale in laser-plasma accelerators is the plasma wavelength. It determines the length of the phase interval of the plasma wakefield that can be used to accelerate beams, and consequently it is a measure for the produced bunch length. In internal injection experiments, λ_p is typically around 10 to 30 μm since a comparably high plasma density is favorable to trigger internal injection. Electron bunches that are created from the plasma background, be it by wavebreaking or other methods such as down ramp or colliding pulse injection, will be a fraction of the plasma wavelength long. Using coherent transition radiation [1] or Faraday rotation induced by the bunch in plasma [2] the bunch length has been measured to be around 1.4 fs and 2.5 fs rms, respectively.

The same condition needs to be fulfilled by an electron bunch injected externally into a wakefield. In order to minimize the accumulated energy spread from the slope or curvature of the accelerating field the bunch length needs to be much shorter than the plasma wavelength.

One major goal in the field of LPA is to drive a **F**ree-**E**lectron **L**aser (FEL) with plasma-accelerated electron bunches. These bunches are either created and accelerated directly in the plasma, or they could also be created and pre-accelerated in a conventional machine and then boosted to higher energy in a plasma stage. This second, hybrid option comes at the cost of a challenging synchronization and stabilization system to lock the driver laser to the conventional accelerator. Yet, it combines the best of both worlds, a well-controlled and characterized beam from a conventional machine, and the large accelerating gradients achievable in a plasma wakefield. Whichever the method of acceleration, the performance of an FEL depends crucially on the electron bunch parameters, especially on the slice energy spread and on the current profile. It is therefore of utmost interest to precisely know these parameters in order to optimize them, for internally injected beams after the plasma or for external injection also the parameters of the beam at the plasma position before injection.

Measuring the bunch length or even the current profile of ultra-short electron bunches is extremely challenging. The temporal resolution achievable with electro-optical monitors is limited to around 50 fs [42, 43]. Another established method is the measurement

of coherent transition radiation. Here, the beam passes through a thin foil and emits radiation. The bunch length can be extracted from the spectrum as it determines the onset of coherence. The current profile influences the shape of the spectrum. However, since the phase information is lacking, no unique solution for the bunch shape exists [1, 44]. Recently, the use of passive corrugated waveguides has been proposed and demonstrated in a proof of principle experiment [45]. The resolution can theoretically be in the femto- or even attosecond range, yet this requires meter long structures.

In conventional accelerators, the longitudinal phase space is usually measured with a **T**ransverse **D**eflecting **S**tructure (TDS) [46, 47]. The TDS maps the time information into the easily detectable transverse beam profile. In such a cavity, a mode is excited that imprints a time-dependent transverse momentum change on the electron bunch. In an imaging optics or a drift after the TDS, this transverse momentum is translated into a transverse position change. A resolution down to 1 fs has been demonstrated [28]. The achievable time resolution depends on the transverse field gradient and on the structure length. Since the field gradient is ultimately limited by RF technology, these devices can be several meters long [48, 49].

This chapter is concerned with a new technique that uses the large field gradients present in a laser-driven plasma wakefield to diagnose the longitudinal phase space of ultrashort bunches. Similar to the TDS, a transverse momentum change is imprinted that depends on the longitudinal position within the bunch. However, owed to the large electric fields and short plasma wavelength, the plasma target can be much shorter than a TDS structure and provide similar or even better temporal resolution. The reduced size is of advantage in compact accelerators like LPA, but it also reduces other detrimental effects inherent to TDS cavities that scale with the structure length, such as the induced beam offset and the accumulated energy chirp [50]. This technique requires a high-power laser system and a plasma target, tools that are needed for LPA in any case. For external injection, it could even provide an on-target bunch diagnostics without additional experimental equipment needed as the very same laser pulse could be used that otherwise drives the booster plasma stage.

Parts of this chapter have been published in [51].

3.1 Theory of Transverse Deflecting Structures

The theoretical basics of the transverse deflecting plasma (TDP) stage are similar to those of the TDS which will therefore be reviewed following refs. [50, 52].

The transverse momentum change imprinted by the structure can be written as

$$p_y(\xi) = \frac{eV}{c} \sin(k\xi + \Psi_0), \tag{3.1}$$

where k is the wave number, Ψ_0 is the average phase of the bunch in the field, and ξ is the longitudinal internal bunch coordinate. The effective voltage V is given by the integral of the amplitude of the deflecting fields over the length l of the structure,

$$V = \int_0^l E_{y0}(z) + cB_{x0}(z)\,\mathrm{dz}. \tag{3.2}$$

It is desirable that the bunch is placed at or near the zero-crossing of the integrated fields, so that the bunch does not gain a net angle, and that the momentum change is nearly linear along the internal bunch coordinate ξ. Therefore the phase is chosen as $\Psi_0 = 0$ in the following.

The slope of the transverse momentum change per unit length normalized to the beam momentum gives the shear parameter

$$S = \frac{1}{p_z}\frac{\partial p_y}{\partial \xi} = \frac{ekV}{cp_z}, \tag{3.3}$$

which represents the introduced angle per unit length. A feature in the longitudinal phase space can be resolved if the introduced angle over the feature size $\Delta\xi$ is larger than the intrinsic divergence of the beam $\sigma_{y'}$. The longitudinal resolution $\Delta\xi$ therefore is given by

$$S\Delta\xi \geq \sigma_{y'} \Leftrightarrow \Delta\xi \geq \frac{\epsilon_y}{\sigma_y S} = \frac{\epsilon_y c p_z}{\sigma_y ekV}, \tag{3.4}$$

with $\epsilon_y = \epsilon_{\mathrm{n},y}/(\beta\gamma)$ the geometric emittance. Using $p_z = \gamma\beta m_e c$ the longitudinal resolution can be rewritten as

$$\Delta\xi \geq \frac{\epsilon_{\mathrm{n},y} m_e c^2}{\sigma_y ekV}. \tag{3.5}$$

As can be seen from this equation, the longitudinal resolution depends only on the normalized transverse beam emittance, the beam size in the structure σ_y and the voltage, as well as the wave number of the RF- or plasma wave.

In this calculation it is assumed that the phase advance between the streaking position and the screen is 90°, so that the introduced angle is translated into a pure position change, which gives the best resolution. If this condition is not fulfilled the resolution is reduced to $\Delta\xi = \Delta\xi(\psi = \pi/2) \cdot |\sin\psi|^{-1}$, where ψ is the phase advance.

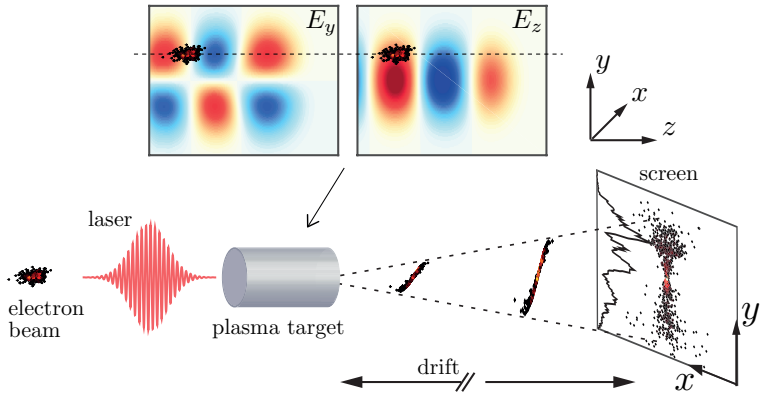

Figure 3.1 – Schematic setup of a current profile measurement with a transverse deflecting plasma. Top: Color coded transverse field $E_y(x = 0, y, \zeta)$ and longitudinal field $E_z(x = 0, y, \zeta)$ in arbitrary units. Transversely, the bunch is injected at the maximum of the transverse fields, at an offset of $y = w_0/2$, while longitudinally it is at the zero-crossing of the transverse fields. At this position, the longitudinal field is maximal longitudinally and exhibits a transverse slope. After the target in the drift, the momentum change is transferred to a change of transverse position carrying the time information.

3.2 Transverse Deflecting Plasma

An electron bunch, created by a conventional RF-based accelerator or in a previous LPA stage, is injected externally into a laser-driven wakefield.
It is possible to find a position in a linear plasma wave (compare eq. (2.12)) where the fields exhibit the same shape as those in a conventional transverse deflecting structure. Longitudinally, a zero-crossing of the transverse field is needed. This fixes the distance ζ between laser driver and witness bunch to multiples of $-\lambda_p/2$. On axis, the transverse fields $E_x(\zeta)$ and $E_y(\zeta)$ are zero. However, at an off-axis position of $w_0/2$, which is one rms of the laser spot size, the transverse fields are maximal. The optimum beam position for a streak in the y-direction therefore is at $x = 0$, $y = w_0/2$ and multiples of $\zeta = -\lambda_p/2$. An illustration of the bunch position within the linear wake can be found in figure 3.1. The longitudinal fields are at a maximum in ζ at this position, and exhibit a strong slope in y, just like in a TDS cavity [52].

The voltage of the transverse deflecting plasma stage (TDP) is calculated like in eq.

(3.2) and for a plasma target of uniform density and length l amounts to

$$V = \frac{a_0^2 k_p m_e c^2 \sigma_{z,l} l}{e w_0} \sqrt{\frac{\pi}{2}} \exp\left(-\frac{1}{2}\right) \exp\left(-\frac{k_p^2 \sigma_{z,l}^2}{2}\right). \tag{3.6}$$

3.2.1 Simulations on the Collinear TDP Setup

The discussed setup where laser and witness bunch propagate collinearly is directly applicable in external injection experiments. For illustration, in this section a Particle-In-Cell simulation is shown with an externally injected beam from the proposed SINBAD accelerator [23, 53].

The beam is accelerated and compressed in the conventional LINAC [54] and injected into a plasma target of 3.5 mm length and a constant density of $n = 1 \cdot 10^{18}\,\mathrm{cm}^{-3}$. The kinetic energy of the beam is 110 MeV with 0.17 % rms relative energy spread, the transverse emittance amounts to $\epsilon_{\mathrm{n},x} = \epsilon_{\mathrm{n},y} = 0.09\,\mathrm{mm\,mrad}$. In order to suppress space charge effects at the gun and to achieve a short bunch length, the bunch charge is low with 0.5 pC. Here, the phase of one accelerating cavity is deliberately detuned to create a spiky current profile of 7.5 fs rms length to demonstrate the resolution of the TDP. The electron beam size at the target position is $\sigma_x = \sigma_y = 17\,\mu\mathrm{m}$.

The laser spot size needs to be significantly larger than the electron beam size in order to reduce the resolution degradation from the curvature of the streaking field E_y depending on x and y. Furthermore, the laser intensity has to be in the strictly linear regime, $a_0^2 \ll 1$, to avoid nonlinear wave front curvature. A strong wave front curvature would introduce a correlation of the streaking signal also with the transverse position, where only a correlation with the longitudinal coordinate is desired. The parameters chosen here are $a_0 = 0.3$, $\lambda_l = 800\,\mathrm{nm}$ and $w_0 = 150\,\mu\mathrm{m}$. The laser pulse length of 41 fs FWHM is resonant with the density, i.e., $k_p \sigma_{z,l} = 1$ [32]. The delay between driver laser and beam is $\zeta/c = -\lambda_p/c$. The bunch propagates collinearly with the laser pulse, but is displaced by $w_0/2 = 75\,\mu\mathrm{m}$ in the y-direction. A summary of laser, beam, and plasma parameters can be found in table 3.1.

The bunch is propagated through the LINAC [54] with the space charge tracking code ASTRA [55]. It is then imported into the 3D PIC code WARP [39] where the interaction with the plasma is modeled in the Lorentz boosted frame [56] with $\gamma_{\mathrm{boost}} = 10$. The plasma is represented by one macroparticle per cell and the simulation box size is $84\,\mu\mathrm{m} \times 750\,\mu\mathrm{m} \times 750\,\mu\mathrm{m}$ with $3150 \times 375 \times 375$ cells.

The transverse fields in the plasma in the center of the target together with the bunch can be seen in fig. 3.2(a). The theoretical peak transverse field amplitude $E_{y0} =$

Driver Laser	
spot size w_0	$150\,\mu$m
pulse energy	3 J
pulse length (FWHM)	41 fs
normalized vector potential a_0	0.3
SINBAD Bunch	
kinetic energy E_{kin}	110 MeV
rms energy spread $\sigma_E/E_{\mathrm{kin}}$	0.17 %
beam size $\sigma_x = \sigma_y$	17 μm
transverse emittance $\epsilon_{n,x} = \epsilon_{\mathrm{n},y}$	0.09 mm mrad
bunch charge Q	0.5 pC
bunch length σ_z/c	7.5 fs
Plasma Parameters	
density n	$1 \cdot 10^{18}\,\mathrm{cm}^{-3}$
target length l	3.5 mm
Bunch Positioning	
distance behind laser ζ	$-34\,\mu\mathrm{m} \approx -\lambda_p$
offset in y-direction	$75\,\mu\mathrm{m} = w_0/2$
TDP Parameters	
voltage V	0.5 MV
wave number k_p	$1.9 \cdot 10^5\,\mathrm{m}^{-1}$
emittance limited resolution $\Delta\xi/c$	≥ 96 as

Table 3.1 – Laser, bunch and plasma parameters for the collinear plasma-based transverse deflection simulation.

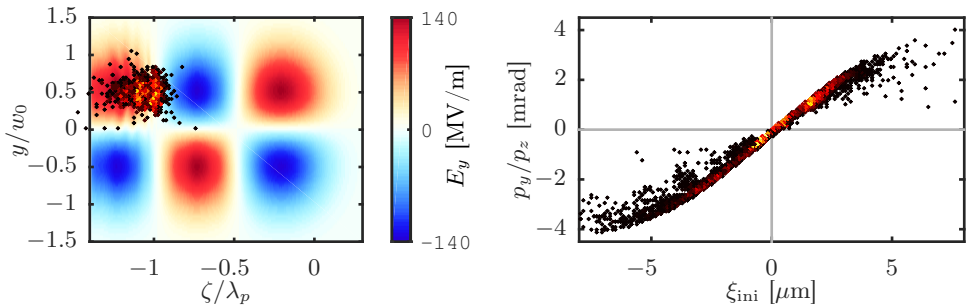

(a) Streaking fields in the plasma.

(b) Streaking trace after plasma.

Figure 3.2 – Snapshot from the PIC simulation near the center of the target ($z = 1.6\,\mathrm{mm}$, left) and streaking trace after the plasma (right). The slope of the phase space corresponds to the streaking signal, while the uncorrelated width in p_y/p_z is the background and is caused by the initial divergence of the beam and by deviations of the field from the ideal shape, such as curvature of the streaking field E_y in x and y or beam loading effects.

141 MV/m agrees well with the simulation result of 137 MV/m. The streaking trace is shown in fig. 3.2(b). The shear parameter determined from this phase space is $S = 762\,\mathrm{m}^{-1}$, which also agrees well with the theoretical value of $760\,\mathrm{m}^{-1}$. A very small displacement of the phase space from the origin at $\xi_{\mathrm{ini}} = 0$ and $p_y/p_z = 0$ is visible, which amounts to $0.15\,\mu$m in ξ_{ini} and stems from the bunch not being perfectly at the zero-crossing of the streaking field E_y in the PIC simulation.

After the plasma, the phase space is extracted from Warp, propagated along a 1 m drift, and imaged on a screen. The phase advance over this drift is 50°. This leads to a resolution degradation of 23 % compared to the ideal phase advance of 90°. For a longer drift, the phase advance would approach 90° asymptotically, or the ideal phase advance could be achieved by introducing more beam optical elements. For the sake of conceptual simplicity, this is not done here.
The particle distribution on the screen is shown in fig. 3.3. The y-coordinate of the particles on the screen carries the information on their initial position ξ_{ini} in the bunch. Consequently, the current profile is reconstructed by binning the particles to the y-axis and scaling with the shear parameter. A comparison of the reconstructed current profile (black) with the original one (dashed yellow) is given on the left axis of the figure.

Another feature is visible in fig. 3.3. The beam divergence in the x-direction, $\sigma_{x'}$, is

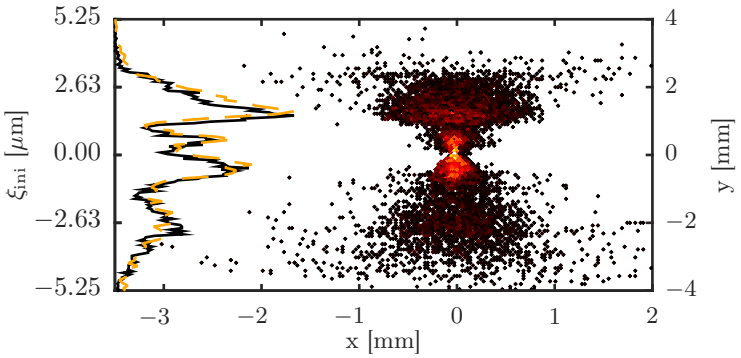

Figure 3.3 – Particle distribution on a screen 1 m downstream of the plasma target. The y-coordinate correlates to the initial position in the bunch. The current profile (black line) is reconstructed by binning the distribution to the y axis and scaling with the shear parameter. For comparison, the initial current profile is given in dashed yellow. The theoretical temporal resolution amounts to $\Delta\xi/c \geq 96\,\mathrm{as}$.

correlated with the y position on the screen, or rather with the initial longitudinal bunch coordinate, ξ_{ini}. The optimum ζ position in the wakefield is the zero-crossing of the streaking field E_y. However, this is also the zero-crossing of the electric field in the other transverse coordinate, E_x. In contrast to y, the beam is not displaced in the x-direction in the wakefield. E_x then acts as a focusing or defocusing field. In the case considered here, the bunch position is chosen as $\zeta = -\lambda_p$, and the head of the bunch is defocused while the tail is focused in x. After the plasma, the bunch tail quickly undergoes a focus and diverges significantly up to the screen which is the reason why the distribution seems to be axially symmetric around $y = 0$.

For this setup, the theoretical temporal resolution according to eq. (3.5) is

$$\Delta\xi/c \geq 96\,\mathrm{as}, \tag{3.7}$$

and $1\,\mathrm{as} = 1\cdot10^{-18}\,\mathrm{s}$. One should keep in mind that the resolution also profits from the low normalized transverse emittance of the simulated SINBAD beam of 0.09 mm mrad, and that this is a theoretical resolution that does not account for several detrimental effects discussed in the next section. Nevertheless, so far no other method achieving attosecond temporal resolution has been shown, especially no direct method featuring a short, mm-scale structure.

3.2.2 Detrimental Effects

Several effects could degrade the performance of the TDP. Just like in a conventional TDS cavity [52], the beam will accumulate an uncorrelated energy spread during the transition through the plasma which limits the resolvable slice energy spread. The temporal resolution can be limited by the curvature of the streaking field E_y depending on x and y. Furthermore, beam loading modifies the streaking field.

Accumulated Energy Spread

At $y = w_0/2$ where the bunch is positioned in the wakefield, the longitudinal electric field E_z exhibits a slope in y. This can be understood considering that the fields are derived from the electrostatic potential of the linear wake as $\vec{E} = -\nabla\Phi$. Since $E_y = -\partial_y\Phi$, the transverse maximum of the transverse field E_y, where the bunch is streaked, is found at the steepest slope of the potential Φ in y. This slope is transferred directly into the longitudinal field E_z, since for the longitudinal field only the longitudinal derivative of the potential is taken. For a Gaussian laser pulse, this position is the turning point of the potential Φ in y at one standard deviation of the laser intensity, i.e., at $y = w_0/2$. It is however a general effect that cannot be mitigated for example by transversely shaping the laser pulse.

The same effect occurs in TDS cavities and the derived expression [52] for the accumulated energy spread is valid for both the TDS and the TDP. The energy change of a particle crossing the plasma is given as

$$\Delta E_{\mathrm{kin}} = -e\int_0^l E_z(z)\mathrm{dz}, \tag{3.8}$$

which is approximated for simplicity as $\Delta E_{\mathrm{kin}} = -eE_z l$ assuming a constant longitudinal field over the length l.

A first order series expansion of the longitudinal field $E_z(x = 0, y, \zeta)$ from eq. (2.10) around $y = w_0/2$ gives the slope of this field in y as

$$\begin{aligned} E_z(x = 0, y, \zeta) &\approx -\frac{a_0^2 k_p^2 m_e c^2 \sigma_{z,l}}{e w_0}\sqrt{\frac{\pi}{2}}\exp\left(-\frac{1}{2}\right)\exp\left(-\frac{k_p^2\sigma_{z,l}^2}{2}\right) y\cos\left(k_p\zeta\right), \\ &= -\frac{V k_p y}{l}\cos\left(k_p\zeta\right), \end{aligned} \tag{3.9}$$

while in the following $\cos(k_p\zeta) = 1$ will be assumed. The average energy of the bunch in the TDP changes by

$$\Delta\bar{E}_{\mathrm{kin}} = -\frac{eVk_p w_0}{2}, \tag{3.10}$$

while the accumulated energy spread amounts to

$$\sigma_{E,\mathrm{acc}} = eVk_p\sigma_y. \tag{3.11}$$

In the simulation shown above, the central energy of the bunch is reduced from initially 110 MeV to 105 MeV, and the rms relative energy spread grows from $\sigma_E/\bar{E}_{\mathrm{kin}} = 0.17\,\%$ to $\sigma_E/\bar{E}_{\mathrm{kin}} = 1.4\,\%$. From eqs. (3.5) and (3.11) it follows that a transverse deflecting structure is limited in terms of the resolvable slice energy spread as

$$\sigma_{E,\mathrm{acc}}\Delta\xi = \epsilon_{\mathrm{n},y}/\gamma, \tag{3.12}$$

as an increase in temporal resolution $\Delta\xi$ also causes the bunch to accumulate a larger slice energy spread in the diagnostic device.

Higher Order Correlations of the Streaking Field

In the linear wakefield regime, the longitudinal field amplitude follows the transverse laser shape, $E_z \propto a^2(x,y,\zeta)$, while the transverse field amplitude is determined by the derivative of the transverse laser shape with respect to the transverse coordinate, $E_y \propto \partial_y a^2(x,y,\zeta)$.

For a Gaussian laser pulse, the maximum of the streaking field E_y is consequently found at the turning point of the Gaussian at $y = w_0/2$. However, this maximum is not flat but depends on x and y. The sides of the bunch will then experience a lower streaking signal than the bunch center.

In the next paragraph, the resolution degradation from these higher order correlations is calculated. The derivation up to eq. (3.18) follows [57].
For a bunch much smaller than the laser spot size ($\sigma_r \ll w_0/2$) the transverse field can be approximated by a series expansion in x and y to second order around $x = 0$ and $y = w_0/2$ as

$$E_y(x,y,\zeta) \approx -\frac{V}{l}\left[1 - \frac{1}{2}\left(\frac{2x}{w_0}\right)^2 - \left(\frac{2y-w_0}{w_0}\right)^2\right]\sin\left(k_p\zeta\right). \tag{3.13}$$

Neglecting slippage or laser evolution throughout the target, the transverse momentum change follows as

$$p_y = \frac{eV}{c}\left[1 - \frac{1}{2}\left(\frac{2x}{w_0}\right)^2 - \left(\frac{2y-w_0}{w_0}\right)^2\right]\sin\left(k_p\zeta\right). \tag{3.14}$$

In the following, a round Gaussian bunch with $\sigma_x = \sigma_y = \sigma_r$ is assumed. However, in principle it would be beneficial to choose an elliptical beam shape with $\sigma_x \ll \sigma_y$, as

the beam size in x can be reduced without causing a resolution degradation according to eq. (3.5). Yet, the effect of this will be limited, as the curvature of the streaking field is stronger in y than in x.

The average momentum change is reduced by the curvature, which is given by the average of the transverse momentum p_y over the bunch,

$$\overline{p_y} = \frac{eV}{c}\left[1 - \frac{3}{2}\left(\frac{2\sigma_r}{w_0}\right)^2\right]\sin\left(k_p\zeta\right), \tag{3.15}$$

while the bar is used according to the definition

$$\overline{p} = \frac{\int_{-\infty}^{\infty}\int_{-\infty}^{\infty} p n_b(x,y,\zeta)\,\mathrm{dxdy}}{\int_{-\infty}^{\infty}\int_{-\infty}^{\infty} n_b(x,y,\zeta)\,\mathrm{dxdy}} \tag{3.16}$$

here. The rms spread follows as

$$\begin{aligned}\sigma_{p_y,\mathrm{ho}} &= \sqrt{\overline{p_y^2} - \overline{p_y}^2} \\ &= \frac{\sqrt{10}\,eV}{2c}\left(\frac{2\sigma_r}{w_0}\right)^2 \left|\sin\left(k_p\zeta\right)\right|.\end{aligned} \tag{3.17}$$

$\sigma_{p_y,\mathrm{ho}}$ adds to the uncorrelated initial divergence, i.e., to the background of the streaking signal, and therefore reduces the resolution to

$$\Delta\xi \geq \sigma_{p_y,\mathrm{ho}}\frac{\partial\xi}{\partial p_y} = \frac{\sqrt{10}}{2}\left(\frac{2\sigma_r}{w_0}\right)^2 |\xi|, \tag{3.18}$$

where eq. (3.3) has been used, and the bunch is assumed to be positioned at the longitudinal zero-crossing of the deflecting field. For the parameter set discussed above, $\Delta\xi \geq 0.08 \cdot |\xi|$, and at one standard deviation of the beam the resolution is reduced by $\Delta\xi/c \geq 0.6\,\mathrm{fs}$. Note that this effect scales with the absolute value of the internal bunch coordinae, $|\xi|$, and reduces the resolution especially at the head and the tail of the bunch. This can also be seen in fig. 3.4, where the PIC simulation is compared to the analytical estimation. Near the bunch center, $\xi_{\mathrm{ini}} = 0$, the background to the streaking signal is given mainly by the beam emittance, while further away from the zero-crossing, where also a stronger curvature is visible, the phase space is smeared out towards smaller angles.

The contribution of $\sigma_{p_y,\mathrm{ho}}$ to the background increases with increasing electron beam size, while the initial divergence of the electron beam due to its emittance decreases for larger beam size. Consequently, an optimum beam size can be found. Since the divergence caused by the higher order correlations of the deflecting field, $\sigma_{p_y,\mathrm{ho}}$,

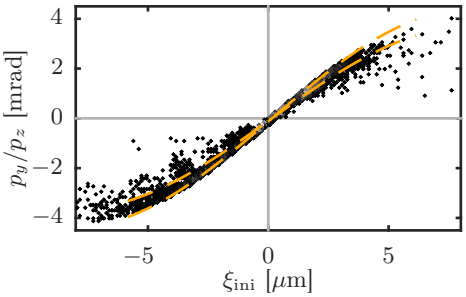

Figure 3.4 – Influence of higher order correlations of E_y with x and y. Comparison of the PIC simulation result (gray phase space) to the analytical estimation from eqs. (3.15) and (3.17), where the dashed yellow lines give $(\overline{p_y} \pm \sigma_{p_y,\mathrm{ho}})/p_z$. The analytical estimation is shifted by 0.15 μm to positive ξ_{ini} to coincide with the center of the phase space, which does not exactly cross the origin of $\xi_{\mathrm{ini}} = 0$ and $p_y/p_z = 0$.

depends on the longitudinal position within the bunch, this is only an average optimum beam size. The divergence averaged over a longitudinally Gaussian electron bunch of density $n_b \propto \exp\left(-\xi^2/(2\sigma_z^2)\right)$ is calculated as

$$\begin{aligned}
\overline{\sigma_{y',\mathrm{ho}}} &= \frac{\int_{-\infty}^{\infty} \sigma_{p_y,\mathrm{ho}} n_b(\xi)\mathrm{d}\xi}{p_z \int_{-\infty}^{\infty} n_b(\xi)\mathrm{d}\xi}, \\
&= \frac{1}{\sqrt{2\pi}\,\sigma_z} \frac{\sqrt{10}\, e k_p V}{2cp_z} \left(\frac{2\sigma_r}{w_0}\right)^2 \int_{-\infty}^{\infty} |\xi| \exp\left(-\frac{\xi^2}{2\sigma_z^2}\right)\mathrm{d}\xi, \\
&= \sqrt{\frac{80}{\pi}} \frac{eVk_p\sigma_z}{cp_z} \left(\frac{\sigma_r}{w_0}\right)^2 .
\end{aligned} \tag{3.19}$$

In the second line, the sine function was approximated as $|\sin(k_p\xi)| \approx k_p|\xi|$. The optimum electron beam size can then be calculated by minimizing the combined divergence depending on σ_r as

$$\begin{aligned}
\frac{\partial}{\partial\sigma_r}\sigma_{y'} &= \frac{\partial}{\partial\sigma_r}\sqrt{\left(\frac{\epsilon_{ny}}{\gamma\beta\sigma_r}\right)^2 + \overline{\sigma_{y',\mathrm{ho}}}^2} \stackrel{!}{=} 0, \\
\Rightarrow \sigma_{r,\mathrm{opt}} &= \left(\frac{\pi}{160}\right)^{\frac{1}{6}} \left(\frac{\epsilon_{ny} c p_z w_0^2}{\gamma\beta e V k_p \sigma_z}\right)^{\frac{1}{3}} .
\end{aligned} \tag{3.20}$$

With $\sigma_{r,\mathrm{opt}} = 9\,\mu$m, the optimum beam size for the SINBAD parameter set is smaller than the beam size $\sigma_r = 17\,\mu$m used in the simulations. This beam size, however, is

determined by the SINBAD LINAC simulations and is therefore not changed. The option remains to increase the laser spot size to achieve the optimum condition. Yet, $w_0 = 150\,\mu$m is already large, especially for the required high intensity, and therefore also the laser spot size is not increased any further for the treatment here.

Influence of Beam Loading

The streaking field is modified by the wakefield driven by the witness beam itself, a phenomenon known as beam loading. This leads to a resolution degradation especially in the tail of the beam.

The analytical estimation given here follows Ref. [57]. For a broad Gaussian beam ($k_p\sigma_r \gg 1$) the transverse wakefield can be written as

$$(E_y + cB_x)(x,y,\zeta) = y\frac{n_{b0}m_ec^2}{en_0\sigma_r^2}\exp\left(-\frac{r^2}{2\sigma_r^2}\right)\underbrace{\int_\infty^\zeta k_p\sin\left(k_p(\zeta-\zeta')\right)\mathrm{e}^{-\frac{\zeta'^2}{2\sigma_z^2}}\mathrm{d}\zeta'}_{:=Z(\zeta)}. \quad (3.21)$$

In contrast to eq. (2.15) this expression is also valid inside the drive beam. The transverse momentum change is given by

$$p_y = -\frac{e}{c}\int_0^l (E_y + cB_x)\mathrm{dz}, \quad (3.22)$$

which rewrites to

$$p_y = -\frac{n_{b0}lm_ec}{n_0\sigma_r^2}Z(\zeta)y\exp\left(-\frac{x^2+y^2}{2\sigma_r^2}\right) \quad (3.23)$$

for a constant density target and negligible beam evolution. The rms momentum change caused by the wake driven by the beam itself can be calculated with

$$\begin{aligned}\sigma_{p_y,\mathrm{bl}} &= \sqrt{\overline{p_y^2} - \overline{p_y}^2} \\ &= \frac{n_{b0}}{n_0}\frac{m_ec}{3\sigma_r}lZ(\zeta),\end{aligned} \quad (3.24)$$

where $\overline{p_y} = 0$ is evident since the focusing fields are symmetric. The reduction of the resolution is again given by $\Delta\xi \geq \sigma_{p_y,\mathrm{bl}}\partial\xi/\partial p_y$. For the parameters used here, beam loading plays only a minor role owing to the low charge of the considered beam. In order to reduce space charge effects in the gun of the linear accelerator, the bunch charge is only 0.5 pC. In the beam center, beam loading causes a reduction of the resolution by $\Delta\xi/c \geq 66$ as. The influence of beam loading scales directly proportional

to the bunch charge, and it can therefore limit the achievable time resolution in the bunch center to 0.66 fs for 5 pC or even to 1.3 fs for 10 pC bunch charge.

In analogy to the treatment of the divergence caused by higher order correlations of the deflecting field E_y, the longitudinally averaged divergence caused by beam loading can be calculated as

$$\begin{aligned}\overline{\sigma_{y',\mathrm{bl}}} &= \frac{\int_{-\infty}^{\infty} \sigma_{p_y,\mathrm{bl}} n_b(\xi)\mathrm{d}\xi}{p_z \int_{-\infty}^{\infty} n_b(\xi)\mathrm{d}\xi}, \\ &= \frac{1}{\sqrt{2\pi}\,\sigma_z}\frac{n_{b0}}{n_0}\frac{m_e c}{3\sigma_r} l \int_{-\infty}^{\infty} Z(\xi)\exp\left(-\frac{\xi^2}{2\sigma_z^2}\right)\mathrm{d}\xi,\end{aligned}$$

which can be solved numerically. The minimization of the combined divergence

$$\frac{\partial}{\partial\sigma_r}\sigma_{y'} = \frac{\partial}{\partial\sigma_r}\sqrt{\left(\frac{\epsilon_{ny}}{\gamma\beta\sigma_r}\right)^2 + \overline{\sigma_{y',\mathrm{ho}}}^2 + \overline{\sigma_{y',\mathrm{bl}}}^2} \stackrel{!}{=} 0 \tag{3.25}$$

then gives the optimum beam size accounting for both beam loading and higher order field correlations. Owing to the integral in the expression for $\overline{\sigma_{y',\mathrm{bl}}}$ the minimization is performed numerically. As beam loading effects call for larger beam sizes, the optimum beam size now amounts to 13 μm for the SINBAD parameters. Although this ideal beam size is smaller than the 17 μm used in the simulations shown above, the SINBAD example is not further optimized here. It should also be noted that this is an estimate, and that it is valid for a longitudinally Gaussian beam, which is not fulfilled in the SINBAD case. Equations (3.20) and (3.25) will be used later to find the optimum working point for a TDP demonstration experiment at the REGAE accelerator, see section 3.3.

3.2.3 Calibration of the TDP

In order to translate the y position on the screen into a time information the shear parameter $S = 1/p_z \cdot \partial p_y/\partial\xi = ek_pV/cp_z$ needs to be known. It is possible to estimate it analytically, however, an experimental determination of the shear parameter is highly desirable as the analytical estimation would need to make several assumptions on the plasma and laser properties.

The shear parameter can be determined from a scan of the delay between the driver laser and the witness bunch by correlating the time information from the delay with the bunch centroid position in y on the screen. Especially a large timing jitter can lead to errors in such a measurement. If the TDP is used to diagnose an RF accelerated beam, the arrival time jitter needs to be controlled by an external synchronization

system which can be very challenging. For the diagnostics of bunches from LPA it can be expected that the timing jitter is smaller since the TDP driver laser could be split off the LPA driver laser and therefore be intrinsically synchronized to the bunch.
Requiring an arrival time jitter around or below 10 % of the plasma period, for the parameters considered previously, i.e., a plasma period of 33 μm corresponding to 100 fs in time, this should be in the 10 fs range. Such a synchronization appears challenging though feasible for today's technology in the light of recent publications. At the SASE FEL FLASH in Hamburg, a synchronization of the X-ray FEL pulse and an infrared laser to 28 fs was demonstrated [58], still limited by the length of the FLASH bunches as the lasing region in the bunch fluctuates. At the seeded FERMI FEL in Trieste, a synchronization of the FEL pulse to an IR laser even down to 6 fs has been shown [59]. This number, however, profits from the seeding of the FEL that determines the lasing region in an otherwise long electron bunch, which is an advantage that cannot be exploited at external injection experiments like SINBAD or REGAE. The requirement on the synchronization can be relaxed by increasing the plasma period by decreasing the density. This, however, comes at the cost of reduced temporal resolution.

For the case considered above, the calibration in the presence of a timing jitter is simulated with ASTRA, which includes a plasma module where the linear wakefield model as given by eqs. (2.10)-(2.12) is used. Due to their computational cost, the thousands of runs needed to simulate jitters cannot be done with a full PIC code. In the case considered here, however, the condition for the linear regime, $a_0^2 \ll 1$, is well fulfilled and the model in ASTRA is a good approximation.

A delay scan is simulated over more than half a plasma period from $\zeta = -21\,\mu$m to $-45\,\mu$m in 0.5 μm intervals. At each delay 50 shots are taken simulating three scenarios for the arrival time jitter, 10 fs or 30 fs or 50 fs rms. The 10 and 30 fs cases can be found in figure 3.5. At the maximum positive or negative deflection the beam profiles on the screen are asymmetric as the bunch center is deflected most while both the bunch head and tail are deflected less. Therefore the median is used for the calculation of the bunch centroid on the screen instead of the mean, as the median weighs outliers less than the mean. Each gray dot in figures 3.5(a) and 3.5(b) represents one bunch centroid on the screen at a given average delay. The blue line is calculated by taking again the median of all shots for each delay. The shear factor, or the slope of the deflection near the zero-crossing at $\zeta = -\lambda_p$, is defined by the plasma wave number k_p and by the voltage V or maximum deflection. The plasma period can be extracted from the jitter simulation by fitting a sine function (yellow) to the median of shots (blue). For the voltage the shot with the minimum and maximum deflection is used, as this corresponds to the bunch being at the peak of the delecting field. Since the timing jitter leads to a decrease of the amplitude of the fitted sine this

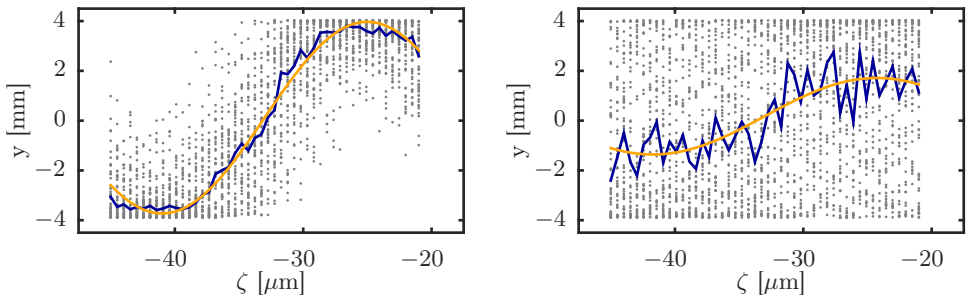

(a) 10 fs rms arrival time jitter.

(b) 30 fs rms arrival time jitter.

Figure 3.5 – Calibration of the TDP under the influence of an arrival time jitter between driver laser and witness bunch. Each gray dot is the bunch centroid on the screen for one shot simulated with ASTRA. The blue line indicates the median over all 50 shots at each distance ζ behind the driver. The wavelength λ_p is reconstructed from a sine fit (yellow) and the voltage V is gained from the minimum and maximum deflection.

amplitude does not present a good measure for the voltage.

The shear factor obtained from this method is compared to the one calculated from a linear fit to the streaking trace, p_y/p_z depending on ξ_{ini}, extracted also from an ASTRA simulation. For the arrival time jitter of 10 fs rms, S is reconstructed with a relative error of 6 % (reconstructed plasma period: 32 μm, deflection amplitude: 4.0 mm), and for the jitter of 30 fs rms S is determined with a relative error of 14 % (reconstructed plasma period: 35 μm, deflection amplitude: 4.0 mm). In the case of 50 fs jitter the sine fit fails and no calibration can be achieved with this method.

The calibration is a multi-shot measurement. In contrast, the streaking itself is a single-shot measurement that is possible to perform even with a large timing jitter. The time information is encoded in the average deflection in y. Those shots where the bunch hits the screen at $y = 0$ can then be identified as having the correct delay.

This timing jitter study does not include any other error sources. Positioning jitters as well as angle jitters can also lead to a fluctuation of the deflection. The tolerance to the bunch positioning scales with the laser spot size, as the spot size determines the width of the wakefield. The tolerance to the angle of the incoming bunch with respect to the laser axis scales with the deflecting voltage. In general, a higher laser energy allowing for a larger spot size at the same or higher voltage can make the TDP more

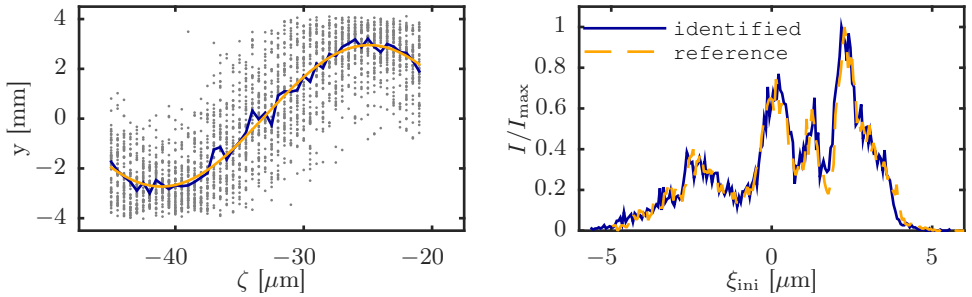

(a) Arrival time, positioning and angle jitter.

(b) Optimum shot extraction.

Figure 3.6 – Calibration of the TDP under the influence of an arrival time jitter between driver laser and witness bunch (a). Best shot identified from the jitter-afflicted data (b). The reference case, shifted by 0.5 μm to positive ξ_{ini}, agrees well with the identified shot. Colors in (a) like in fig. 3.5.

tolerant to positioning and angle jitters.
A similar simulation as shown in fig. 3.5 is shown in fig. 3.6 for an arrival time jitter of 10 fs rms, and an additional positioning jitter of 30 μm rms, i.e., 20 % of w_0, and an angle jitter of 100 μrad rms. Both the positioning and the angle jitter are imprinted on the electron bunch, while the laser does not jitter in the simulation. For the positioning jitter the relative displacement between laser and electron beam is the important quantity and it is therefore irrelevant which beam is displaced. For the angle jitter this presents an upper estimate as an initial angle on the electron beam will cause an additional displacement on the screen which would not be the case for a pointing jitter of solely the laser. From this simulation the calibration is extracted with a relative error of 5 % (reconstructed plasma period: 32 μm, deflection amplitude: 4.1 mm).

In the case of a pure arrival time jitter it is straightforward to identify those shots that hit the center of the screen as the ones situated at the correct streaking position in the plasma wake. If additional positioning and pointing jitters are present also an initial beam pointing could be compensated by an opposite deflection in the plasma, or a beam could have a large offset and still end up in the center of the screen. To still identify a good shot the jitter-afflicted data can be filtered. One method is to filter first for the shots hitting near the screen center (here, ± 1 mm in y) and from those to use the phase space that is largest in y, as this bunch has experienced the largest streaking voltage, and an initial offset or angle will always reduce the streaking voltage. If the

bunch length is not constant for all bunches, this method will also identify the longest bunch, which will give a conservative estimation of the bunch length.
The shot identified by this method as well as the ideal bunch situated at the correct delay can be seen in fig. 3.6(b). The identified shot had an initial offset of $-1.9\,\mu$m and $0.3\,\mu$m and an initial angle of $1.0\,\mu$rad and $132\,\mu$rad in x and y, and an arrival time error of 1.0 fs compared to the ideal value. The good agreement between the reference case and the identified phase space allows to conclude that such a filter is a powerful method to extract data even with large jitters present.

3.2.4 Non-collinear Experimental Geometry

In the experimental geometry discussed so far, the laser and the electron bunch propagate collinearly. In external injection experiments such a geometry appears naturally. There, the TDP could be installed exchangeably with the acceleration target to diagnose the pre-accelerated electron bunch exactly at the injection position.

In this collinear geometry, the laser needs to be coupled into the electron beam path, for example using a magnetic chicane, a dogleg, or a mirror with a hole. However, it is also possible to create a streaking in the plasma with an angle between the laser and the electron beam path. This provides additional freedom in the experimental design, as no mirrors need to be placed in the electron beam path. To realize the geometry with an angle, the plasma profile needs to fulfill certain requirements which will be discussed in this section.

A schematic of the setup can be found in figure 3.7. The angle α between the laser and the beam propagation axis is in the x-z-plane. The laser propagates in the z-direction, and the bunch travels in the z^*-direction. The streaking is imprinted in the y-direction, so that the beam enters the wake again at an offset of one rms of the laser intensity, $w_0/2$, in y. The imprinted transverse momentum change p_y is proportional to the integral of $E_y + cB_x$ along the beam trajectory through the wake. Assuming a stiff beam, this is a straight line. The trajectory can best be pictured in the co-moving frame of the laser which moves at the group velocity v_{gr}. For a constant plasma density and non-evolving laser pulse the phase velocity of the wake, v_{ph}, is given by the group velocity of the laser, v_{gr}.

In the laboratory frame, the bunch travels at the velocity $\vec{v}_{z^*}$. In the co-moving frame of the wake with $\zeta = z - v_{\mathrm{gr}}t$, which is not a Lorentz transformation, the laser position is fixed and the bunch seems to travel sideways through the wake. In order to get a clean streaking signal, the imprinted momentum change should correlate only with the longitudinal coordinate of the bunch ξ, but not with its transverse coordinates x^*

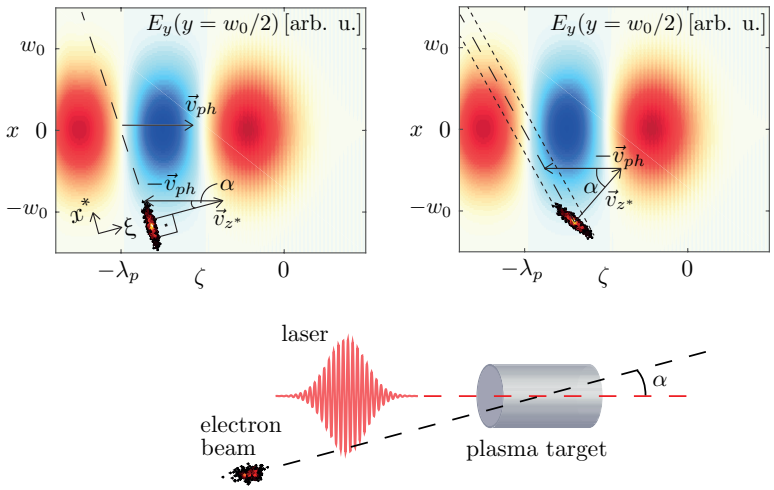

Figure 3.7 – Schematic setup of a transverse deflecting plasma measurement including an angle α between laser and bunch propagation axis in the x-z-plane. Top: Color coded deflecting field $E_y(x, y = w_0/2, \zeta)$ and the seeming direction of movement of the bunch in the co-moving frame of the wake. If the phase velocity fulfills eq. (3.26) the bunch seems to move sideways through the wake (left). If the condition is not fulfilled, a correlation of the imprinted momentum change p_y with the x-coordinate in the bunch exists (right).

or $y = y^*$. The seeming direction of movement of the bunch in the co-moving frame of the wake therefore needs to be perpendicular to $\vec{v}_{z^*}$. The condition can be written as

$$v_{\mathrm{ph}} = \frac{v_{z^*}}{\cos\alpha}. \tag{3.26}$$

In the left image in fig. 3.7 the angle, the bunch velocity, and the phase velocity are well chosen, and the bunch seems to move sideways through the wake as indicated by the dashed line. In the right image, however, this condition is not fulfilled. The imprinted momentum change then correlates with the transverse coordinate inside the bunch, x^*, as indicated by the small dashed lines.

Since typically the beam velocity is almost the speed of light, $v_{z^*} \approx c$, equation (3.26) requires a phase velocity larger than the speed of light for highly relativistic beams. This can be achieved by tailoring the plasma density. Under the assumption that $v_{\mathrm{gr}} \approx c$ the plasma up ramp needed to fulfill this condition can be calculated with [60]

$$\frac{\mathrm{d}n}{\mathrm{d}z} = \left(\frac{c}{v_{\mathrm{ph}}} - 1\right)\frac{2n}{\zeta_b}. \tag{3.27}$$

Here, ζ_b is the time-dependent distance of the beam to the driver laser given by

$$\zeta_b = \zeta_{b,\mathrm{ini}} + \left(\frac{v_{z^*}}{v_{\mathrm{gr}}}\cos\alpha - 1\right) z. \tag{3.28}$$

Angles of several degrees are possible with this method, as will be shown with simulations in the next paragraphs. However, very large angles will reduce the interaction time and require a steep density gradient, which eventually limits both the achievable voltage and the practicability. Furthermore, due to the density gradient, a correlation of the streaking voltage with the x-coordinate of the beam can be expected, as one side of the beam experiences a net lower density as the other side of the beam. Therefore, few-degree angles in general are favorable as they increase the possible interaction time and reduce the requirements on the target design.

PIC Simulation of Non-collinear Setup

An exemplary PIC simulation of a setup featuring an angle of $\alpha = 5°$ between laser and bunch propagation axis is shown in the following. The same laser and bunch parameters as in the collinear case are used, see table 3.1. The plasma length, however, is increased to 6.5 mm to accommodate for the complete crossing time, which is still short compared to the Rayleigh length of the laser of 8.8 cm. Please note that even though the target is longer than for the collinear case, the effective streaking voltage will be reduced as the bunch passes from one side of the wake to the other. The target

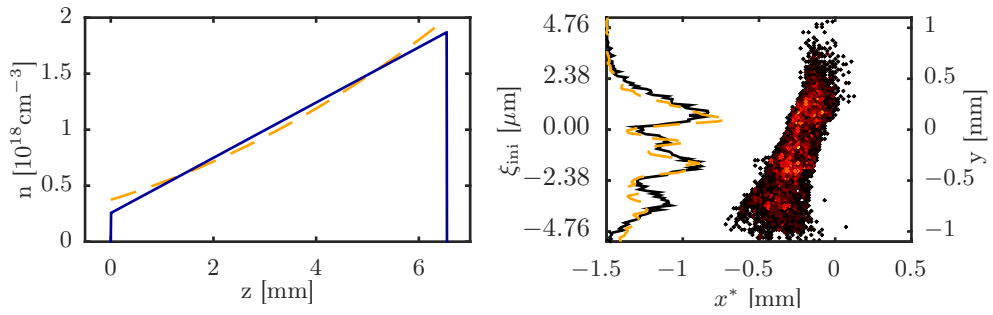

(a) Tapered plasma profile.

(b) Beam profile on screen.

Figure 3.8 – (a) Tapered plasma profile to fulfill the phase velocity according to eq. (3.26). The numerical solution of eq. (3.27) is given in dashed yellow, and the plasma profile used in the PIC simulation is a linear fit to this solution (solid blue). Right: Beam profile on a screen 1 m downstream of the plasma target. The current profile obtained by binning to the y-axis is given in black. Dashed yellow is the original current profile, and ξ_{ini} gives the internal bunch coordinate, for reference.

features a linear density up ramp from $n = 0.26 \cdot 10^{18}\,\mathrm{cm}^{-3}$ to $1.9 \cdot 10^{18}\,\mathrm{cm}^{-3}$ to ensure the phase velocity required by eq. (3.26). This is a linear fit to the density profile calculated from eq. (3.27), as shown in fig. 3.8(a). The distance of the beam behind the laser is chosen to be $\zeta_0 = -\lambda_p$ at the center of the target. For this simulation WARP is used in 3D in the boosted frame with $\gamma_{\mathrm{boost}} = 10$. The plasma is represented by one macroparticle per cell, the simulation box size is $92\,\mu\mathrm{m} \times 825\,\mu\mathrm{m} \times 825\,\mu\mathrm{m}$ with $3448 \times 412 \times 412$ cells.

Figure 3.8(b) shows the simulated beam profile on a screen positioned 1 m behind the target. The current profile is reconstructed by binning to the y-axis (black line). For comparison, also the original current profile is given (dashed yellow). The current profile is reproduced well. Compared to the screen image in the collinear case (figure 3.3) two major differences are visible. The bunch is smaller in x^* and y, and it steers towards the negative x^*-direction.

The steering in x^* is caused by the electric field in x. At the start of the plasma, the bunch is situated at a negative x coordinate in the defocusing region at $\zeta > -\lambda_p$, i.e., it experiences a positive field in x and consequently a negative change of momentum, Δp_x. As soon as the bunch crosses $x = 0$ it also enters the focusing region at $\zeta < -\lambda_p$. The field is still positive, and the steering towards negative x is further increased.

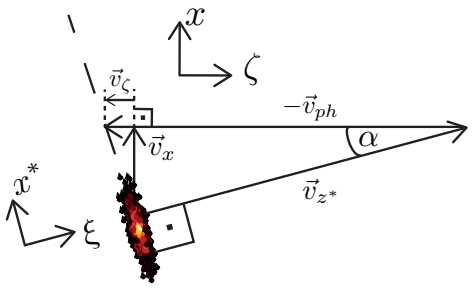

Figure 3.9 – Definitions of velocities in the co-moving frame of the wake (compare fig. 3.7), used in the derivation of the estimated resolution.

The limited interaction time between bunch and wake owed to the crossing angle effectively limits the imprinted streak signal and also causes the bunch to be smaller on the screen. The resolution calculated from the fitted slope of the simulated phase space after the interaction amounts to $\Delta\xi/c \geq \epsilon_{\mathrm{n},y} m_e/\sigma_y \cdot \partial\xi/\partial p_y = 0.39\,\mathrm{fs}$.

Estimate of the Resolution for the Non-collinear Setup

The momentum change p_y is given by the transverse fields E_y experienced by the bunch during its transition through the wakefield as

$$\begin{aligned} p_y &= -e \int_{-\infty}^{\infty} E_y(x(t), y = w_0/2, \zeta(t))\,\mathrm{dt} \\ &= -\frac{e}{v_x} \int_{-\infty}^{\infty} E_y(x, y = w_0/2, \zeta(x))\,\mathrm{dx}. \end{aligned} \tag{3.29}$$

Here, $v_x = \beta c \sin\alpha$ is the velocity component of the bunch in the x-direction. The transverse field at $y = w_0/2$ is given as (compare eq. (2.12))

$$\begin{aligned} E_y(x, y = w_0/2, \zeta) = -\frac{a_0^2 m_e c^2 \sigma_{z,l}}{e w_0} \sqrt{\frac{\pi}{2}} \exp\left(-\frac{1}{2}\right) \times \\ k_p \exp\left(-\frac{k_p^2 \sigma_{z,l}^2}{2}\right) \exp\left(-\frac{2x^2}{w_0^2}\right) \sin\left(k_p \zeta\right), \end{aligned} \tag{3.30}$$

while both ζ and k_p, or n, now depend on x, the transverse bunch position in the wake. With the velocities v_x and v_ζ as in figure 3.9, $\zeta(x)$ follows as $\zeta(x) = \zeta_0 - v_\zeta/v_x \cdot x$. The distance in laser propagation direction z between the laser and the bunch is denoted

by ζ_0 at the center of the target or, what shall be equivalent, when the bunch is at $x = 0$. The plasma density is given by $n(z) = n_{\mathrm{mid}} + n'(z - z_{\mathrm{mid}})$, with n_{mid} the plasma density at the center at $z = z_{\mathrm{mid}}$, and n' the slope of the linear ramp. With $x = z \tan\alpha$, $n(x)$ follows directly as

$$n(x) = n_{\mathrm{mid}} + n' x / \tan\alpha. \tag{3.31}$$

The theoretical resolution can then be gained from the numerical integration of eq. (3.29), using eqs. (3.30) and (3.31), for different delays corresponding to longitudinal positions in the bunch $\zeta_{\mathrm{ini}} = \zeta_0 + \xi \cos\alpha$. For the parameters used in the PIC simulation, the theoretical resolution amounts to $\Delta\xi/c \geq 0.32\,\mathrm{fs}$. For several reasons, this is slightly smaller than the resolution of 0.39 fs obtained from the phase space. For one thing, the delay of the bunch was not chosen optimally in the simulation, so that the bunch did not pass the wake exactly through the zero-crossing. This might also be caused by an unphysical reduction of the laser group velocity from numerical dispersion in the PIC code. Furthermore, the analytical estimation does not account for the following effects connected to the transverse beam size: The linear approximation of the ideal plasma profile will introduce a small correlation of the transverse momentum p_y with the transverse coordinate inside the bunch, x^*, and additionally, as the density increases while the bunch crosses the wake, particles at the side of the bunch crossing later will experience a larger deflection. Also, as discussed for the collinear case, beam loading will hamper the resolution, as well as the curvature of the streaking field E_y in y. The influence of the curvature is very similar to the collinear case, except that the contribution in x^* is different, which is mainly caused by the above mentioned different densities experienced depending on the x^* coordinate of the particles. However, this contribution to the resolution reduction is of similar or smaller magnitude than the influence of the curvature of the deflecting field E_y in y, as can be seen from the phase space after the plasma interaction (not shown). All of these effects are not part of this analytical estimation, but are intrinsically included in the simulation, which explains the reduced resolution in the simulation.

3.3 TDP at the REGAE External Injection Experiment

At DESY in Hamburg it is planned to use the conventional accelerator REGAE (**R**elativistic **E**lectron **G**un for **A**tomic **E**xploration) [61, 62] to externally inject electron beams into a laser-driven plasma wakefield [21]. This experiment could also serve as a testbed for the TDP, as REGAE is designed to deliver electron beams of few

REGAE Bunch	
kinetic energy E_{kin}	$\leq$ 5.6 MeV
rms energy spread σ_E/E	0.2 %
transverse emittance $\epsilon_{\mathrm{n},x} = \epsilon_{\mathrm{n},y}$	$<$ 0.1 mm mrad
bunch charge Q	$\approx$ 100 fC
bunch length σ_z/c	$\lesssim$ 5 - 10 fs
ANGUS Driver Laser	
spot size w_0	42 μm
pulse energy	5 J
pulse length (FWHM)	100 fs
normalized vector potential a_0	0.9

Table 3.2 – Laser and bunch parameters at the REGAE external injection experiment.

fs length. Originally, REGAE was designed for time-resolved electron diffraction experiments, performed by the group around R.J.D. Miller [63]. The electron bunch is created at a photocathode in the gun cavity and is accelerated to a few MeV in this cavity. After a short drift an energy chirp is imprinted onto the bunch in the so-called buncher cavity. Electrons in the head of the bunch are decelerated, while electrons in the tail of the bunch are accelerated. In a drift after the buncher cavity this velocity difference leads to a temporal compression of the bunch, down to a few fs at the target.

3.3.1 Experimental Parameters

The electron beam and laser parameters are summarized in table 3.2. Most of these parameters have already been measured at the machine. For example, the transverse emittance has been determined to be as low as $\epsilon_{\mathrm{n},y} = 0.02\,\mathrm{mm\,mrad}$ [64], however at a low charge (37 fC) and low kinetic energy (2.45 MeV). For the external injection experiment, as well as for a potential TDP measurement, a larger kinetic energy is favorable. The reason is that at the laser focus, i.e., where the external injection into the wakefield takes place, the laser is situated in front of the bunch. Due to their velocity difference, however, the laser overtakes the bunch shortly in front of its focus. A larger bunch energy shifts this overtaking position away from the laser focus and relaxes possible beam quality degradation due to the interaction with the laser [21, 24]. For this reason the kinetic energy $E_{\mathrm{kin}} = 5.6\,\mathrm{MeV}$ is chosen, which is near the maximum achievable energy at this machine. Furthermore, a more conservative normalized emittance of 0.1 mm mrad is assumed to allow for more charge or stronger transverse focusing than in [64].

The laser parameters are determined by the design of the external injection experiment [21, 24]. The electron beam size will be fraction of the laser spot size to keep the influence of the curvature of the streaking field low. At the same time, a large beam size allows for good temporal resolution by reducing the intrinsic divergence of the beam. The resolution degradation from the higher order correlations depends on the z position in the bunch and consequently on the bunch length. An optimum beam size therefore cannot be determined without a priori knowledge of the bunch length.

Note that this discussion, as well as the previous section, assumes a Gaussian laser pulse. In general, such an assumption is not fulfilled for the experimentally available high power laser systems. The temporal laser shape is not critical for the TDP, as it only changes the wakefield amplitude, which will be included in the calibration. The transverse laser shape, however, is crucial, since the transverse fields in the linear wakefield regime follow the derivative of the laser intensity with respect to the transverse coordinate. As a consequence, a smooth transverse laser profile is required to minimize resolution degradation from transverse changes of the streaking field. The laser profile does not need to be Gaussian, though, and within the linear regime the treatment can also be adapted to a different, known, shape. Ideally, to even completely avoid resolution degradation from higher order correlations of the deflecting field, the laser intensity should be constant in x and rise linearly in y. Since this is not very realistic especially for first proof of principle experiments, the assumption of a Gaussian profile will be kept here.

The electron bunch length of 10 fs at REGAE is gained from ASTRA simulations [21]. Recently, a new operation mode has been proposed [65, 24] that could reduce the bunch length even below one femtosecond, making use of the drift between gun and buncher to achieve a curvature correction of the phase space. At REGAE, the bunch length has not been measured so far as the low signal expected from the small bunch charge makes optical methods such as coherent transition radiation very challenging. For the future, the installation of a conventional TDS cavity is planned [50]. For a normalized emittance of $\epsilon_{\mathrm{n},x} = 0.01\,\mathrm{mm\,mrad}$ the streaking cavity is expected to provide a temporal resolution down to 10 fs, including errors and imperfections [50]. The few-fs bunch length assumed here is realistic, especially in the light of recent results from the UCLA Pegasus laboratory, which features a similar experimental setup as REGAE and where a bunch length of 7 fs rms has been measured with an X-band TDS cavity [66].

The aim of this section is to show the feasibility of a TDP proof-of-principle experiment at REGAE. Also, its limitations in terms of time resolution are explored to see if it could be used to demonstrate the phase space linearization proposed in [65].

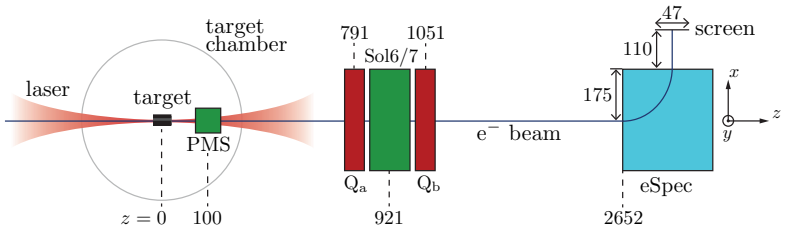

Figure 3.10 – Sketch (not to scale) of the REGAE beamline layout downstream of the target chamber. All dimensions in mm.

3.3.2 Design Considerations

Owing to the low kinetic energy of the REGAE beam, the design of the TDP needs to account for some effects that were negligible in the previously shown example case with SINBAD parameters. First, the streaking leads to a very large beam divergence after the plasma. This sets a limit on the possible streaking voltage that allows beam transport to the detector without hitting the physical walls of the beam pipe. Second, during the transition through the TDP, the bunch acquires a transverse offset caused by slippage effects, and also the bunch is elongated from the imprinted energy spread. Both effects are more severe for low initial beam energy. They scale with the voltage, but also explicitly with the structure length l and favor therefore a short plasma length [50]. In the following, the maximum allowable divergence is estimated, and a plasma target design is derived fitting the demands of the low energy REGAE bunch.

Downstream Beamline Layout

This section briefly names and describes the beam optical elements of the REGAE beamline designed for the external injection experiment [24] that are downstream of the plasma target and relevant for the discussion here. A sketch of the element positions can be found in figure 3.10.

The plasma target is in the center of the target chamber. Shortly behind it, still inside the chamber, a permanent magnetic solenoid (PMS) [67] is placed on a linear stage allowing for some flexibility of position. Here, the PMS is near to the target with a distance of 10 cm between the target center and the PMS center. This minimizes the electron beam size in it and consequently minimizes the errors from field nonlinearities away from the axis.

After the target chamber, a beam pipe leads to the electron spectrometer (eSpec) positioned at 2.65 m behind the target. It disperses the beam in the x-plane and features a beam pipe diameter in the y-plane of 38 mm. This fixes the streaking plane to y, carrying the time information, while the energy information is transferred to the x plane in the spectrometer. The measurement of the streaked bunch in the spectrometer gives direct access to the longitudinal phase space. However, it should be kept in mind that the energy resolution is inversely proportional to the temporal resolution according to eq. (3.12), just like for a conventional TDS cavity.

In between the target chamber and the spectrometer, around 1 m behind the target, two electrical quadrupoles, $\mathrm{Q_a}$ and $\mathrm{Q_b}$, and one electrical solenoid, Sol6/7, are placed. The beam pipe diameter in these focusing elements is 38 mm.

Maximum Tolerable Divergence

To ensure maximum resolution, the phase advance between the TDP position and the detector needs to be $90° + k \cdot 180°$, $k \in \mathbb{N}_0$. In the most simple case this is realized by a long enough drift, where the phase advance converges to 90°. For REGAE, such a procedure would mean not to focus the beam at all after the plasma. Consequently, to prevent clipping at the beam pipe, the divergence would need to be small, limiting the temporal resolution. To allow for larger divergence and better resolution, the PMS directly after the target is used in addition to the quadrupole doublet $\mathrm{Q_a}$ and $\mathrm{Q_b}$. The PMS provides some initial divergence reduction but it is not strong enough to achieve a focus. The first quadrupole then defocuses in x and focuses in y to capture the strongly divergent beam. The doublet is tuned to focus the beam in y to a position halfway between the beam optics and the spectrometer, leading to a phase advance of around 270° between the TDP and the detector position, i.e., the spectrometer screen. Consequently, the transverse beam size in the first quadrupole is similar to the one in the spectrometer. In other words, if no clipping occurs in this quadrupole, also the aperture of the spectrometer does not pose a problem. Since the TDP does not significantly increase the bunch energy, the solenoid Sol6/7 would also be strong enough to focus the beam. Here, however, only the quadrupoles are used, first to gain additional freedom how to focus both planes, and second to avoid abberations from the field nonlinearities of the solenoid in combination with the large beam.

The maximum acceptable divergence after the target can be estimated with the help of beam transport matrices (see e.g. [41]). The transport matrices for a drift and for a thin focusing lens read

$$M_d = \begin{pmatrix} 1 & s \\ 0 & 1 \end{pmatrix} \text{ and } M_f = \begin{pmatrix} 1 & 0 \\ -1/f & 1 \end{pmatrix}, \tag{3.32}$$

respectively. Here, s is the drift length and f the focal length of the lens. The transport of the Courant-Snyder parameters from the target to the first quadrupole, Q_a, is then given by

$$\begin{pmatrix} \beta_S & -\alpha_S \\ -\alpha_S & \gamma_S \end{pmatrix} = \begin{pmatrix} C & S \\ C' & S' \end{pmatrix} \begin{pmatrix} \beta_T & -\alpha_T \\ -\alpha_T & \gamma_T \end{pmatrix} \begin{pmatrix} C & S \\ C' & S' \end{pmatrix}^T, \tag{3.33}$$

with

$$\begin{pmatrix} C & S \\ C' & S' \end{pmatrix} = \begin{pmatrix} 1 & s_{\mathrm{PQ}} \\ 0 & 1 \end{pmatrix} \begin{pmatrix} 1 & 0 \\ -1/f_{\mathrm{PMS}} & 1 \end{pmatrix} \begin{pmatrix} 1 & s_{\mathrm{TP}} \\ 0 & 1 \end{pmatrix}. \tag{3.34}$$

Here, the distance between the PMS and the first quadrupole is $s_{\mathrm{PQ}} \approx 0.69\,\mathrm{m}$, the distance between the target and the PMS is $s_{\mathrm{TP}} = 0.1\,\mathrm{m}$ and the focal length of the PMS is $f_{\mathrm{PMS}} \approx 0.2\,\mathrm{m}$ [67] for a kinetic energy of 5.6 MeV. At the target the bunch is in focus, and consequently $\alpha_T = 0$. For the beta function at the first quadrupole then follows

$$\beta_{\mathrm{S}} = C^2 \beta_{\mathrm{T}} + S^2 \frac{1}{\beta_{\mathrm{T}}}, \tag{3.35}$$

which, using $\beta_{\mathrm{CS}} = \sigma_y^2/\epsilon_y$ and $\sigma_{y,\mathrm{T}}\sigma_{y',\mathrm{T}} = \epsilon_y$, can be rewritten to obtain the electron beam size as

$$\begin{aligned} \sigma_{y,\mathrm{S}}^2 &= C^2 \sigma_{y,\mathrm{T}}^2 + S^2 \sigma_{y',\mathrm{T}}^2, \\ &= \left(1 - \frac{s_{\mathrm{PQ}}}{f_{\mathrm{PMS}}}\right)^2 \sigma_{y,\mathrm{T}}^2 + \left(s_{\mathrm{TP}} + s_{\mathrm{PQ}} - \frac{s_{\mathrm{TP}} s_{\mathrm{PQ}}}{f_{\mathrm{PMS}}}\right)^2 \sigma_{y',\mathrm{T}}^2, \\ &= (-2.45)^2 \sigma_{y,\mathrm{T}}^2 + (0.45\,\mathrm{m})^2 \sigma_{y',\mathrm{T}}^2. \end{aligned} \tag{3.36}$$

Typically, the beam size at the target $\sigma_{y,\mathrm{T}}$ is in the range of 1 to 10 μm, and the beam divergence $\sigma_{y',\mathrm{T}}$ can be expected to be between 1 and 10 mrad. The contribution of the initial divergence to the beam size in the quadrupole, $\sigma_{y,\mathrm{S}}$, is therefore around two orders of magnitude larger than the contribution of the initial beam size, and the first term of eq. (3.36) can be neglected. As an upper limit to the tolerable beam size at the quadrupole position $6 \cdot \sigma_{y,\mathrm{S}} \leq 35\,\mathrm{mm}$ is required, which is only marginally smaller than the beam pipe diameter of 38 mm, and the maximum tolerable divergence at the target follows as $\sigma_{y',\mathrm{T,max}} = 13\,\mathrm{mrad}$.

Note that this is an estimate that does not account for possible misalignments, field nonlinearities, which such a large beam experiences in the solenoid, or energy changes in the TDP. Apart from this, if the ideal beam just barely fits through the beam pipe, there will be no room for scanning the bunch phase in the wake and calibrating the deflection. Therefore, the divergence should at least be a factor of two smaller than this upper limit, i.e., $\sigma_{y',\mathrm{T,max}} = 6.5\,\mathrm{mrad}$.

Imprinted Divergence

The TDP, as well as any conventional TDS cavity, imprints a divergence on the electron bunch that depends on the streaking voltage and on the bunch length. From eq. (3.3) the imprinted divergence follows as

$$\sigma_{y',\mathrm{TDP}} = S \cdot \sigma_z = \frac{ek_pV}{cp_z}\sigma_z. \tag{3.37}$$

The temporal resolution $\Delta\xi/c$ can be expressed depending on the imprinted divergence as

$$\frac{\Delta\xi}{\sigma_z} \geq \frac{\epsilon_y cp_z}{\sigma_y\sigma_z ek_pV} = \frac{\epsilon_{\mathrm{n},y}}{\gamma\beta\sigma_y\sigma_{y',\mathrm{TDP}}}. \tag{3.38}$$

This expression shows the dynamic range of the current profile diagnostic. It is determined by the maximum divergence that can be captured after the streaking. In other words, it is difficult to diagnose a long bunch with a good temporal resolution, as its divergence would become very large. A larger kinetic energy can increase the dynamic range.

For a given divergence, energy, beam emittance and bunch length, the only remaining free parameter to optimize the temporal resolution is the electron beam size σ_y. It is therefore favorable to increase the beam size while keeping the voltage fixed. However, for a given laser spot size w_0, the electron beam size cannot be increased without loss of resolution due to higher order correlations of the streaking field. This leaves the option to increase both the laser spot size and the electron beam size, and to compensate the decrease of laser intensity by increasing the plasma length.

Experimentally, the laser focal spot size w_0 is directly proportional to the focal length of the parabolic mirror used as the final focusing optics, and inversely proportional to the beam size of the collimated laser on this optical element. Since the focal length is fixed to 4.2 m by the beamline design, the collimated laser beam size remains to tune the focal spot size. However, the laser intensity is limited by the damage threshold of the beamline mirrors, and a decrease of the collimated beam size must not lead to an increase of intensity. The focal spot size can consequently only be increased at the cost of the laser pulse energy by placing an aperture in the beam path upstream of the parabolic mirror. Assuming a circular, flat intensity distribution, the final pulse energy scales as

$$E_{\mathrm{pulse,fin}} = E_{\mathrm{pulse,ini}}\frac{w_{0,\mathrm{ini}}^2}{w_{0,\mathrm{fin}}^2}. \tag{3.39}$$

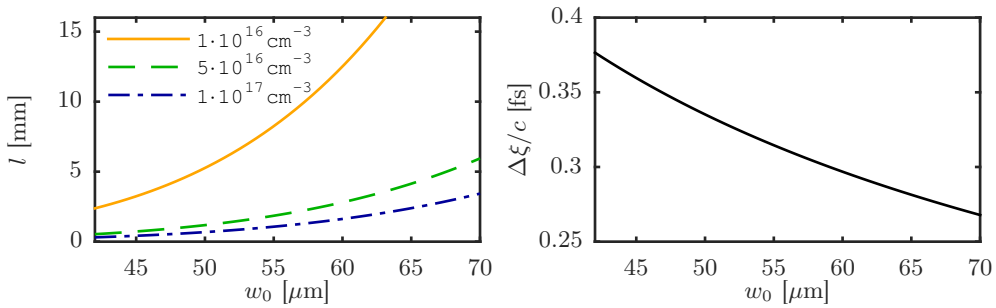

(a) Target length.

(b) Temporal resolution.

Figure 3.11 – Target length needed to imprint a beam divergence of 6.5 mrad depending on the laser spot size in focus w_0 (a). a_0 reduces with $a_0 \propto w_0^{-2}$ (see text). The larger w_0 allows for a larger electron beam size $\sigma_y \propto w_0^{2/3}$, leading to a better theoretical temporal resolution (b), assuming a longer target to imprint the same divergence.

The laser strength parameter a_0 is consequently reduced to

$$a_{0,\mathrm{fin}} = a_{0,\mathrm{ini}} \frac{w_{0,\mathrm{ini}}^2}{w_{0,\mathrm{fin}}^2}, \tag{3.40}$$

accounting for both the energy loss at the hypothetical aperture and for the larger spot size.

Figure 3.11 shows the target length needed to imprint the beam divergence of 6.5 mrad on the bunch for varying laser spot size and different plasma densities.
Please note that the assumed bunch length is, unlike shown in table 3.2, only $\sigma_z/c = 2\,\mathrm{fs}$. The reason for this assumption is that the design presented here aims at the best possible resolution for the TDP at REGAE. Due to the limited dynamic range caused by the low beam energy, see eq. (3.38), this can only be achieved for ultrashort bunches. For longer bunches, the voltage and consequently the resolution will have to be scaled accordingly to guarantee a small enough divergence. The design will assume ultrashort bunches, and scaling laws will be discussed at the end of the chapter.

The other laser and bunch parameters are like in table 3.2. The optimum transverse beam size $\sigma_r = \sigma_y = 7\,\mu\mathrm{m}$ is calculated using equation (3.20) for the given bunch length and a laser spot size of $w_0 = 42\,\mu\mathrm{m}$. As the laser spot size varies in fig. 3.11, the electron beam size follows like $\sigma_y \propto w_0^{2/3}$ like in eq. (3.20). This treatment includes the influence of higher order correlations of the deflecting field and of the emittance. It

does not include beam loading effects, as these are negligible for the low bunch charge at REGAE.

The density range considered in this study is limited on the upper end to around $n = 1 \cdot 10^{17}\,\mathrm{cm}^{-3}$ by the gas flow into the target chamber [24]. On the lower end it is limited by the achievable field gradient, which will be seen later.

From fig. 3.11 it seems that a long target is favorable to increase the resolution. However, as mentioned above, long plasma lengths make the setup more susceptible towards detrimental effects such as bunch offsets or elongation. These will be discussed in the following.

Bunch Lengthening During TDP Transition

One effect that is increasingly relevant for bunches of low kinetic energy is the bunch lengthening in the TDP.

The expression for the accelerating fields in the vicinity of $y = w_0/2$ is given in eq. (3.9) on page 29. The dependence of the longitudinal field E_z on the transverse coordinate y in general causes an increase of slice energy spread as in any TDS cavity. In addition, for low energy bunches, this also leads to a significant velocity difference between particles at different y positions. Due to the velocity difference the bunch will elongate during its transition through the TDS or TDP. The longitudinal shift of a particle at a position y compared to a reference particle at exactly $y_{\mathrm{ref}} = w_0/2$ can be calculated as [50]

$$\Delta z = -\frac{eVk_pl}{2cp\beta\gamma^2}(y - w_0/2)\cos(k_p\zeta), \tag{3.41}$$

where p is the average bunch momentum. The bunch length consequently increases as

$$\sigma_z^2 = \sigma_{z,\mathrm{ini}}^2 + \left(\frac{eVk_pl\sigma_y}{2cp\beta\gamma^2}\cos(k_p\zeta)\right)^2, \tag{3.42}$$

where $\sigma_{z,\mathrm{ini}}$ is the bunch length at the start of the plasma. As discussed in [50], since the longitudinal shift scales directly proportional to both the voltage and the structure length, $\Delta z \propto Vl$, while the theoretical resolution from eq. (3.5) scales inversely proportional only to the voltage, $\Delta\xi \propto 1/V$, this favors short deflecting structures of high field amplitude, providing the same voltage V over a shorter length l.

Figure 3.12(a) shows the bunch lengthening in the TDP depending on the laser spot size. As before, $a_0 \propto w_0^{-2}$. The plasma length is adjusted like in figure 3.11(a) to achieve the same beam divergence of 6.5 mrad after the target for all spot sizes, and the electron beam size is scaled like $\sigma_y \propto w_0^{2/3}$ as before. The solid black line indicates

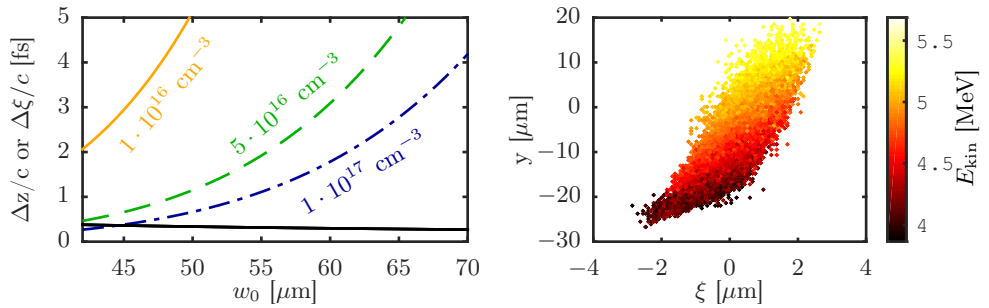

(a) Bunch lengthening.

(b) Elongated bunch.

Figure 3.12 – (a) The REGAE bunch lengthening $\Delta z/c$ according to eq. (3.41) depending on the laser spot size w_0, when scaling the target length as before to keep the imprinted divergence fixed. The theoretical resolution $\Delta\xi/c$ (see eq. (3.5)) is shown in black for reference. (b) Elongated bunch in low density ($n = 1 \cdot 10^{16}\,\mathrm{cm}^{-3}$) TDP with color coded kinetic energy. An energy resolved measurement allows to access the bunch length for slices in y. For details see text.

the temporal resolution $\Delta\xi/c$, like in figure 3.11(b), for reference. As expected from eq. (3.41), the effect is strongest for the lowest density since the low density targets rely on comparably long plasma lengths at lower field amplitude.

As the bunch lengthening is caused by the slope of the longitudinal field E_z in y, a correlation of the final z position with the y-coordinate and also with the kinetic energy can be expected. The energy resolved measurement in the spectrometer then allows to diagnose the bunch length of an energy slice, which for an initially uncorrelated energy distribution also corresponds to a slice in y. For illustration, an ASTRA simulation of a low density TDP with $n = 1{\cdot}10^{16}\,\mathrm{cm}^{-3}$ and $l = 2.4\,\mathrm{mm}$ is shown in figure 3.12(b). The laser spot size is $w_0 = 42\,\mu\mathrm{m}$. The depicted bunch has propagated through 1.8 mm of plasma, and the bunch length has increased from initially 2 fs rms to 2.7 fs rms. However, the length of the individual energy slices has not increased, for example the slice around $\pm 1\,\%$ of the central energy of 4.6 MeV is still 2 fs rms long. If the bunch is then diagnosed in the spectrometer, the slice length can be measured, and also the central, i.e., optimally streaked, slice can be determined as the one that does not accumulate a net angle. The bunch lengthening therefore is not a show-stopper for the TDP design at REGAE. However, the plasma length is still limited by the induced offset.

Bunch Offset from TDP

The low kinetic energy leads to an offset of the bunch centroid during the TDP transition, as the bunch slips through the zero crossing of the deflecting field E_y. It first accumulates a momentum change in one direction that is then compensated by the fields of opposite sign after crossing $E_y = 0$, and a net offset remains. Owing to the similarity of the fields in the TDP and in a conventional TDS cavity, this offset can be calculated in the same way as for a conventional cavity and has been derived for those in [50] to

$$x_{\mathrm{off}} = \frac{eV}{12cp_z}\frac{\partial\Psi}{\partial z}l^2, \tag{3.43}$$

with the phase slippage defined as

$$\frac{\partial\Psi}{\partial z} = k_p\left(v_{\mathrm{gr}}/c - \beta\right). \tag{3.44}$$

Here, $\Psi = k_p\zeta$ is the phase of the bunch in the wake, v_{gr} is the laser group velocity and $\beta = v_z/c$ is the normalized beam velocity. Since eq. (3.43) scales directly with the structure length l in addition to the voltage V, short structures with large voltage are favorable in order to minimize the offset [50].

If the offset is very large the bunch leaves the maximum of the streaking field E_y in y. This does not only reduce the streaking voltage, but also causes a linear correlation of the deflection with the y coordinate of the bunch, which limits the resolution. The offset therefore needs to be much smaller than the laser spot size, as this determines the wakefield width.

For the same assumptions as before, namely an increasing laser spot size with $a_0 \propto w_0^{-2}$ and the optimum electron beam size $\sigma_y \propto w_0^{2/3}$, and an adjusted plasma length according to figure 3.11(a) to achieve an imprinted divergence of 6.5 mrad, the offset at the end of the TDP depending on the laser spot size can be seen in figure 3.13. From the figure it is apparent that for a density of $1 \cdot 10^{16}\,\mathrm{cm}^{-3}$ even the offset introduced for the smallest possible (design) spot size of $w_0 = 42\,\mu\mathrm{m}$ is very large with $x_{\mathrm{off}} = 18\,\mu\mathrm{m} > w_0/4$. The TDP at REGAE therefore needs to be designed with a larger density, or else temporal resolution has to be sacrificed to reduce the bunch offset.

Depending on the initial phase of the bunch in the wake, also a net angle instead of an offset can be introduced due to slippage [50]. One could then think about injecting the bunch with an initial angle, which is compensated in the TDP. This might help to push the density limit a bit lower than allowed for a case where the injection phase leads to a pure offset. However, the bunch would still have an offset at the center of the plasma target, which will be reduced to zero again at its exit. The reduction

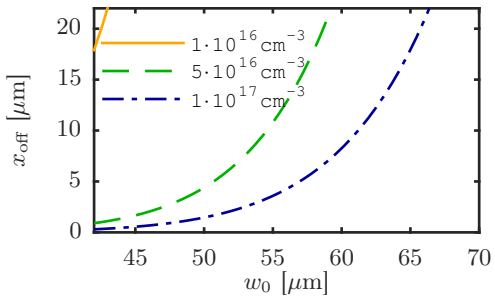

Figure 3.13 – Offset at the end of the TDP depending on the laser spot size w_0, with $a_0 \propto w_0^{-2}$ and $\sigma_y \propto w_0^{2/3}$ as before. The plasma length is scaled according to fig. 3.11(a) to achieve the same imprinted divergence.

of the streaking voltage due to the offset and the linear correlation of the transverse momentum p_y with y would thereby be reduced compared to a pure offset, but it would not be completely removed.

Another option is to taper the plasma density to remove the slippage between laser and bunch, as proposed in [68] for laser plasma acceleration. Since the REGAE bunch is slower than the laser group velocity in the plasma at the densities considered, this calls for a density down ramp. For the sake of conceptual and experimental simplicity, and also since it seems very challenging to achieve a precise density taper at such a low density and small length scale, neither this option nor the introduction of an initial angle is pursued here.

Summary: Resulting Parameter Set for the TDP Design at REGAE

The streaking voltage is limited by the imprinted divergence. A higher resolution can only be achieved by increasing the possible electron beam size and at the same time increasing the laser spot size. To increase the laser spot size at constant voltage, however, calls for a longer plasma length.

Apart from the bunch lengthening which could be accounted for using the electron spectrometer, the low bunch energy at REGAE leads to a beam offset in the TDP which ultimately limits the plasma length. With several μm offset over the TDP, and since the laser spot size determines the tolerance to the offset, this is a strong effect. For this reason, and also since it will introduce additional experimental effort, the TDP design presented here will keep the REGAE design of $w_0 = 42\,\mu$m.

REGAE bunch (Gaussian)	
kinetic energy E_{kin}	5.6 MeV
transverse emittance $\epsilon_{\mathrm{n},x} = \epsilon_{\mathrm{n},y}$	0.1 mm mrad
bunch charge Q	100 fC
bunch length σ_z/c	2 fs
beam size σ_r	7 μm
position behind driver laser ζ_{bunch}	-148 μm
ANGUS driver laser (Gaussian)	
spot size w_0	42 μm
pulse length (FWHM)	100 fs
normalized vector potential a_0	0.9
plasma	
density n	$5 \cdot 10^{16}\,\mathrm{cm}^{-3}$
length l	0.5 mm
longitudinal profile	flat top
expected resulting parameters	
theor. resolution $\Delta\xi$	0.39 fs
imprinted divergence	6.5 mrad
imprinted offset	0.9 μm
final energy	4.3 MeV
final relative rms energy spread	10 %

Table 3.3 – Design parameters for the TDP experiment with maximum temporal resolution at the REGAE external injection experiment.

The remaining free parameter is the plasma density, which, however, is also limited by the bunch offset on the lower end ($n > 1 \cdot 10^{16}\,\mathrm{cm}^{-3}$) and by the gas flow in the target chamber on the upper end (around $n \leq 1 \cdot 10^{17}\,\mathrm{cm}^{-3}$ [24]). Therefore, for the design shown here, the intermediate density of $n = 5 \cdot 10^{16}\,\mathrm{cm}^{-3}$ is chosen. This density is favorable also from an experimental point of view since it requires a plasma length of $l = 0.53\,\mathrm{mm}$, while for $n = 1 \cdot 10^{17}\,\mathrm{cm}^{-3}$ the plasma length would be even shorter with only $l = 0.31\,\mathrm{mm}$. In the following, the plasma length is set to $l = 0.50\,\mathrm{mm}$ to have a round number for this study. Furthermore, the plasma profile is a flat top without significant ramps. This is of course not realistic, but the exact plasma profile is not important since the voltage will be given by the integral over the plasma target, so that deviations will be averaged out.

The summarized parameter set can be found in table 3.3.

3.3.3 Numerical Simulations

The REGAE setup including beam optics and spectrometer is simulated with ASTRA. The plasma module in ASTRA uses the linear wakefield model as given by eqs. (2.10)-(2.12). This does not include nonlinearities such as wave front curvature. As $a_0 = 0.9$ in this example, nonlinearities can already play a role here. The plasma interaction is therefore simulated with the PIC code WARP in 3D. The electron phase space extracted from WARP is then loaded into ASTRA where the beam is transported through the magnetic optics and the spectrometer.

Beam Transport Behind the Target

The beam transport between the TDP and the electron spectrometer has to fulfill three main requirements. First, the highly divergent beam needs to be transported without clipping at the beam pipe, second, for best temporal resolution a phase advance in y of $90° + k \cdot 180°$, $k \in \mathbb{N}_0$, is necessary, and third, for best energy resolution a phase advance in x of $m \cdot 180°$, $m \in \mathbb{N}_0$, i.e., a focus in the x plane on the spectrometer screen, needs to be achieved. The last two requirements ensure that an imaging of the full longitudinal phase space can be achieved.
Behind the target, two solenoids are installed, the permanent magnet solenoid (PMS) shortly behind the target, and an electrical solenoid Sol6/7 at roughly 0.9 m downstream of the target, compare fig. 3.10. In front of and behind Sol6/7 also two quadrupoles, Q_a and Q_b, are positioned, which are intended to be used with electron beams accelerated to higher energies by the plasma wakefield in the external injection experiment. The electron spectrometer (eSpec) follows at around 2.6 m behind the target.

The mean kinetic energy of the bunch positioned at one plasma wavelength behind the driver is reduced to 4.6 MeV. This number is taken from the PIC simulations shown later, and it agrees with the expected 4.3 MeV from equation (3.10). The low energy allows for the efficient use of the solenoids PMS and Sol6/7, providing a symmetric focusing in both transverse planes. However, Sol6/7 is not used here. Instead, the quadrupole doublet is employed. This provides the freedom to independently tune both the x and y plane, and furthermore the quadrupoles are well suited for transversely large beams. In contrast, the solenoid would introduce abberations due to its field nonlinearities.

The large divergence after the target makes the use of the PMS inevitable. It provides initial focusing to prevent clipping till the first quadrupole, Q_a. To avoid field nonlinearities inside the PMS, the distance between target center and PMS center is chosen

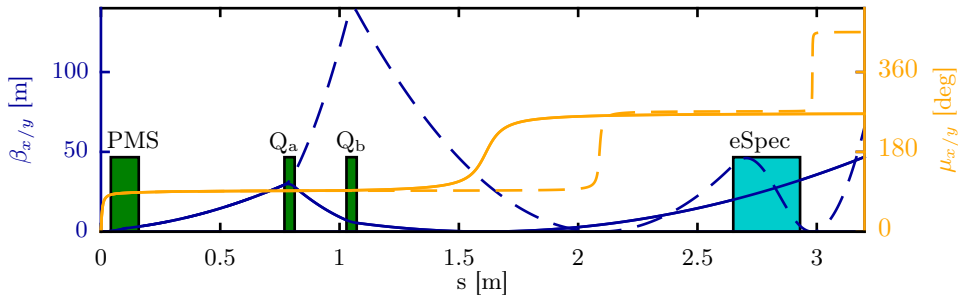

Figure 3.14 – Beta function and phase advance of the unstreaked beam behind the target. With an intermediate focus between the quadrupole doublet and the spectrometer, a phase advance of 270° is achieved for the y plane (solid lines). The focusing properties of the dipole leads to a focus in x (dashed) on the spectrometer screen at around $s = 3\,\mathrm{m}$.

small with 10 cm, which is still below the expected PMS focal length for 4.6 MeV of 13 cm.

Due to the small electron beam size and corresponding beta function at the target position the phase advance through the PMS and drift to Q_a already amounts to 90°. Yet, it is necessary to focus the beam again with the doublet as otherwise it would clip in the spectrometer. Tuning Q_a and Q_b to achieve an intermediate focus in the y plane roughly halfway between the doublet and the eSpec ensures passage through the eSpec while providing a phase advance of around 270° in total between target and detector. Here, Q_a focuses the y plane, in order to quickly reduce the beam size in the streaking direction. The electron spectrometer strongly focuses the beam in the x plane. In order to achieve a focus in x on the screen, the quadrupoles focus the beam also in the x plane to an intermediate focus in front of the spectrometer. The beam optics design is found following the procedure shown in [24], which employs the matrix formalism for the beam optical elements. For the sake of brevity, the treatment given in [24] is not repeated here.
The beta function and phase advance for an unstreaked 4.6 MeV beam can be seen in fig. 3.14. The gradients of Q_a and Q_a are $-1.2\,\mathrm{T/m}$ and $1.1\,\mathrm{T/m}$, respectively, which are realistic values.

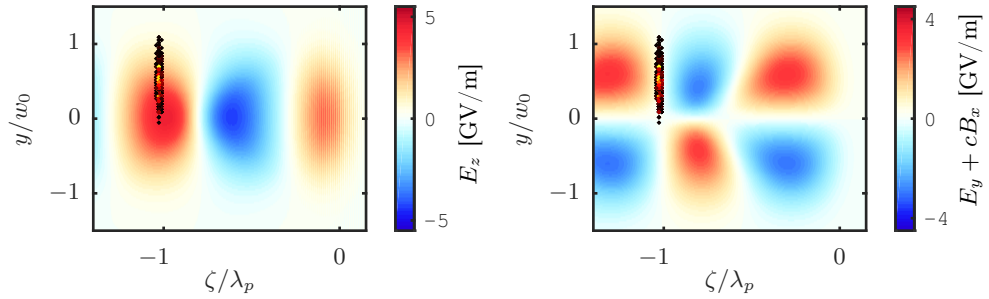

(a) Longitudinal field.

(b) Streaking fields.

Figure 3.15 – Accelerating and streaking fields at $z = 0.25\,\mathrm{mm}$ in the plasma from a WARP 3D simulation. The onset of nonlinearities leads to a curved wave front around $\zeta = -\lambda_p/2$, which leaves the zero-crossing of $E_y + cB_x$ at $\zeta = -\lambda_p$ as the optimum driver to witness distance for streaking. A 2 fs long bunch is shown for illustration.

PIC Simulations

The plasma interaction is simulated with Warp 3D in the laboratory frame. The simulation box has a size of $305\,\mu\mathrm{m} \times 168\,\mu\mathrm{m} \times 168\,\mu\mathrm{m}$ with $12201 \times 86 \times 86$ cells. The laser and electron bunch parameters are motivated above and are shown in table 3.3.

A curved wave front due to wakefield nonlinearities can severely hamper the temporal resolution, as it causes a correlation of the streaking signal with the transverse coordinate of the bunch. For the parameters discussed here, the wave front at half a plasma period behind the driver is strongly curved, while the wave front at one plasma period behind the driver it is almost flat, see figure 3.15. The delay between driver and bunch consequently needs to be chosen as $\zeta_{\mathrm{bunch}} = -\lambda_p$.

Two parameter scans are performed in WARP. First, for a constant bunch length of $\sigma_z/c = 2.0\,\mathrm{fs}$, the delay between driver laser and witness bunch is scanned by $\pm 10\,\mathrm{fs}$ in 1 fs steps around the ideal ζ_{bunch}/c. Second, the bunch length is varied from $\sigma_z/c = 0.1\,\mathrm{fs}$ to $\sigma_z/c = 4.0\,\mathrm{fs}$ to determine the maximum resolution of the TDP at REGAE.

After the plasma interaction, the 6D phase space from the PIC code is tracked with ASTRA through the beam optics and the spectrometer. The simulated spectrometer

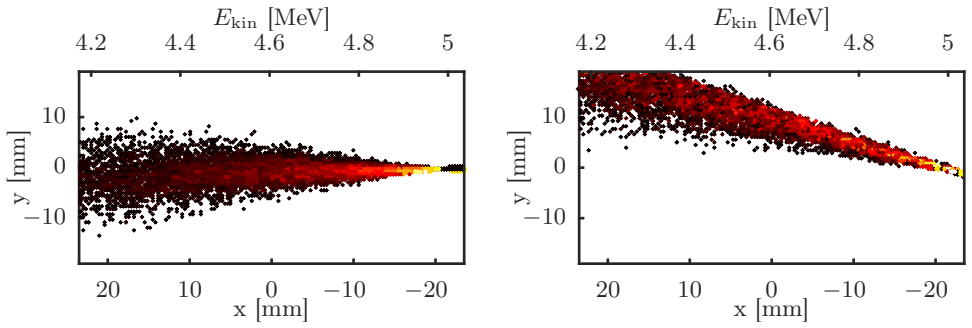

(a) Optimum delay.

(b) 10 fs shift.

Figure 3.16 – Simulated screen image of the spectrometer for a 2 fs bunch streaked at the optimum delay in the wake (a) and with a 10 fs larger delay (b) between driver and witness. The axis limits correspond to the screen size (x) or beam pipe width (y). The large energy spread imprinted by the wakefield causes a smearing of the bunch over the complete energy acceptance of the spectrometer in x. Higher energies are focused directly on or near to the screen, their phase advance consequently is smaller than 270°.

screen image for a 2 fs long bunch can be seen in figure 3.16. The x axis limits correspond to the total screen width of 47 mm, while the y axis is limited by the beam pipe of 38 mm total width. Due to the large energy spread imprinted by the TDP the phase space is distributed in the dispersion plane x over the complete screen. It can also be seen that the focus of the high energy tail of the bunch is at or near the spectrometer screen. The phase advance of this energy range is smaller than the required 270°. This, as well as the chromatic bunch lengthening, implies that only the central (design) energy can be used for the measurement.
Figure 3.16(b) shows the simulated screen image for a bunch that is injected into the TDP with a delay between driver and witness that is 10 fs larger than the optimum one. As the bunch here already clips in y at the spectrometer chamber, the ten femtoseconds represent a limit for the calibration delay scan as well as for the maximum resolvable bunch length. Experimentally, a steering magnet could be used for the calibration, so that the bunch is centered on the screen for each delay. The magnet current could then be translated into a deflection. In that sense, the aperture of the spectrometer chamber only limits the bunch length but not necessarily the delays used for the calibration.
In fig. 3.16(b) one can also see that the intermediate focus changes the sign of the deflection: After the plasma target a bunch of this delay steers towards the negative y direction, and this is flipped in the focus between the quadrupole doublet and the

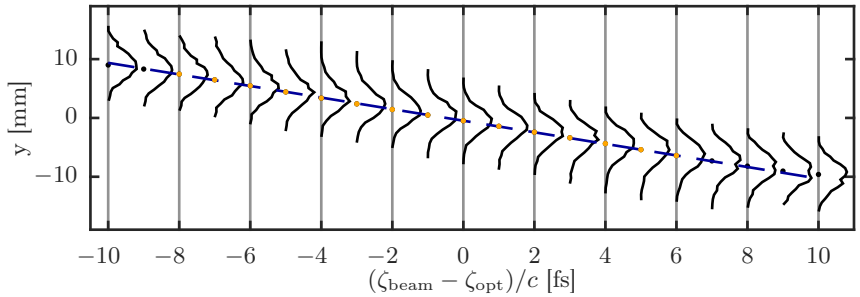

Figure 3.17 – Calibration of the TDP at REGAE with a scan of the witness delay ζ_{beam}/c around the optimum delay ζ_{opt}/c. Black curves are the bunch histogram in y on the spectrometer screen, the dots indicate the centroid. A linear fit (dashed blue) to those centroids where a minimum of 95 % of the bunch charge hit the screen (yellow dots) allows to correlate the y coordinate to the time information.

eSpec.

For the calibration, the central 10 mm in x of the screen are used. In order to reduce the influence of field nonlinearities or outliers on the result, the bunch centroid is calculated with the median. The y-offset of the bunch centroid on the screen is then correlated with the delay between driver and witness, a calibration that includes also the effect of the beam optics, see figure 3.17. There, the black lines show the bunch histogram to the y axis of the spectrometer detector, obtained for different delays. The dots show the bunch centroid, while yellow indicates that at least 95 % of the initial bunch charge hit the screen. Only those shots are used for the linear fit (dashed blue) that gives the time calibration with $\Delta y/\Delta t = -0.98\,\mathrm{mm/fs}$.

Knowing the calibration, it is possible to infer the initial bunch length from the measured beam size in y at the detector position. This is shown in figure 3.18 for four different bunch lengths, $\sigma_z/c = 0.1\,\mathrm{fs}$, $0.75\,\mathrm{fs}$, $2.0\,\mathrm{fs}$ and $4.0\,\mathrm{fs}$. Not surprisingly, the short bunch is not resolved perfectly by the TDP as it is shorter than the expected temporal resolution of 0.39 fs. For the intermediate lengths the reconstruction is very accurate, while the measured bunch length of the 4 fs case is actually too small. This error and also the deviation of the beam from its original Gaussian shape is caused by the large beam size of $\sigma_y = 1.2\,\mathrm{mm}$ in the PMS making the beam prone to focusing errors from field nonlinearities of the solenoid. With a divergence of $\sigma_{y'} = 11.4\,\mathrm{mrad}$ after the target, this bunch length is already very near to the estimated maximum transportable divergence after the target of 13 mrad. It consequently presents the limit to the dynamic range of the TDP at REGAE.

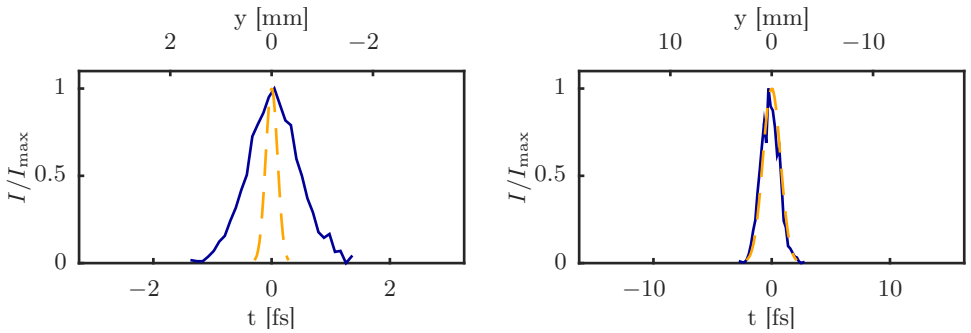

(a) $\sigma_z/c = 0.1$ fs.

(b) $\sigma_z/c = 0.75$ fs.

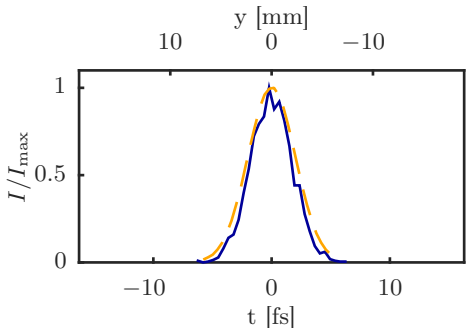

(c) $\sigma_z/c = 2$ fs.

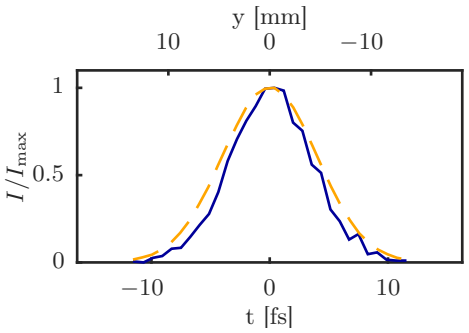

(d) $\sigma_z/c = 4$ fs.

Figure 3.18 – Initial (dashed yellow) and reconstructed (blue) current profile at REGAE for different initial bunch lengths. y refers to the vertical coordinate of the spectrometer screen and its limits agree with the screen size in figs. (b)-(d). Note the different scale for the short bunch in (a).

The temporal resolution is retrieved from the 0.1 fs case as

$$\Delta\xi = \sqrt{\sigma_{t,\mathrm{reconst}}^2 - \sigma_{t,\mathrm{ini}}^2} = 0.43\,\mathrm{fs}, \tag{3.45}$$

which agrees well with the 0.39 fs expected theoretically.

3.3.4 Calibration with Arrival Time Jitters

The tolerance of the calibration to arrival time jitters between laser and bunch is estimated in this paragraph. Due to their run time, the many simulations necessary for this cannot be done in the Particle-In-Cell framework. They are therefore done purely with Astra that uses the linear wakefield model for the plasma interaction. Furthermore, in contrast to the tolerance simulations for the SINBAD example case in section 3.2.3, it is not possible to map the complete plasma wavelength to the spectrometer screen, as the deflection is too large to capture beams positioned far away from the optimum streaking delay in the wake. The calibration therefore needs to be extracted from a linear fit like in figure 3.17, however, to the jitter-afflicted data.

Figure 3.19 shows Astra simulations of the calibration for different magnitudes of the rms arrival time jitter. 50 individual shots are tracked through the plasma and the beam optics to the screen for 21 different average beam positions in the wake ζ_{beam}. As before, all parameters are like in table 3.3, and especially the rms bunch length is $\sigma_z/c = 2\,\mathrm{fs}$. The calibration is obtained from a linear fit (dashed yellow) to the median of the centroid of all 50 shots (solid blue) at each delay. For comparison, the ideal calibration without jitters is repeated with Astra (dashed green line) and with $\Delta y/\Delta t = -1.1\,\mathrm{mm/fs}$ shows a slightly larger deflection than the Warp calibration of $-0.98\,\mathrm{mm/fs}$.
This can be directly traced back to the slope of the phase space $\partial p_y/\partial\xi$ after the TDP, which is larger by 7 % in Astra compared to Warp. The origin of this effect can only be the linear wakefield model employed in Astra. This can be expected as the normalized vector potential of the laser used in the REGAE parameter set, $a_0 = 0.9$, does not fulfill the requirement of $a_0^2 \ll 1$ for the linear regime. However, since the differences to the full PIC code are small here, the model is used for the jitter studies nonetheless. In fact, such a study is only possible with an analytical model as employed in Astra, where one run from target to spectrometer finishes within a few seconds, but not with the full PIC code, where one tracking through the plasma costs about 2000 CPU-hours on a supercomputer.
The calibration obtained from the jittering simulated data ranges from $\Delta y/\Delta t = -1.0\,\mathrm{mm/fs}$ for 2 fs rms to $\Delta y/\Delta t = -0.57\,\mathrm{mm/fs}$ for 14 fs rms arrival time jitter. All

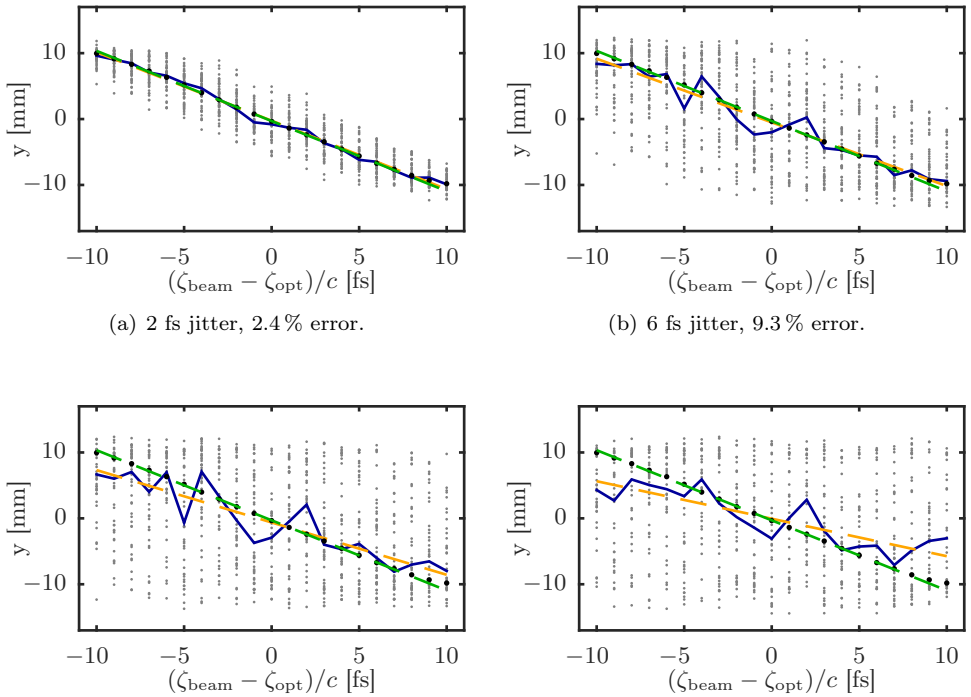

(a) 2 fs jitter, 2.4 % error.

(b) 6 fs jitter, 9.3 % error.

(c) 10 fs jitter, 25 % error.

(d) 14 fs jitter, 47 % error.

Figure 3.19 – Jitter-afflicted TDP calibration at REGAE. 50 shots are taken at each delay (gray dots). A linear fit (dashed yellow) to the median of their centroids (solid blue) gives the calibration. For comparison, an ideal, non-jittering calibration is shown (black dots and dashed green line). The error between the two linear slopes due to the arrival time jitter increases strongly for larger jitter. Also, a systematic error is visible, as charge is clipped in many shots and the bunch centroids erroneously tend towards the screen center.

relative errors compared to the non-jittering calibration are given in the figure captions.
Obviously, the jitter-afflicted calibration is lower than the ideal one for all jitter magnitudes. The reason for this is a systematic error, as beams clip at the beam pipe due to the large divergence and steering after the TDP. For example, even for the small jitter of 2 fs, only in those simulations with average delay $(\zeta_{\mathrm{beam}} - \zeta_{\mathrm{opt}})/c$ between -1 fs and 2 fs at least 90 % of the bunch charge reached the screen for all 50 shots. However, only the charge hitting the screen can contribute to the centroid calculation, which will therefore be systematically smaller than the true value.

The question as to what is a tolerable error in the calibration is somewhat arbitrary if no direct application or design goal is fixed. For the demonstration of phase space linearization [65], for example, an accuracy of 50 % might be sufficient if the bunch is indeed very short and it can be excluded that such a bunch length can be achieved with the standard operation mode. For the treatment here, the limit for the arrival time jitter for the TDP design with the best resolution shall be fixed to 6 fs, as here a clear correlation of the shots is still visible in figure 3.19(b). However, this is indeed not a very physical criterion, and also one could expect that other calibration measures could improve this tolerance, such as a cross-calibration with another bunch length measurement, e.g. the conventional TDS cavity or a CTR measurement. Also it might be possible to calibrate the TDP at a lower laser energy where the setup is more forgiving to timing errors and scale the obtained calibration to the highest energy. Furthermore, the calibration with the help of a steerer magnet so that the average deflection is zero for each delay might improve the tolerance to jitters, as clipping would occur only for larger timing jitters. Please note that this is a requirement on the short-term jitter and not necessarily on the long-term drift.

3.3.5 Scaling the Design

To summarize, the best temporal resolution achievable with the TDP at REGAE is around $\Delta\xi/c \geq 0.4$ fs. With this resolution, bunch lengths up to $\sigma_z/c = 4$ fs can be measured. Initially longer bunches accumulate a very large divergence and the beam optics is not able to capture them anymore. For this parameter set, the arrival time jitter should not be significantly larger than 6 fs rms.
So far lacking sophisticated diagnostic devices at REGAE such as the proposed TDS cavity [50] the electron bunch length is currently not known. Also, the arrival time jitter including all error sources such as the complete laser chain is yet unknown. It is therefore highly desirable to be able to scale the mentioned TDP parameters towards longer bunches and larger jitters.

According to eqs. (3.5) and (3.6) the resolution scales as $\Delta\xi \propto V^{-1} \propto a_0^{-2}$. The divergence, on the other hand, scales as $\sigma_{y',\mathrm{TDP}} \propto V \propto a_0^2$, see eq. (3.37). As the tolerance to timing jitters is dominated by the dynamic range of the detection, i.e., by clipping at the beamline, it can be expected to scale directly with $1/\sigma_{y',\mathrm{TDP}} \propto a_0^{-2}$. Due to the low bunch charge of 100 fC beam loading can be neglected, which would otherwise contribute stronger for lower laser-driven wakefield amplitude. The parameters of the TDP at REGAE design, i.e., the resolution, the acceptable bunch length and the timing jitter, consequently increase linearly with decreasing laser intensity, or experimentally with the laser pulse energy. It is therefore straightforward to relax the requirements, like those on the arrival time jitter, by reducing the laser pulse energy.

3.4 Summary

In the previous paragraphs a novel longitudinal phase space diagnostics has been presented. The method harnesses the strong transverse fields of plasma wakefields to streak ultrashort electron bunches, thereby providing a temporal resolution well below one femtosecond.

An electron bunch from an external source – be it a conventional accelerator or a previous plasma stage – is injected into a laser-driven linear wakefield. It is displaced transversely with respect to the driver to the maximum of the transverse fields, and it is injected longitudinally at the zero-crossing of these fields by choosing the driver to bunch delay. During the transition through the plasma stage the bunch accumulates a transverse momentum change that correlates with its longitudinal coordinate. In a drift or beam optics the transverse momentum and consequently the time information can directly be mapped to the experimentally easily accessible transverse coordinate. Apart from bunch properties such as normalized emittance and beam size, the temporal resolution is determined by the length of the plasma stage, the transverse field amplitude, and the plasma wavelength. Since plasma wakefields feature both large field amplitudes and short wavelengths the TDP can achieve very high temporal resolution even with plasma targets of only a few millimeters length. For the exemplary numerical simulations shown here with parameters of the proposed SINBAD linac, the theoretical resolution is as low as 96 attoseconds.

The diagnostics is especially well suited for transversely focused ultrashort electron bunches as the limits on the longitudinal and transverse size of the diagnosed bunch are given by the plasma wavelength and the laser spot size. However, this also implies that the small transverse beam size leads to a loss in resolution compared to conventional TDS cavities where the bunch can be large. Furthermore, since beam loading

can influence the wakefield shape, the best temporal resolutions can be achieved for low bunch charge. Experimentally, a high-power laser system that is synchronized to the probed electron bunch is required. All of these boundary conditions are naturally fulfilled by conventional accelerators designed for external injection into a plasma booster stage, i.e., hybrid accelerators, or by laser-plasma accelerated beams. LPA beams are intrinsically synchronized to the laser and arrival time jitters therefore may play only a minor role. On the other hand their charge can be much higher than in conventional injectors, which are limited by space charge effects at the photocathode, and due to beam loading the high charge can lead to resolution degradation. In the case of hybrid accelerators, where a sophisticated synchronization system needs to be installed in any case, the TDP does not require any additional equipment. In contrast, it provides the possibility to measure the initial, injected longitudinal bunch profile directly at the injection position – a task that would not be feasible even with a dedicated TDS cavity.

A design for the experimental demonstration of the proposed concept is presented for the external injection experiment at REGAE. Here, the main challenge is posed by the low kinetic energy leading to a large divergence and quick deformation of the bunch still within the plasma target. This eventually limits the theoretical resolution to 0.4 fs, under the assumption of an ultrashort, 2 fs electron bunch with a normalized transverse emittance of 0.1 mm mrad. Owing to the imprinted divergence and resulting limited dynamic range, the temporal resolution scales with the electron bunch length. Experimentally straightforward this can be achieved by adjusting the laser pulse energy, and provides the benefit to also scale the tolerance to arrival time jitters accordingly.
Compared to conventional TDS cavities the TDP provides an additional advantage that is especially important for low energy beams like those at REGAE, which is to drastically reduce errors from bunch deformation within the structure. The TDP at REGAE is therefore a promising option to push the temporal resolution down below one femtosecond, and thereby to provide the diagnostics tool to prove the concept of longitudinal phase space linearization proposed recently [65, 24].

4 Emittance Conservation and Divergence Reduction

Plasma wakefields can sustain high accelerating field gradients, making them very attractive as compact particle accelerators. However, these high longitudinal fields are also accompanied by strong focusing fields. In order to avoid emittance growth, the beta function of a bunch accelerated in a wakefield needs to be matched to these focusing fields [69]. This requires extremely small beta functions around or below 1 mm, which is very challenging for the beam optics that capture the beam after the plasma, and – in the case of external injection – also for the injection beam optics. Furthermore, the large divergence of the beam leads to chromatic emittance growth in the drift after the plasma-vacuum boundary [29], that can quickly spoil the initially good emittance of laser-plasma accelerated beams [70, 71].

To capture the highly divergent beam after the plasma target, different strong focusing lenses have been proposed and demonstrated. Permanent magnet quadrupoles [72] achieve a gradient of up to 500 T/m, which comes at the cost of limited tunability. Furthermore, like all quadrupoles, they focus one plane and defocus the other plane, leading to even stronger emittance growth in this plane until it is focused by the next element.
Another approach is the recently re-discovered discharge capillary lens [73], of which the working principle was already proposed and demonstrated in 1950 in the context of ion beams [74]. A high current is pulsed through a discharge and the resulting azimuthal magnetic field symmetrically focuses charged particle beams with a gradient up to 3500 T/m. However, these devices feature a small aperture of only a few hundred microns up to a millimeter. As a large part of the driver laser also exits the plasma target and has to fit through the following apertures, the discharge capillary lens needs to be placed close to the target, which limits its effectiveness.
Making use of the laser to reduce the beam divergence has been proposed [75] and demonstrated [76] recently. In this scheme, a second, lower density jet or plateau is placed behind the target. The electron bunch diverges in the short drift between the two plasmas and is focused by the wakefield driven by the remainder of the laser pulse in the second jet.

Also the electron bunch drives a wakefield in a plasma and can be used to focus the bunch itself [77–79].

This chapter is concerned with a method to reduce the beam divergence with the help of adiabatic matching sections before the beam exits the target. This also relaxes the requirements on the beta function needed for external injection. Experimentally, the solution to catch the beam will surely be a combination of several concepts.
First, the origin of the emittance growth in the plasma and of the large divergence is discussed. The approach to circumvent this is then illustrated with examples of externally and internally injected beams.

The part of this chapter dealing with externally injected beams has been published in [80].

4.1 Causes for Transverse Beam Quality Degradation

This section gives an overview of the possible causes for emittance growth. The literature used is mainly [29, 81, 69], unless cited otherwise.

Note on Terminology: Divergence

Please note that throughout this work, the term "divergence" is used for the quantity $\sigma_{x'} = \langle x'^2 \rangle^{1/2}$, which is the standard deviation of the trajectory angles $x' = p_x/p_z$ of all particles in the bunch. It should not be confused with the quantity $(\sigma_x)'$, which is also called divergence, but refers to the change of beam size σ_x over z, $(\sigma_x)' = \mathrm{d}\sigma_x/\mathrm{d}z$. For example, in a free drift $\sigma_{x'}$ will be the same at all z positions, even if the bunch undergoes a focus. In contrast, $(\sigma_x)'$ will change. It is zero in the focus, negative in front of the focus, where the beam size decreases, and positive after the focus. Likewise, in a constant focusing channel where σ_x does not change, $(\sigma_x)'$ is zero, while $\sigma_{x'}$ is finite and will also change its value depending on the beam size and emittance.

Beam Emittance Definition

The transverse emittance is a measure for the beam quality. It is related to the area in phase space covered by the beam. The emittance connects the beam divergence to the beam size. In focus, the relation $\sigma_x \sigma_{x'} = \epsilon_{\mathrm{n},x}/\gamma$ holds, where γ is the relativistic Lorentz factor.

The normalized transverse phase space emittance is defined as [29]

$$\epsilon_{\mathrm{n},x} = \frac{1}{m_e c}\sqrt{\langle x^2\rangle\langle p_x^2\rangle - \langle x p_x\rangle^2}, \tag{4.1}$$

where the angle brackets denote the second central moment as

$$\langle x^2\rangle = \frac{\sum x^2}{N} - \left(\frac{\sum x}{N}\right)^2, \quad \langle x p_x\rangle = \frac{\sum x p_x}{N} - \frac{\sum x \sum p_x}{N^2}, \tag{4.2}$$

and $\langle p_x^2\rangle$ analogously to $\langle x^2\rangle$. The sum is performed over all N particles in the bunch.

Emittance can also be defined in the trace space, x-x', where $x' = p_x/p_z$. The normalized trace space emittance is defined as [29]

$$\epsilon_{\mathrm{tr,n},x} = \frac{\overline{p}_z}{m_e c}\sqrt{\langle x^2\rangle\langle x'^2\rangle - \langle x x'\rangle^2}. \tag{4.3}$$

For a mono-energetic beam, the normalized trace space emittance $\epsilon_{\mathrm{tr,n},x}$ is identical to the normalized phase space emittance $\epsilon_{\mathrm{n},x}$, as $p_z = \overline{p}_z$ is valid for all particles. For beams of finite energy spread, the behaviour of the phase space emittance can differ significantly from the one of the trace space emittance.

Phase Space Emittance Growth in a Drift

The phase space emittance of a beam of both large energy spread and large divergence grows in a drift, while the trace space emittance is conserved [29].

An illustration of this effect can be found in figure 4.1. A beam of emittance $\epsilon_{\mathrm{n},x,\mathrm{ini}} = \epsilon_{\mathrm{tr,n},x,\mathrm{ini}} = 1\,\mathrm{mm\,mrad}$ is initialized in focus (black dots) with a beam size of $\sigma_x = 3\,\mu\mathrm{m}$, a divergence of $\sigma_{x'} = 1.7\,\mathrm{mrad}$, a mean energy of $\bar{E}_{\mathrm{kin}} = 100\,\mathrm{MeV}$ and a relative rms energy spread of $\sigma_E/\bar{E}_{\mathrm{kin}} = 10\,\%$. After the drift of 0.1 m (blue shades) the trace space area is conserved as x' actually defines how far the particles are sheared in x during the drift. The phase space area, however, increases, as particles of same transverse momentum p_x but different kinetic energy have a different x'. The particles then separate in the phase space according to their energy. In this example, the phase space emittance $\epsilon_{\mathrm{n},x}$ after the drift is 5.7 mm mrad.

Following [29] the emittance in the drift can be calculated by accounting for the changing transverse position

$$x = x_0 + z x' \tag{4.4}$$

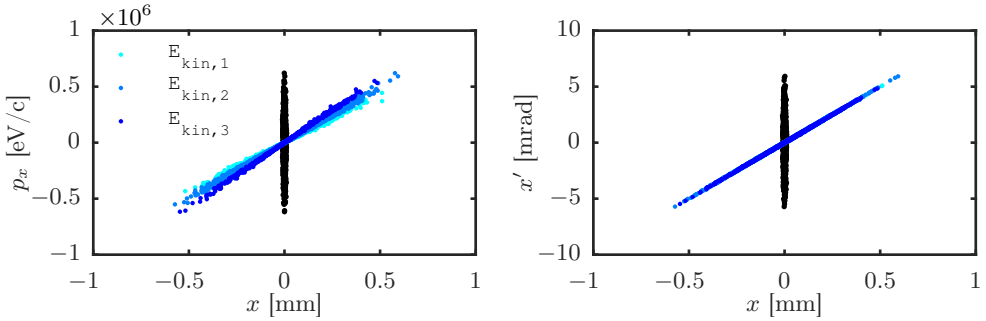

(a) Phase space.

(b) Trace space.

Figure 4.1 – Emittance evolution of a beam with large energy spread and high divergence in a drift. Initial particle positions are shown in black, particle positions after a drift are marked in shades of blue, where $E_{\mathrm{kin},1} < \bar{E}_{\mathrm{kin}} - \sigma_E$, $E_{\mathrm{kin},3} > \bar{E}_{\mathrm{kin}} + \sigma_E$, and $E_{\mathrm{kin},2}$ in between them. (b) The trace space area and consequently the trace space emittance $\epsilon_{\mathrm{tr,n},x}$ is conserved. (a) The phase space fans out depending on the kinetic energy, hence $\epsilon_{\mathrm{n},x}$ is not conserved in the drift. For beam parameters see text.

in eq. (4.1) as

$$\epsilon_{\mathrm{n},x}(z) = \frac{1}{m_e c}\sqrt{\langle (x_0 + zx')^2\rangle\langle p_x^2\rangle - \langle (x_0 + zx')\, p_x\rangle^2}\,. \tag{4.5}$$

Sorting the terms gives

$$\begin{aligned}\epsilon_{\mathrm{n},x}(z) = \frac{1}{m_e c}\big[\langle x_0^2\rangle\langle p_x^2\rangle - \langle x_0 p_x\rangle^2 + 2z\left(\langle x_0 x'\rangle\langle p_x^2\rangle - \langle x_0 p_x\rangle\langle x' p_x\rangle\right)\\ + z^2\left(\langle x'^2\rangle\langle p_x^2\rangle - \langle x' p_x\rangle^2\right)\big]^{1/2}\,.\end{aligned} \tag{4.6}$$

In the next step, $p_x = p_z x' = \gamma\beta_z m_e c x'$ is used and $\beta_z = 1$ is assumed for simplicity. The relativistic Lorentz factor γ can then be separated from the averages of x_0 and x' assuming they are statistically independent (as in [81]), i.e., that there are only negligible correlations between the energy and the transverse position:

$$\begin{aligned}\epsilon_{\mathrm{n},x}(z) = \frac{1}{m_e c}\big[\langle x_0^2\rangle\langle p_x^2\rangle - \langle x_0 p_x\rangle^2 + 2z\left(m_e^2c^2\langle\gamma^2\rangle\langle x_0 x'\rangle\langle x'^2\rangle - m_e^2c^2\langle\gamma\rangle^2\langle x_0 x'\rangle\langle x'^2\rangle\right)\\ + z^2\left(m_e^2c^2\langle\gamma^2\rangle\langle x'^2\rangle^2 - m_e^2c^2\langle\gamma\rangle^2\langle x'^2\rangle^2\right)\big]^{1/2}\,.\end{aligned}$$

With the definition of the rms energy spread $\sigma_\gamma^2 = \langle\gamma^2\rangle - \langle\gamma\rangle^2$ and $\sigma_{x'}^2 = \langle x'^2\rangle$ (assuming

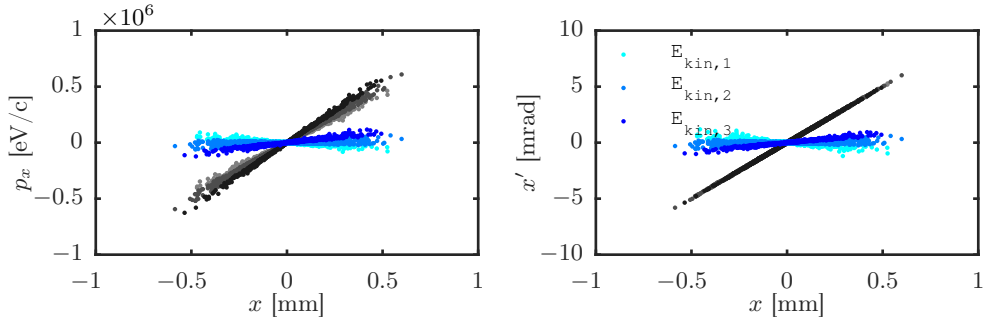

(a) Phase space. (b) Trace space.

Figure 4.2 – Emittance evolution of a large energy spread beam in a focusing element. Initial particle positions are shown in gray shades, particle positions after the focusing element are marked in shades of blue, where $E_{\mathrm{kin},1} < \bar{E}_{\mathrm{kin}} - \sigma_E$, $E_{\mathrm{kin},3} > \bar{E}_{\mathrm{kin}} + \sigma_E$, and $E_{\mathrm{kin},2}$ in between them. (a) The phase space area and consequently the phase space emittance $\epsilon_{\mathrm{n},x}$ is conserved. (b) The trace space fans out depending on the kinetic energy, so the trace space emittance $\epsilon_{\mathrm{tr,n},x}$ is not conserved in the beam optical element. For beam parameters see text.

$\langle x' \rangle = 0$) this rewrites to

$$\epsilon_{\mathrm{n},x}(z) = \frac{1}{m_e c} \left[\langle x_0^2 \rangle \langle p_x^2 \rangle - \langle x_0 p_x \rangle^2 + m_e^2 c^2 \sigma_\gamma^2 \left(2z \langle x_0 x' \rangle \sigma_{x'}^2 + z^2 \sigma_{x'}^4 \right) \right]^{1/2} . \tag{4.7}$$

For sufficiently small energy spread or divergence, the z-dependent terms are negligible. The phase space emittance $\epsilon_{\mathrm{n},x}$ is then identical to the initial emittance, and is conserved in the drift.

The trace space emittance $\epsilon_{\mathrm{tr,n},x}$ is always conserved in a drift. This can be shown analogously by replacing x with $x_0 + z x'$ in eq. (4.3). However, this does not mean that the trace space emittance would be a better measure for the emittance. When the large energy spread beam enters a focusing element, the behaviour of the trace and the phase space emittances is opposite to in the drift: the phase space emittance is conserved and the trace space emittance grows. A beam optical element directly changes the transverse momentum p_x. The phase space emittance therefore is conserved. The change in transverse momentum however leads to an energy-dependent shearing in the trace space x-x'. The trace space emittance then grows for beams of large energy spread.

An example can be found in figure 4.2. After the drift of 0.1 m the bunch shown in fig. 4.1 is focused by a quadrupole of integrated field gradient $\partial B_y/\partial x \cdot l = 3.2\,\mathrm{T}$. The quadrupole is treated as a thin lens. The phase space emittance is conserved at $\epsilon_{\mathrm{n},x} = 5.7\,\mathrm{mm\,mrad}$, while the trace space emittance grows from initially $\epsilon_{\mathrm{tr,n},x} = 1\,\mathrm{mm\,mrad}$ also to 5.7 mm mrad. The chosen integrated field gradient collimates the beam in the sense that it minimizes the beam divergence. The trace space emittance therefore exactly matches the phase space emittance after the lens.

Emittance Growth in a Focusing Channel

For fig. 4.2 the focusing element was assumed to be short, and the thin lens approximation was used. In long lenses, i.e., focusing channels, this approximation breaks down and the effects of the focusing elements and the drift are combined.

The particle motion in a focusing channel is given by (see e.g. [82])

$$x'' = -Kx, \tag{4.8}$$

where K is the focusing strength. In the case of a plasma channel, it is given by the electromagnetic field gradient

$$K = \frac{e}{\gamma m_e c^2} \frac{\partial (E_r - cB_\theta)}{\partial r}. \tag{4.9}$$

For constant focusing strength the solution to eq. (4.8) can be found as

$$x = x_0 \cos \sqrt{K} z + \frac{x_0'}{\sqrt{K}} \sin \sqrt{K} z. \tag{4.10}$$

Judging from the oscillation frequency in this equation the length of a focusing element where the thin lens approximation is still valid can be approximated as $l \ll 1/\sqrt{K}$. The emittance evolution of a large energy spread beam in a focusing channel is illustrated in figure 4.3. The initial beam parameters are an emittance of $\epsilon_{\mathrm{n},x,\mathrm{ini}} = \epsilon_{\mathrm{tr,n},x,\mathrm{ini}} = 1\,\mathrm{mm\,mrad}$, with a beam size of $\sigma_x = 10\,\mu\mathrm{m}$, a divergence of $\sigma_{x'} = 0.5\,\mathrm{mrad}$, a mean energy of $\bar{E}_{\mathrm{kin}} = 100\,\mathrm{MeV}$ and a relative rms energy spread of $\sigma_E/\bar{E}_{\mathrm{kin}} = 10\,\%$. A focusing channel of $\partial(E_r - cB_\theta)/\partial r = 1 \cdot 10^{14}\,\mathrm{V/m^2}$ over a length of 5 mm is assumed. $10^{14}\,\mathrm{V/m^2}$ is the typical order of magnitude for the on-axis transverse derivative of the transverse fields in plasma wakefields. Using eq. (4.10) the particles are propagated through the channel. The initial particle distribution is shown in black, while the final distribution is color-coded according to the particles' energy like in figs. 4.1 and 4.2. The phase space and the trace space emittance both grow to 4.9 mm mrad and 4.5 mm mrad, respectively.

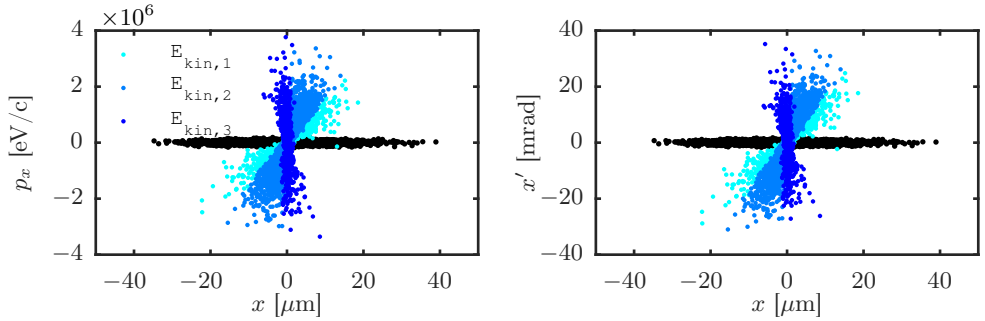

(a) Phase space.

(b) Trace space.

Figure 4.3 – Emittance evolution of a large energy spread beam in a focusing channel. Initial particle positions are shown in black, particle positions after the focusing channel are marked in shades of blue, where $E_{\mathrm{kin},1} < \bar{E}_{\mathrm{kin}} - \sigma_E$, $E_{\mathrm{kin},3} > \bar{E}_{\mathrm{kin}} + \sigma_E$, and $E_{\mathrm{kin},2}$ in between them. Both the phase space area (a) and the trace space area (b) fan out depending on the kinetic energy, the trace space and the phase space emittance are both not conserved. For beam parameters see text.

The reason for the emittance growth lies in the energy-dependence of the focusing strength, see eq. (4.9). The betatron frequency of the individual relativistic particles $\omega_\beta = c\sqrt{K}$ consequently depends on the energy γ. Slices of different energy rotate at a different frequency in phase space, leading to a decoherence in phase space. The same effect can also occur for bunches of finite length in a focusing channel where the focusing strength depends on the longitudinal coordinate, as it is the case in plasma wakefields [69].

4.2 Strategies to Mitigate Beam Quality Degradation

Emittance growth in drift spaces and in focusing channels has different origins. In the drift, the growth is caused by a large energy spread in combination with a large divergence. In a focusing channel, on the other hand, a large energy spread or a finite bunch length in combination with a longitudinally varying K can lead to the same result, namely betatron decoherence.

Typically, laser-plasma accelerated beams exit the plasma at a large divergence caused by the strong focusing forces in the wakefield. This is problematic not only as it leads to strong chromatic emittance growth after the target, but also as extremely strong

magnetic lenses are needed to capture the beam [81, 83]. The preferred method to prevent chromatic emittance growth in a drift would be to reduce the beam energy spread. This, however, is a non-trivial task in laser-plasma acceleration. The second option is to reduce the divergence. This suppresses emittance growth significantly, as the divergence enters eq. (4.7) with the fourth power in the radicand. Furthermore, this relaxes the requirements on the beam optics after the plasma target.

Emittance growth in a focusing channel can be omitted if the transverse beam size is matched to the focusing forces [84, 69]. The envelope of a matched beam does not oscillate in the focusing channel. This is equivalent to the area of the phase and trace space ellipses being constant – the particles still rotate in phase space, but the area they occupy is not changed. The matched beta function in a constant focusing channel is given by

$$\beta_m = \frac{1}{\sqrt{K}}, \tag{4.11}$$

and $\alpha_{\mathrm{CS}} = 0$ is required. The matched beam size follows as $\sigma_x = \sqrt{\epsilon_{\mathrm{n},x}\beta_m/(\beta\gamma)}$.

An example can be seen in figure 4.4. The same beam and focusing parameters as in fig. 4.3 are used, however, the beam size is now matched to the focusing forces with $\sigma_x = 2.3\,\mu\mathrm{m}$ and $\beta_m = 1\,\mathrm{mm}$. After a propagation distance of 5 mm the area covered by the particles is still the same, the emittance is conserved. The trajectory of one particle (white) lies within the ellipse already covered by the beam. In this example, the phase advance calculated from $\psi(z) = \int_0^z 1/\beta_m(z')\mathrm{d}z'$ amounts to 294°, which is also the angle described by the exemplary particle trajectory in Floquet coordinates (see section 2.5).

The strategy to maintain the beam quality throughout the plasma stage is consequently to inject the beam at the matched beam size and to reduce the beam divergence at the plasma exit. The matched beam size, however, is very small owing to the strong focusing forces in the plasma. For external injection this calls for strong focusing optics before the plasma, and also causes a large divergence after the plasma. A way to relax the requirements on the matched beam size for injection and to reduce the divergence after the target is to introduce dedicated matching sections at the entrance and the exit of the plasma target.

Adiabatic Tapering Profiles

Several authors have suggested to taper the plasma density at the exit in order to reduce the divergence [81, 83, 85, 71], and an ideal behaviour of the focusing strength K

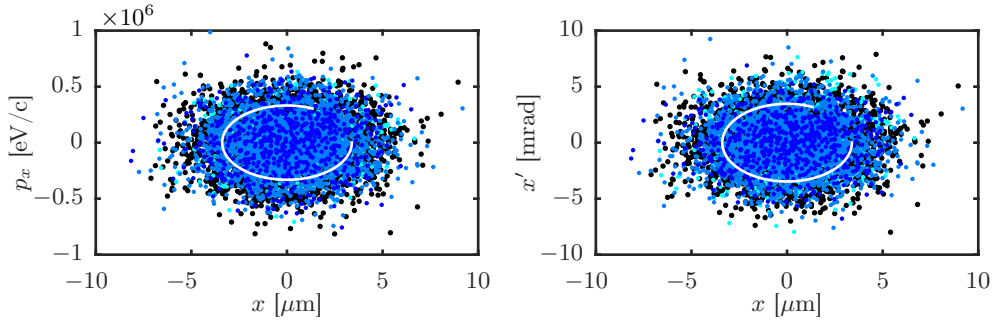

(a) Phase space.

(b) Trace space.

Figure 4.4 – Emittance evolution of a large energy spread beam with matched beam size in a focusing channel. Initial particle positions are shown in black, particle positions after the focusing channel are marked in shades of blue, where $E_{\mathrm{kin},1} < \bar{E}_{\mathrm{kin}} - \sigma_E$, $E_{\mathrm{kin},3} > \bar{E}_{\mathrm{kin}} + \sigma_E$, and $E_{\mathrm{kin},2}$ in between them. Both the phase space area (a) and the trace space area (b), and consequently also the trace space and the phase space emittance are conserved. The trajectory of one exemplary particle is plotted in white. For beam parameters see text.

has been proposed in [86]. Here, this analytical profile is translated into experimentally accessible parameters, the plasma density and the evolution of the laser envelope.

The aim of these tapering sections is to adiabatically expand (shrink) the beam size at the exit (entrance) of the plasma [86]. In the following, the case of the plasma exit is discussed, the concept, however, is general and can also be used for the plasma entrance. At the start of the tapering section, the beam size is matched to the focusing strength. In this context, adiabaticity means that the focusing strength changes slow enough so that the beam size can adapt to it without emittance growth. A measure for how fast the beam can adapt is the phase advance ψ. A large phase advance corresponds to the particles rotating quickly in phase space. The change of focusing strength therefore needs to be slow compared to the phase advance. Since in general $\psi(z) = \int_0^z 1/\beta_{\mathrm{CS}}(z')\mathrm{d}z'$ and considering eq. (4.11), a large focusing strength causes a large phase advance, which also means that changes of the focusing strength can be quick.

The proposed shortest still adiabatic profile for K is [86]

$$K(z) = \frac{K_0}{(1+gz)^4}, \tag{4.12}$$

where K_0 is the focusing strength at the start of the tapering section, i.e., at the end of the acceleration section. The taper parameter g determines how quickly the focusing strength decays, and needs to fulfill $g\beta_0 \ll 1$ to provide an adiabatic tapering. β_0 is the beta function at the start of the tapering section.

The focusing strength provided by a laser-driven linear wakefield depends on several physical parameters. From eqs. (4.9) and (2.11) it is found as

$$\begin{aligned} K &= \frac{e}{\gamma m_e c^2}\, \partial_r E_r|_{r=0} \\ &= -\frac{2a_0^2 k_p \sigma_{z,l}}{\gamma w_0^2}\sqrt{\frac{\pi}{2}}\, \exp\left(-\frac{k_p^2\sigma_{z,l}^2}{2}\right) \sin\left(k_p\zeta\right). \end{aligned} \tag{4.13}$$

Apart from the beam energy γ and the distance ζ between driver laser and witness bunch, the focusing strength also depends on the laser in terms of normalized laser vector potential a_0, the laser pulse length $\sigma_{z,l}$ and the laser spot size w_0. Furthermore, the plasma density plays a role, expressed by the plasma wave number k_p.

In the following, changes both of the kinetic energy and of the distance between driver and witness in the tapering section are neglected. The major part of the acceleration takes place before the extraction, while within the tapering section the focusing strength is reduced, which in most cases also implies a decreased accelerating field. The same is true for the distance to the driver laser. The length of the target is ultimately limited by the dephasing length, however, the tapering section only occupies a fraction of the total target length. Furthermore, even if some change in beam energy or slippage occurs, these processes change the focusing strength only very slowly, i.e., adiabatically.

There are two main knobs to turn in order to produce a profile similar to eq. (4.12): the evolution of the laser envelope and the plasma density. Both dependencies are considered separately here. Yet, in a real experiment it is very likely that the matching sections consist of a combination of both effects.
First, the plasma density and consequently the plasma wave number k_p is assumed to be constant. For a constant laser pulse length, the remaining dependency of the focusing strength is

$$K \propto \frac{a_0^2}{w_0^2} \propto \frac{1}{w_0^4}, \tag{4.14}$$

since a_0^2 is directly proportional to the laser intensity, $a_0^2 \propto I$, which scales inversely proportional to the spot size as $I \propto w_0^{-2}$. The ideal laser spot size evolution to fulfill eq. (4.12) is consequently

$$w(z) = w_0(1 + gz). \tag{4.15}$$

For an ideal Gaussian laser beam the beam size evolution in a free drift out of the focus is given by

$$w(z) = w_0 \sqrt{1 + \frac{z^2}{z_R^2}} \overset{z \gg z_R}{\approx} w_0 \frac{z}{z_R}. \tag{4.16}$$

Far away from the focus the qualitative behaviour of the beam size evolution resembles eq. (4.15). However, for the tapering factor $g \ll 1/\beta_0 \approx 1000$ is required, and the Rayleigh length z_R is typically around 1 mm. In most cases, the tapering provided by the freely diffracting laser will therefore be too fast, and guiding the laser pulse is necessary also in the matching section.

The other extreme case that one could consider is that the laser is guided at a constant spot size for example by a guiding channel, and, neglecting depletion, has the same intensity throughout the extraction section. The plasma density then is a free parameter and

$$K \propto \underbrace{k_p \exp\left(-\frac{k_p^2 \sigma_{z,l}^2}{2}\right)}_{\text{term 1}} \cdot \underbrace{(-\sin(k_p \zeta))}_{\text{term 2}}. \tag{4.17}$$

In order to obtain an ideal density profile this equation in combination with eq. (4.12) needs to be solved for the plasma wave number. Whether a continuous solution exists depends on the laser pulse length $\sigma_{z,l}$ (term 1) and on the distance between laser and bunch ζ (term 2). A decrease in density should always lead to a decrease of the focusing strength, as otherwise no continuous density profile can be found that mimics the ideal profile of K.
Term 1 is maximal for $\sigma_{z,l} = 1/k_p$, which is also known as the resonant pulse length [32]. A decrease of density and consequently of the plasma wave number will therefore only lead to a decrease of term 1 if $\sigma_{z,l} \leq 1/k_{p0}$. k_{p0} is the plasma wave number corresponding to the density at the start of the down ramp n_0.
The bunch phase is encoded in term 2. In a linear wakefield the maximum focusing strength in the first bucket is at $\zeta = -\lambda_p/4$, compare fig. 2.1 on page 15. This is called the dephasing point, as the longitudinal field exhibits a longitudinal zero-crossing there. If the bunch is at this position a decrease in density leads to a decrease of term 2. This would also be the case for $-\lambda_p/4 < \zeta < 0$, yet, such a constellation is unlikely as the longitudinal field is decelerating in this phase interval.
If both conditions are fulfilled, $\sigma_{z,l} \leq 1/k_{p0}$ and the bunch initially positioned at the dephasing point, the focusing strength decreases monotonically for decreasing plasma density and an ideal density profile can be found numerically. For resonant laser pulse length, $\sigma_{z,l} = 1/k_{p0}$, it is approximately given by

$$n(z) = n_0 \left[1 + c_1 g z + c_2 g^2 z^2\right]^{-2}, \tag{4.18}$$

with the fit parameters $c_1 = 3.45$ and $c_2 = 1.59$.

4.3 Matching Sections for External Injection

Apart from the divergence reduction at the plasma exit, in external injection experiments a matching section can help to relax the requirements on the matched beta function needed to inject the beam. Furthermore, tolerances to positioning jitters can be increased. This is illustrated with ASTRA[55] and FBPIC[87] simulations in the following.

An electron beam of kinetic energy $\bar{E}_{\mathrm{kin}} = 100\,\mathrm{MeV}$, relative rms energy spread $\sigma_E/\bar{E}_{\mathrm{kin}} = 0.1\,\%$, normalized transverse emittance $\epsilon_{\mathrm{n},x} = \epsilon_{\mathrm{n},y} = 1\,\mathrm{mm\,mrad}$ and rms bunch length $\sigma_z = 1\,\mu\mathrm{m}$ is focused into a plasma target and accelerated in a laser-driven wakefield. The bunch charge is chosen very low with $Q = 0.1\,\mathrm{pC}$, so that beam loading effects are negligible. The laser parameters are similar to state-of-the-art high-power laser systems with 1.5 J pulse energy, a pulse length of $\sigma_{z,l} = 13\,\mu\mathrm{m}$ (i.e., $\tau_{\mathrm{FWHM}} = 100\,\mathrm{fs}$) and $w_0 = 26\,\mu\mathrm{m}$ spot size. For an ideal Gaussian beam the Rayleigh length follows as $z_R = 2.7\,\mathrm{mm}$.

The plasma target consists of three sections. In the injection section the beam is slowly focused down into the acceleration section where most of the energy gain takes place. An extraction section at the end forms the transition into vacuum and adiabatically reduces the beam divergence and increases the beam size. Throughout the injection section, the laser beam size follows the ideal evolution of a Gaussian beam, see eq. (4.16), where the focus is at the start of the acceleration section. In the acceleration section it is guided by a plasma density channel. In the extraction section the plasma density channel for laser guiding is tailored to achieve a slow laser expansion according to eq. (4.15).

As this is the most simple assumption, the plasma density rises linearly from $n = 0$ at $z = 0$ to $n = 1 \cdot 10^{17}\,\mathrm{cm}^{-3}$ at $z = 2.7\,\mathrm{cm}$, the start of the acceleration section. The length of the injection section is chosen as $10\,z_R$ to make use of the slow increase of laser intensity. The acceleration section and the extraction section are 13 cm and 5 cm long, respectively, and the plasma density is constant there. This case is compared to the worst case of a flat top target of 13 cm length without any matching sections.

The x and y plane are identical in all simulations shown in the external injection case, therefore only the x plane is discussed.

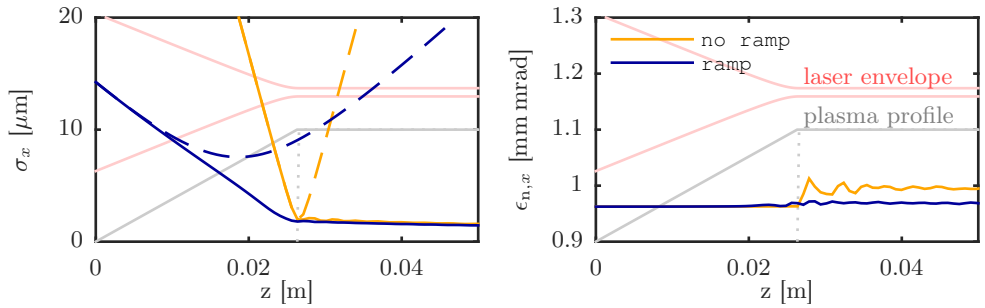

(a) Beam size.

(b) Beam emittance.

Figure 4.5 – Beam size (a) and emittance evolution (b) for externally injected beams simulated with Astra. The plasma profile and the laser envelope are indicated in faint gray and red. A case using a $10\,z_R$ long linear plasma up ramp (blue) is compared to a case without an up ramp (yellow). Both beams are matched and the emittance is conserved. The dashed lines in the plot (a) show the beam size evolution without a plasma target. The requirement on the beam size in the (virtual) focus is relaxed by the up ramp. For laser and beam parameters see text. The x and y plane are identical, therefore only x is shown.

4.3.1 Injecting the Beam

Astra simulations comparing the beam evolution in the injection section are shown in fig. 4.5. In both the case with the long linear up ramp (blue) and the case without any up ramp (yellow), the beam is matched at the start of the acceleration section at $z = 2.7\,\mathrm{cm}$ with $\sigma_x = 1.9\,\mu\mathrm{m}$ or $\beta_m = 0.8\,\mathrm{mm}$. For the sharp plasma start the emittance grows by around 3 %, which is likely caused by numerical inaccuracies at the steep edge. To good approximation the emittance is therefore conserved in both cases. The beam size in the case with a dedicated matching section, however, decreases much slower throughout the plasma up ramp. The relaxed requirements on the focal beam size are also illustrated by the dashed lines in the plot (a). They show the beam size evolution in vacuum, if no plasma target would be present. Without the matching section, this "virtual" focus of $\sigma_x = 1.9\,\mu\mathrm{m}$ coincides with the start of the plasma target and the laser focus. If an up ramp is present, the virtual focus lies within the up ramp and is much larger with $\sigma_x = 7.5\,\mu\mathrm{m}$ or $\beta_{\mathrm{CS}} = 12\,\mathrm{mm}$.

In order to find the beam parameters at the start of the injection section that ensure a

matched beam after the injection section the differential envelope equation is solved

$$\sigma_x'' + K(z)\sigma_x - \frac{\epsilon_x^2}{\sigma_x^3} = 0, \tag{4.19}$$

with the geometric emittance $\epsilon_x = \epsilon_{\mathrm{n},x}/(\beta\gamma)$. The matched beam size inside the nearly constant focusing channel present in the acceleration section is known, as is the behaviour of the focusing strength $K(z)$ in the injection section, assuming a linear wakefield, and the electron beam size σ_x can be propagated backwards through the injection section.

4.3.2 Jitter Tolerances

A dedicated injection section also helps to relax jitter tolerances. A beam entering a focusing channel at an offset or with an angle is subject to emittance growth just like a beam of unmatched spot size. The beam envelope of an unmatched beam oscillates at the betatron frequency, while an initial beam offset leads to the oscillation of the beam centroid at this frequency. Since the betatron frequency depends on the focusing strength, and the focusing strength in turn depends on the distance to the driver and on the bunch energy, both a large energy spread or a long beam lead to emittance growth from misalignments.

Betatron decoherence happens faster and therefore emittance growth is stronger for larger values of the focusing strength [69]. The parameter that determines the amount of beam quality degradation is consequently the misalignment at the laser focus. In the injection section the electron bunch is slowly focused into the accelerating section. In the same way, initial offsets are reduced in the injection section. Such a section makes the target more robust against positioning jitters.

For illustration, Astra simulations of beams injected with a random rms jitter of the beam offset of 10 % of the focal beam size, and an rms laser offset jitter of 5 % of w_0 (equivalent to 10 % of the rms laser spot size in focus) are shown in figure 4.6. The average beam emittance over 3000 independent runs grows by 20 % compared to the on-axis case for the target without a matching section. The injection section reduces this growth to about 2 %, even though the absolute jitter amplitude is slightly larger due to the larger focal beam size here. The beam trajectory for an initial offset of $y_{\mathrm{off}} = \left[(\sigma_x/10)^2 + (w_0/20)^2\right]^{1/2}$ can be seen in fig. 4.6(a). As expected, the offset is reduced during the matching section.

The average emittance growth in 3000 Astra runs caused by a pure angle jitter of laser and electron beam around their respective (virtual) focus positions can be seen

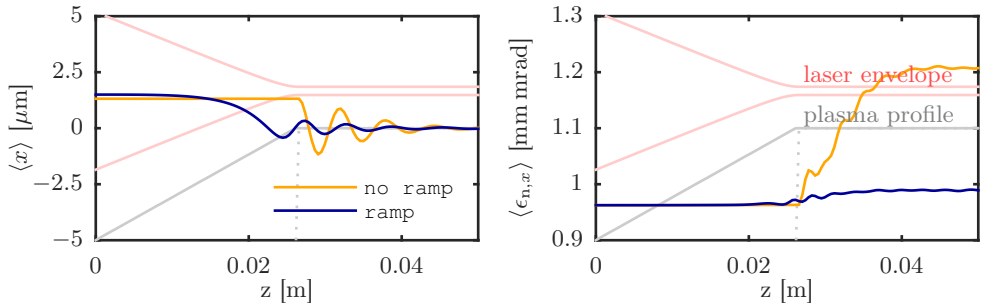

(a) Exemplary beam trajectory.

(b) Average beam emittance.

Figure 4.6 – Random rms jitter of the laser and beam offset. The beam offset jitters by $\sigma_x/10$ rms using σ_x in the (virtual) focus, that is $\sigma_x/10 = 0.8\,\mu$m or $0.2\,\mu$m with or without the injection section. The random rms laser offset jitters by $w_0/20$, i.e., by $1.3\,\mu$m. (a) Exemplary beam trajectory for an electron beam entering at an offset $y_{\text{off}} = \left[(\sigma_x/10)^2 + (w_0/20)^2\right]^{1/2}$. The injection section (blue case) reduces the oscillation amplitude at the laser focal position compared to the case without injection section (yellow). (b) Average emittance over 3000 ASTRA runs simulating the positioning jitter. The matching section increases the tolerance to positioning errors.

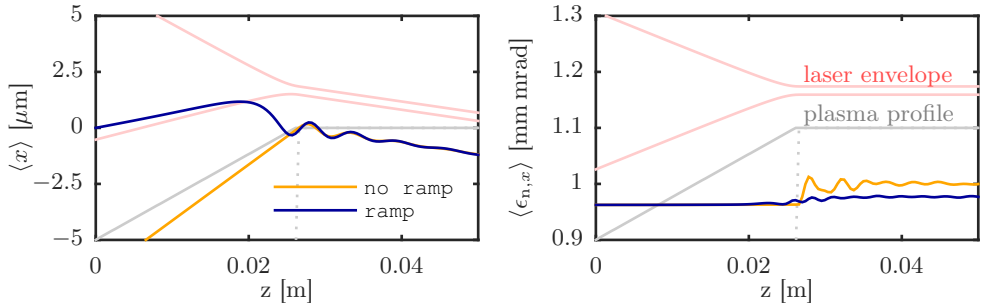

(a) Exemplary beam trajectory.

(b) Average beam emittance.

Figure 4.7 – Random rms jitter of the beam angle in focus by 10 % of $\sigma_{x'}$, that is $\sigma_{x'}/10 = 65\,\mu$rad or $250\,\mu$rad with or without the injection section, and random rms pointing jitter of the laser of $50\,\mu$rad. (a) Exemplary beam trajectory for an electron beam entering at 65 or $250\,\mu$rad into a plasma wakefield driven by a laser entering at an angle of $-50\,\mu$rad. (b) The average emittance over 3000 ASTRA runs is conserved for this parameter set in both cases.

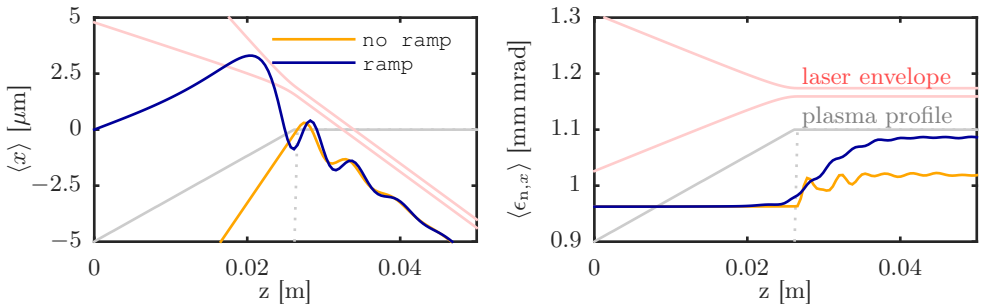

(a) Exemplary beam trajectory.

(b) Average beam emittance.

Figure 4.8 – Random rms jitter of the beam angle in focus by 20 % of $\sigma_{x'}$, that is 130 μrad or 500 μrad with or without the injection section, respectively, and random rms pointing jitter of the laser of 250 μrad. (a) Exemplary beam trajectory for an electron beam entering at 130 or 500 μrad into a plasma wakefield driven by a laser entering at an angle of −250 μrad. (b) The average emittance over 3000 Astra runs is not conserved for this parameter set.

in fig. 4.7. The rms angle jitter of the electron beam is 10 % of the beam divergence, that is $\sigma_{x'}/10 = 65\,\mu$rad or 250 μrad with or without the matching section, and the pointing jitter of the laser is 50 μrad rms. As can be seen in fig. 4.7(b) both setups are tolerant to angle jitters and the influence is negligible for the chosen parameter set.

The susceptibility of both setups becomes clear only for large angle jitters. In figure 4.8 the average emittance growth in again 3000 Astra runs and exemplary trajectories can be seen, with an rms angle jitter of the electron beam of 20 % of the beam divergence, that is $\sigma_{x'}/5 = 130\,\mu$rad or 500 μrad with or without the matching section. The pointing jitter of the laser is assumed to be five times larger than previously with 250 μrad. The average emittance growth amounts to 12 % with the matching section but only to 2.4 % with the sharp plasma edge.

In conclusion, the dedicated injection section increases the tolerances to positioning jitters at the plasma entrance. Pure angle jitters of electron beam and laser in their respective focal positions lead only to small beam quality degradation both with or without the injection section. For very large angle jitters, the dedicated injection section performs worse than the sharp plasma edge. In an experiment, the length of the injection section could be used to balance the influence of positioning and angle jitters, depending on the actual stability of both laser and electron beam.

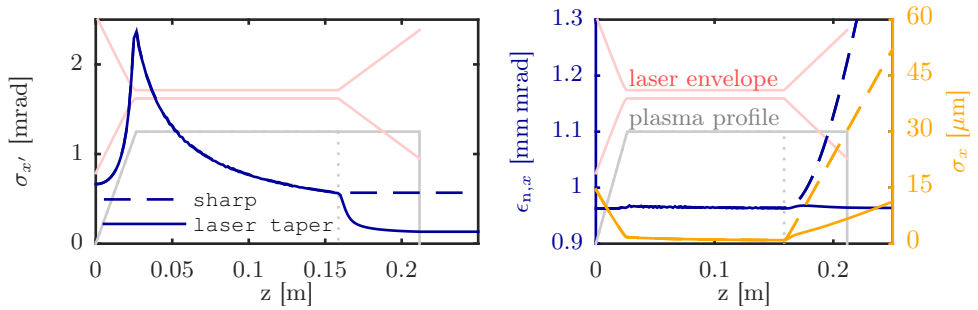

(a) Beam divergence.

(b) Beam emittance.

Figure 4.9 – (a) Beam divergence and (b) emittance and beam size evolution for externally injected beams simulated with ASTRA. The plasma profile and laser envelope are indicated in faint gray and red. The case with a sharp plasma end (dashed lines) at $z = 15.9\,\mathrm{cm}$ is compared to a case with constant density extraction section (solid lines), where the laser is tapered according to eq. (4.15). The divergence rises quickly during the $10\,z_R$ long linear plasma up ramp and is damped due to energy gain during the acceleration section. The dedicated extraction section reduces the divergence by a factor of 4 and causes a slow increase of the beam size, and thereby significantly suppresses chromatic emittance growth in the drift after the target. For laser and beam parameters see text.

Accelerating the Beam

After the beam has been injected, it is accelerated in a constant density section where the laser is guided by a density channel at constant spot size $w = w_0$. This section is terminated once the beam has reached 1 GeV at $z = 15.9\,\mathrm{cm}$.

4.3.3 Extracting the Beam

For the extraction section, the focusing forces are tapered according to the ideal profile, realized by tailoring the laser beam size evolution like in eq. (4.15). Typically, the taper factor g calls for a slower increase of the laser spot size than caused by the undisturbed Gaussian beam evolution. The evolution of the laser spot size $w(z)$ then needs to be enforced by a plasma density channel. Experimentally, laser guiding can be achieved in a capillary discharge target. The gas pressure applied before the discharge and the capillary diameter determine the guided laser spot size and the on-axis plasma density

after the discharge [31]. A slow taper of the laser spot size can be achieved by properly designing the target geometry.

ASTRA does not self-consistently track the laser propagation through the plasma. Instead, $w(z)$ is defined analytically beforehand. Therefore, a PIC simulation is shown for comparison later in section 4.3.4. This includes, in addition to other effects like wakefield nonlinearities, which are absent in ASTRA, the self-consistent modeling of the laser propagation through the guiding channel.
Figure 4.9 shows ASTRA simulations of the complete 1 GeV plasma stage. The case including a dedicated extraction section (solid lines) of 5.3 cm, or $20\,z_R$, length and $g = 137\,\mathrm{m}^{-1}$ is compared to a simulation with a sharp plasma end directly after the acceleration section (dashed lines). The length of the extraction section is chosen much longer than the Rayleigh length to achieve a slower extraction than possible just by letting the laser diffract. On the other hand, it should be significantly shorter than the acceleration section length of 13 cm to keep the setup still compact. The chosen taper parameter g fulfills the required $g\beta_0 \ll 1$ with $g\beta_0 = 0.2$.
The beam divergence rises during the injection section and is damped during the acceleration section as the beam gains kinetic energy. Compared to the divergence of $\sigma_{x'} = 0.56\,\mathrm{mrad}$ of the beam at the sharp edge, the dedicated extraction section reduces the divergence by more than a factor of four to $\sigma_{x'} = 0.13\,\mathrm{mrad}$.

During the acceleration section the beam has accumulated a mainly correlated relative rms energy spread of $\sigma_E/\bar{E}_{\mathrm{kin}} = 2.4\,\%$. In combination with a large divergence, this leads to chromatic emittance growth in the drift after the target according to eq. (4.7). Without the extraction section, the transverse emittance grows by 275 % from $\epsilon_{\mathrm{n},x} = 0.96\,\mathrm{mm\,mrad}$ to $\epsilon_{\mathrm{n},x} = 3.6\,\mathrm{mm\,mrad}$ during a 25 cm long drift behind the target end and keeps growing. With the matching section it increases by only 2 % to $\epsilon_{\mathrm{n},x} = 0.98\,\mathrm{mm\,mrad}$ at 25 cm behind the target end.

4.3.4 Validation of the Linear Model with PIC Simulations

Since ASTRA makes several assumptions on the plasma interaction, such as not self-consistently modeling the laser propagation through the target, or using the linear wakefield approximation (eqs. (2.10)-(2.12)), Particle-In-Cell simulations are needed to validate the results. The long target assumed here with around 20 cm length makes PIC simulations computationally very intensive, as millions of time steps are needed to propagate the simulation volume through the plasma target. The reason for this is that the maximum time step length is limited by the **C**ourant-**F**riedrichs-**L**ewy (CFL) condition [88] that is given by the spatial resolution of the simulation grid. It is however possible to perform the simulation not in the laboratory frame, but to transform the

physical setup to a Lorentz-boosted frame where the scales are more favorable [56]. In the boosted frame the plasma is contracted and propagates towards the elongated laser pulse. As the needed spatial resolution is determined by the laser wavelength, also the time step length increases. This allows for far fewer time steps to be simulated.

However, simulations in the boosted frame are prone to the **N**umerical **C**herenkov **I**nstability (NCI) [89–92]. This is a violent instability stemming from the relativistic movement of the plasma with respect to the simulation grid, as the charged particles excite an electromagnetic (beam) mode at their speed, which is close to the speed of light. This mode can couple to an incorrectly modeled dispersion relation, as can be the case for finite difference time domain solvers, where Maxwell's equations are solved using spatial finite differences to approximate the derivatives. In addition, the spatial aliases of the beam mode can also couple to a correctly modeled dispersion relation, leading to a fast growing NCI. Many methods have been proposed to suppress NCI, for example to filter the simulated fields [93–96] or to artificially modify the dispersion relation [97–99].

The simulations shown in the following are performed with FBPIC [87], a quasi-cylindrical spectral code that runs on GPUs [100]. The usage of a quasi-cylindrical geometry [101] where the electromagnetic field components are azimuthally Fourier expanded to also include 3D effects like laser polarization, drastically reduces the memory requirements and run time. In addition, the spectral solver is free of spurious numerical dispersion, in contrast to finite difference time domain solvers. FBPIC features a novel method that makes it intrinsically free of NCI by solving Maxwell's equations in a Galilean transformed coordinate system [102, 103]. In this frame, the simulation grid moves with the relativistic plasma particles and this assumption is also included in the solver for Maxwell's equations. The relativistic plasma can therefore be modeled in the Lorentz-boosted frame without any additional filtering. The GPU implementation, the quasi-cylindrical geometry, and the boosted frame enabled by the NCI-free code cause a drastic speed-up, so that the PIC simulation of this setup with more than 20 cm plasma interaction is possible on a single Nvidia Tesla K80 type GPU in less than ten hours.

The simulation volume consists of 4500×200 cells covering a longitudinal length of $120\,\mu$m and a radial width of $300\,\mu$m. In each cell $2 \times 2 \times 4$ macro particles are distributed in longitudinal, radial and azimuthal direction. The simulation is boosted with $\gamma_{\text{boost}} = 15$. The plasma density channel width is tailored in the PIC simulation to achieve a laser spot size evolution like defined analytically in Astra. In the injection section, no guiding channel is present, while in the acceleration section a constant guiding channel matched to a laser spot size of $w_0 = 26\,\mu$m is present. 5.6 mm before the end of the acceleration section, the guided spot size starts to increase slowly to

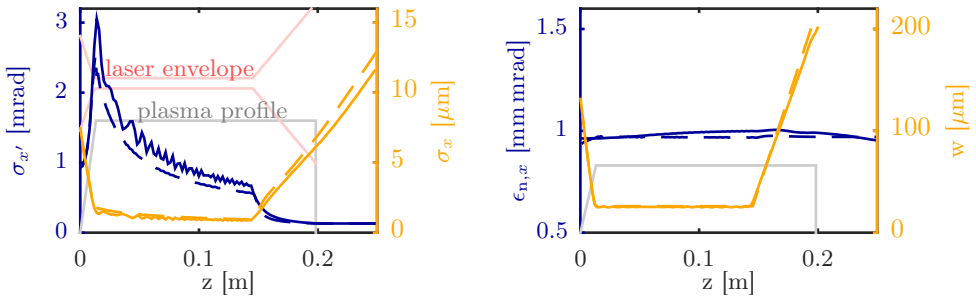

(a) Divergence and beam size.

(b) Beam emittance and laser spot size.

Figure 4.10 – Comparison of the PIC simulation (solid lines) to Astra (dashed). The laser spot size evolution is ensured with a tailored plasma density channel.

allow the laser to follow, and then increases according to eq. (4.15) in the extraction section. The density channel for a matched spot size w_0 is given by (see [32] and references therein)

$$n = n_0 \left(1 + \frac{\Delta n}{n_0} \frac{r^2}{w_0^2}\right), \tag{4.20}$$

$$\text{with } \Delta n = \frac{1.13 \cdot 10^{20}}{(w_0[\mu\text{m}])^2} \,\text{cm}^{-3}, \tag{4.21}$$

where n_0 is the on-axis density.

For this comparison, the injection section is shortened to $5\,z_R$, opposed to $10\,z_R$ in the previous paragraphs. This reduces the laser spot size at initialization, and allows to reduce the transverse width of the simulation window and consequently the memory consumption.

Figure 4.10 shows the comparison of the Particle-In-Cell simulation (solid lines) with the Astra simulation (dashed). Especially the electron beam size agrees very well, while only small deviations are visible in the divergence and emittance evolution. The origin of these deviations might well be from physical differences, as FBPIC intrinsically includes effects like for example wakefield nonlinearities. The oscillations visible in the divergence can then stem from a slightly different matched beam size in the PIC simulation, while the bunch has been optimized for the Astra fields. The deviation is, however, not large enough to cause significant emittance growth. The divergence after the extraction section agrees with sub-percent level accuracy between

the two codes.
The longitudinal beam properties, the mean kinetic energy $\bar{E}_{\text{kin}}$ and the relative rms energy spread $\sigma_E/\bar{E}_{\text{kin}}$ (not shown), agree within ten percent, with $\bar{E}_{\text{kin}} = 0.88\,\text{GeV}$ and $\sigma_E/\bar{E}_{\text{kin}} = 2.6\,\%$ in FBPIC, and $\bar{E}_{\text{kin}} = 0.98\,\text{GeV}$ and $\sigma_E/\bar{E}_{\text{kin}} = 2.4\,\%$ in ASTRA.

4.4 Matching Sections for Internal Injection

An adiabatic tapering section can also be employed to extract an electron bunch generated from internal injection in a plasma acceleration stage. This will be shown in the following section at the example of a bunch injected via shock-front injection.

All simulations are performed with the same code also used in the previous section, FBPIC [87], a spectral, quasi-cylindrical PIC code running on GPUs. The general setup is described first, followed by a comparison of a laser and a density tapered extraction section.

4.4.1 Setup and injected phase space

For the example shown here, parameters similar to those at the LUX experiment in Hamburg with the ANGUS laser system are used. A summary of laser, plasma and bunch parameters can be found in table 4.1. The plasma target is structured into four sections: an initial high density plateau at density $n_0 = 1 \cdot 10^{18}\,\text{cm}^{-3}$, a density down ramp of length $l_{\text{ramp}} = 200\,\mu\text{m}$ to trigger injection, a lower density plateau at density $n_{\text{acc}} = 7 \cdot 10^{17}\,\text{cm}^{-3}$ to allow for acceleration of the bunch, and the extraction section. The laser of vacuum focal spot size $w_0 = 18\,\mu\text{m}$, 25 fs FWHM pulse length and normalized peak vector potential $a_0 = 4.0$ is focused at the end of a density down ramp. The plasma profile (blue) as well as the vacuum laser spot size evolution (dashed yellow) can be seen in figure 4.11(a). In the plasma, especially in the high density region, the laser undergoes self-focusing [32] (solid yellow line, from an FBPIC simulation). This can originate from two effects. First, due to its ponderomotive force, the laser pushes aside plasma electrons and basically creates its own plasma guiding channel. Second, the relativistic Lorentz factor γ of plasma electrons increases near the on axis peak intensity of the laser, which also leads to a change of refractive index that depends on the transverse coordinate and focuses the laser pulse.
To ensure a smooth transition from the high to the low density plateau, the density

ANGUS driver laser (Gaussian)			
spot size w_0		$18\,\mu$m	
pulse length (FWHM)		25 fs	
normalized vector potential a_0		4.0	
wavelength λ_l		800 nm	
polarization direction		x	
plasma profile			
initial density n_0		$1 \cdot 10^{18}\,\mathrm{cm}^{-3}$	
down ramp length l_{ramp}		0.2 mm	
plateau density n_{acc}		$7 \cdot 10^{17}\,\mathrm{cm}^{-3}$	
plateau length		1.2 mm	
injected bunch (end of density plateau)			
mean kinetic energy $\bar{E}_{\mathrm{kin}}$		145 MeV	
rms energy spread $\sigma_E/\bar{E}_{\mathrm{kin}}$		7.7 %	
bunch charge Q		400 pC	
rms bunch length σ_z		$2.6\,\mu$m	
rms beam size σ_x	$1.9\,\mu$m	σ_y	$0.59\,\mu$m
transverse emittance $\epsilon_{\mathrm{n},x}$	4.4 mm mrad	$\epsilon_{\mathrm{n},y}$	0.55 mm mrad
divergence $\sigma_{x'}$	8.0 mrad	$\sigma_{y'}$	3.2 mrad

Table 4.1 – Parameters in the internal injection case triggered by shock-front injection.

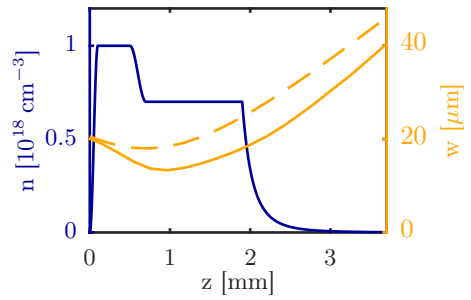

(a) Plasma profile and laser spot size evolution.

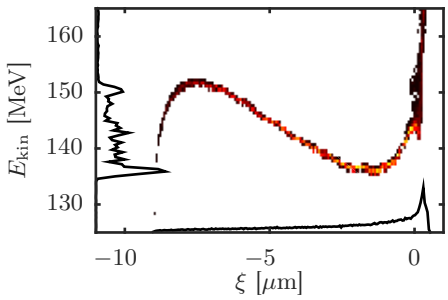

(b) Longitudinal phase space.

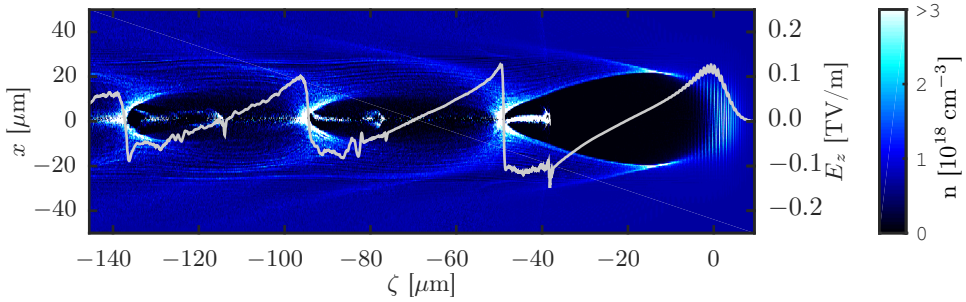

(c) Electron density and accelerating field.

Figure 4.11 – Overview of the internal injection setup. (a) Plasma profile (blue) and laser envelope in vacuum (dashed yellow) and in plasma (solid yellow) from an FBPIC simulation. The steep, shock-front like density down ramp triggers injection. Here, an extraction section using tapered density is shown as an example. Different extraction sections will be used later. (b) Longitudinal phase space at the end of the plasma density plateau at $z = 1.9\,\mathrm{mm}$. The S-shape is caused by beam loading. (c) Electron density in the wakefield (colors) including the injected bunch and longitudinal field line out (gray) directly after injection, at $z = 0.8\,\mathrm{mm}$. Beam loading causes a flattened longitudinal field in the first bucket.

down ramp for injection follows a squared sine function like

$$n = n_0 - (n_0 - n_{\mathrm{acc}}) \cdot \sin^2\left(\frac{\pi(z - z_{\mathrm{ramp}})}{2l_{\mathrm{ramp}}}\right), \tag{4.22}$$

where $z_{\mathrm{ramp}} = 0.5\,\mathrm{mm}$ is the z position at which the density ramp starts.

In figure 4.11(c) the electron density of the plasma wakefield at the end of the density down ramp at $z = 0.7\,\mathrm{mm}$ can be seen, as well as an on-axis line out of the longitudinal electric field. In the first bucket around $\zeta = -45\,\mu\mathrm{m}$, an electron bunch is injected, which contains sufficient charge to flatten the longitudinal field. Injection is also visible in the second and third bucket. However, in the density down ramp, the change of phase of the injected particles due to the change in density depends on the position in the wake. Consider a density change that corresponds to a doubling of the plasma period. An electron bunch initially positioned at $\zeta = -\lambda_p$, which is a phase of $\Psi = -2\pi$, will be shifted to $\Psi = -\pi$ during the density decrease. In contrast, if it is initially at $\zeta = -2\lambda_p$, i.e., at $\Psi = -4\pi$, it will be shifted by a larger phase difference to $\Psi = -2\pi$. Therefore, a large part of the charge injected into the second and third bucket is already at or near the dephasing point, i.e., at the zero-crossing of the longitudinal field, after the down ramp. The acceleration of electrons injected into the second and higher buckets is consequently not efficient, and the final energy of these particles will be very different from the energy of the bunch in the first bucket.

Typically, these short, steep down ramps are produced by inserting a razor blade into a gas jet [104]. A supersonic shock then causes the steep ramp. This injection mechanism is therefore often referred to as shock-front injection, opposed to the original concept of density down ramp injection [12], where longer ramps are used.

In contrast to externally injected bunches, here it is necessary to define criteria on how to identify the bunch from the phase space of all plasma electrons. The main criterion can be the kinetic energy, which is also an experimentally accessible parameter. First, all plasma electrons with a Lorentz factor $\gamma \leq 100$ are removed to include only injected charge and exclude the plasma wakefield background. From the remaining electrons both the current profile and the energy spectrum are calculated. The second cut in the energy includes only those particles within 30 % of the average Lorentz factor γ. Especially in the case of a laser tapered extraction, which will be shown later, the bunch is decelerated in the extraction section, while the electrons injected in the later buckets gain energy. The particles from later buckets are then not filtered by the energy cut, and impact mainly the numerical emittance calculation. Although this would be very difficult experimentally, to exclude them for the analysis here another cut is applied in the longitudinal coordinate. It allows only those particles within

$\pm 9\,\mu$m of the peak current position, which is at the head of the bunch in the first bucket.

The acceleration section ends at $z = 1.9\,$mm. The longitudinal phase space of the bunch at this position is shown in figure 4.11(b). Apparently, the flattening of the longitudinal field due to beam loading is not perfect, and the phase space exhibits an S-shape like structure. During the acceleration section, the tail has gained more energy than the head. It might be possible to further optimize the shape of the longitudinal phase space, for example by earlier termination of the acceleration section at the cost of beam energy, or by choosing a different density n_{acc}. This, however, is not the purpose of this chapter.
In some parts of the bunch the slice energy spread is significantly lower than the projected energy spread. For $-8\,\mu\mathrm{m} < \xi < -4\,\mu\mathrm{m}$ the relative rms slice energy spread is around 0.2 %. However, in the bunch head for $\xi \geq -2\,\mu$m, where also the largest current is located, the slice energy spread is still large with 6 to 8 %. The charge contained in the bunch amounts to 400 pC, with a peak current of around 60 kA. This is an extremely high charge, even for an internally injected bunch. Please note that in the tail of the bunch with $\xi < -4\,\mu$m the current is still between 5 and 10 kA at low slice energy spread.
As expected, the beam size is very small, and the divergence is large, see table 4.1. Also, the normalized emittance in the x direction, which is the laser polarization direction, is significantly larger than in the y direction.

To exclude possible errors from the quasi-cylindrical geometry assumed in FBPIC the injection is also simulated with the full 3D PIC code Warp [39]. The simulation volume of $105\,\mu\mathrm{m} \times 120\,\mu\mathrm{m} \times 120\,\mu$m is divided into $4200 \times 251 \times 251$ cells with four particles per cell. The injected phase space (not shown) is very similar in Warp as in FBPIC, and has the same peak current and current profile. Also the slice energy spread is similarly small in the bunch tail and large in the current spike at the bunch head. The most significant deviation is in the emittance, which is only $\epsilon_{\mathrm{n},x} = 1.6\,$mm mrad in Warp, while it is 4.4 mm mrad in FBPIC. Due to the much shorter run time of FBPIC of only 6.5 hours on a single Nvidia Tesla K80 GPU per millimeter propagation length, compared to 30720 CPU-hours per millimeter propagation length in Warp, the extraction studies are continued with FBPIC.

4.4.2 Design and PIC simulations of the extraction section

Compared to the previously discussed external injection case, mainly two things are very different in the internal injection case and therefore affect the design of the extraction section. First, the laser is not guided by a plasma density channel, and second,

the bunch charge is much higher. The laser will consequently diffract freely, except for the small amount of self focusing still present in the low density plateau. Due to its high charge the electron bunch causes significant beam loading, so that it might not react to the weaker laser-driven wake once the laser diffracts, but remain focused in its own wakefield. Due to both effects, the option of tapering the evolution of the laser envelope is not very promising. The most similar case to a laser tapered extraction section would be to keep the plasma density constant until the laser has diffracted to a negligible intensity.
The other option is to taper the plasma density. In this case, one can account also for the strong beam loading by tapering the density for the beam-driven wakefield. With a peak density of $1 \cdot 10^{21}\,\mathrm{cm}^{-3}$ the bunch is much more dense than the ambient plasma. Its wakefield is therefore in the blow-out regime, where the simplest approximation is a spherical cavity devoid of electrons [32]. This causes a focusing strength dependency on the plasma wave number like

$$K \propto k_p^2. \tag{4.23}$$

The focusing strength is independent of the longitudinal coordinate inside the bubble. As $n \propto k_p^2$, a comparison of this expression to the ideal focusing strength profile from eq. (4.12), $K(z) = K_0/(1+gz)^4$, directly gives the ideal density profile

$$n(z) = \frac{n_{\mathrm{acc}}}{(1+gz)^4}, \tag{4.24}$$

where in this equation the start of the extraction section would be at $z = 0$.

Both options, keeping the density constant or tapering it according to eq. (4.24), are simulated with FBPIC. Figure 4.12 shows the bunch evolution in the extraction section. The yellow lines correspond to the case of constant plasma density, where the extraction section relies on the tapering effect from the laser diffraction. The blue lines show the bunch evolution in the case of a density tapering according to eq. (4.24) with $g = 2 \cdot 10^3\,\mathrm{m}^{-1}$, starting at $z = 1.9\,\mathrm{mm}$. The criterion of $g\beta_0 \ll 1$ is fulfilled with the beta function at the start of the extraction section being around $\beta_0 = 0.2\,\mathrm{mm}$ in both planes.

In the case of a density down ramp the emittance and the bunch charge are conserved. Furthermore, the kinetic energy is almost unchanged through the extraction section. A slight deceleration is visible and can be expected, as the decrease in density shifts the bunch to the decelerating phase region behind the driver. Also, a very small emittance decrease occurs in the down ramp, which might originate from a reorientation of the halo visible in fig. 4.12(f) with respect to the main bunch, similar to the effect found in [105], or from particle loss.
An emittance decrease is possible if correlated phase space ellipse orientations in the

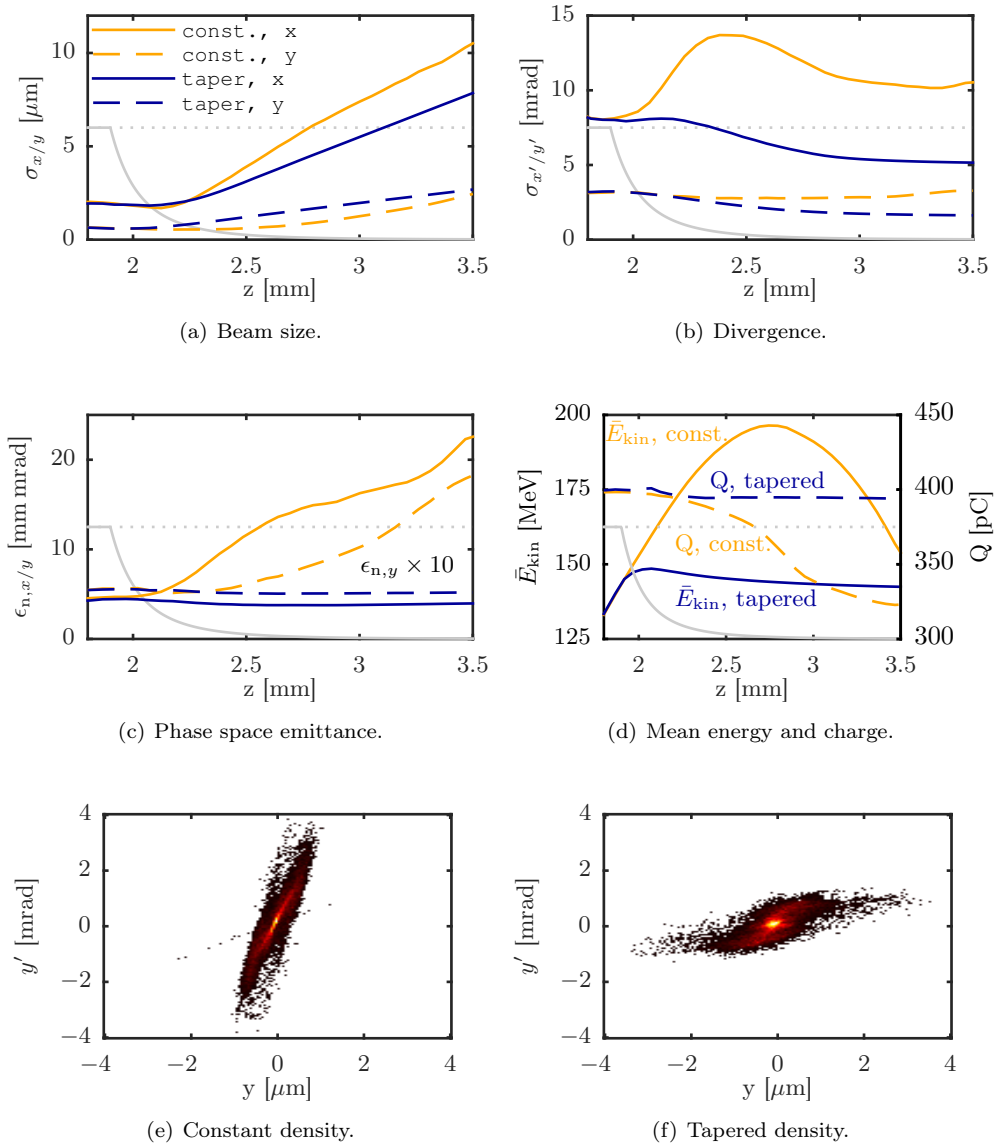

(a) Beam size.

(b) Divergence.

(c) Phase space emittance.

(d) Mean energy and charge.

(e) Constant density.

(f) Tapered density.

Figure 4.12 – Bunch evolution in the extraction section for either a constant density (yellow lines) or a density taper (blue lines). In (a)-(c) the solid lines represent the x plane of the bunch, while the dashed lines show the y plane. In (d) the solid lines correspond to $\bar{E}_{\mathrm{kin}}$ and the dashed lines show the charge contained in the bunch. Note that in (c) $\epsilon_{n,y}$ is multiplied by a factor of 10. (e) and (f) show the trace space in y at $z = 3.7\,\mathrm{mm}$.

bunch exist and can be reduced. For example, due to different energies or focusing strengths the phase space ellipse of the head of the bunch could be in a different phase of the betatron oscillation than the one at the tail. Decreasing the density changes the focusing forces differently in the two regions, they can realign and the projected beam emittance is reduced. In Ref. [105] the adiabatic extraction of an externally injected beam under the influence of beam loading has been studied, and an emittance compensation effect at the head of the bunch originating from beam loading has been found.
A decrease in emittance can also be caused by particle loss, as typically those particles are lost that travel trajectories far from the bunch center. Since these also contribute strongly to the emittance, their loss reduces the emittance. The emittance decrease observed here can be caused by particle loss, as also a small decrease in bunch charge is visible around $z = 2.1\,\mathrm{mm}$. However, it is in any case a very small effect here.
As before, the decreasing focusing strength in the down ramp in combination with the conserved emittance leads to a decrease in beam divergence to $\sigma_{x'} = 5.1\,\mathrm{mrad}$ and $\sigma_{y'} = 1.6\,\mathrm{mrad}$ at $z = 3.7\,\mathrm{mm}$.

In the case of a constant density, relying on the laser diffraction leads to strong emittance growth in both planes. The divergence is not reduced or even increases in the x plane, and a significant charge loss can be observed. The kinetic energy first continues to rise, but starts to fall again at roughly the same z position where the charge loss occurs. This can be identified as the transition from the laser-driven wake to the beam-driven wake. Due to the lower laser intensity the laser-driven bubble contracts (not shown in the figure) and the tail of the bunch is shifted to the defocusing region, i.e., into the density peak at the back of the bubble. The formation of the beam-driven bubble is not quick enough to prevent the tail of the bunch from leaving the wake due to the strong defocusing forces. Once the beam-driven wake dominates the bunch decelerates in its own wake.
The strong emittance growth can then be attributed to the quickly changing focusing strength at the transition from the laser- to the beam-driven wake. A decoherence of the longitudinal slices in the bunch can also be expected, as typically a beam-driven wake changes significantly over the driver bunch length. In fig. 4.12(e) the trace space in y is shown. In contrast to the plasma density tapered case, fig. 4.12(f), the trace space exhibits a larger divergence. Furthermore, remaining particles from the tail form a thin line at a different angle than the main bunch.

Conclusion

A large beam current is characteristic for internally injected electron bunches. In this case, the pure laser tapering is not a good option as the beam will stay focused due to

its high charge density even once the laser has diffracted. The divergence then cannot be reduced. In the example shown here, also additional emittance growth occurs once the laser has diffracted and the beam-driven wakefield dominates.
For the extraction of a high charge beam from the plasma consequently a plasma density down ramp is the only option. It has been demonstrated with PIC simulations that the density down ramp conserves the emittance while reducing the divergence by a factor of 1.6 to 2 for the specific example discussed.
However, with a relative rms energy spread around 8 % even the reduced divergence will lead to strong chromatic emittance growth in the drift following the plasma. Furthermore, the divergence is still large with 5.1 and 1.6 mrad in x and y, respectively. The matching section therefore is only part of the solution. In addition, strong focusing optics shortly behind the plasma are needed to capture the beam. This could be quadrupole magnets, an additional laser-plasma lens [75], or a discharge-capillary active plasma lens [73]. Since the laser-plasma lens relies on the remaining laser power, it might not be suited for the example discussed here, where the laser diffracts quickly and the bunch charge is very high. The working principle of the discharge-capillary plasma lens is different. It makes use of the high current density present in a capillary discharge, and the induced magnetic field provides strong symmetric focusing. The discharge, however, is also pulsed through a (low density) plasma, and beam loading might still be an issue for high charge beams. How to best combine the extraction optics – matching sections, current or laser-driven plasma lenses, or even passive plasma lenses [79] – therefore depends significantly on the specific example considered. Similarly, for very short matching distances like between two LPA stages without any beam optics [106, 107], a non-adiabatic matching can also conserve the emittance.

4.5 Summary

The previous chapter was concerned with the beam quality conservation throughout the plasma stage, as well as with the divergence reduction at the plasma vacuum interface.
In order to avoid emittance growth in the strong focusing fields of the laser-driven plasma wakefield, the beta function of the injected bunch has to be matched to the focusing forces. The required very small beta function is extremely challenging for the capturing beam optics after the plasma, and in the case of external injection also for the injection beam optics. Furthermore, the large divergence in combination with a typically large energy spread leads to chromatic emittance growth in a drift.
In order to relax tolerances on the beam optics and to mitigate emittance growth in the drifts, adiabatic matching sections at the plasma to vacuum transition and, for

external injection, also at the vacuum to plasma transition have been used. In these sections the focusing strength of the wakefield changes slowly to allow the bunch to adapt to it and adiabatically increase or decrease its beta function.

Two different ways to design the matching sections have been investigated: tailoring the plasma density or shaping the laser spot size evolution.
In the case of an electron bunch with low charge density in a hybrid acceleration scheme, it has been shown with ASTRA and with Particle-In-Cell simulations that the tapering of the laser beam size evolution can reduce the divergence by more than a factor of four for the example considered. The beta function needed for injection could be increased from 0.8 mm without a matching section to 12 mm with a non-optimized matching section, only making use of the Gaussian laser evolution and a linear plasma density ramp. This also significantly increases the tolerances to laser and bunch positioning jitters at injection.
Tapering the laser beam size evolution provides the advantage that it is independent of the phase of the bunch in the linear wakefield. It is well suited for the low-charge bunches in linear or quasi-linear wakefields typical for hybrid accelerators.
However, the charge density of internally injected bunches can be much higher. In this case, it has been found at the example of PIC simulations of a shock-front injected electron bunch that the plasma density tapering is the favorable option. If only laser tapering is employed, a transition from laser-driven to beam-driven wakefield occurs, leading to strong emittance growth and preventing a divergence reduction. On the other hand, tailoring the density according to the derived ideal profile conserves the beam emittance and reduces the divergence.

5 Modulated Plasma Density for Wakefield Shaping

One of the major challenges in plasma acceleration is that the produced electron beams typically exhibit a large relative rms energy spread of several percent. The energy spread is a crucial parameter for any light source design. In the case of undulator radiation it broadens the spectrum and thereby reduces the brilliance. More critically, for a Free-Electron Laser to show gain, the relative energy spread has to be smaller than the so-called FEL parameter, which is in the range of 10^{-4} to 10^{-2}.

From the ratio of the electron bunch length to the plasma wavelength, and from the overlap of focusing and accelerating region in the wake, it can be expected that a large part of the measured projected energy spread is actually correlated with the longitudinal bunch coordinate. To circumvent this, already in 1987 it has been proposed [108] to shape the current profile of the accelerated bunch, the so-called witness bunch, such that the wakefield driven by the bunch flattens the laser-driven wake. This ideally requires a triangular current profile. An idea from the late 1990s [109] features a hollow plasma channel, which effectively removes the focusing forces of the wakefield and allows for acceleration at the minimum of the longitudinal fields. Both concepts have not been demonstrated so far. Another approach is to accept the energy spread delivered by the source and filter for the design energy in a subsequent dispersive beam optics, as proposed in [110] for a LPA driven source for ultrafast electron diffraction. This, however, comes at the cost of significant charge loss, which is a severe disadvantage for FELs.

This chapter is concerned with a new concept to reduce the energy spread by modulating the plasma density, as this would allow to influence the average wakefield shape. The original idea by R. Brinkmann (DESY) was investigated within the LAOLA collaboration, and published in [111]. For completeness, the concept is reviewed shortly in section 5.1. In the following, the focus lies on one aspect of the method, which is the identification of a parameter set for a laser-driven plasma wakefield. A significant energy spread reduction can be achieved by modulating the plasma density for this parameter set, which is supported by numerical simulations. The limitations of the applicability in terms of bunch charge are discussed at the end of the chapter.

5.1 Review of the Theoretical Concept

In most simulations of plasma accelerators a correlated energy spread of the witness bunch is observed, which originates from the finite bunch length compared to the plasma period, combined with the overlap of focusing and accelerating phases in the wakefield. Stable beam transport in plasma wakefields is only possible in the focusing region, which is shifted by a quarter of the plasma period with respect to the accelerating region, as can be seen in fig. 2.1 on p. 15. As a consequence, the bunch is accelerated on the slope of the longitudinal field, leading to a correlated energy spread. The situation is qualitatively the same in the nonlinear regime. It can therefore be expected that the linearly correlated energy spread, or chirp, forms a large part of the experimentally easily accessible projected energy spread, even though the complete longitudinal phase space of LPA beams has not been measured so far.
In contrast, when accelerating electron bunches in conventional RF cavities, it is possible to position the bunch at the minimum of the longitudinal field, which is referred to as "on-crest" acceleration. There, only a curvature is imprinted on the longitudinal phase space.

By periodically modulating the plasma density, on-crest acceleration can also be achieved in plasma wakefields [111]. Neglecting slippage, which is a slow process, the phase of a witness bunch in the wake is determined by its distance to the driver and by the plasma density. Changing the density then leads to a change of phase. A periodic modulation of the density shifts the bunch between phases where the accelerating field exhibits opposite slopes, and prevents the build-up of a chirp, see figure 5.1(a).

This implies that the bunch is also shifted between the focusing and the defocusing region, as shown in fig. 5.1(b). Analogously to a FODO structure stable beam transport is then possible even if the bunch is temporarily in the defocusing fields.

For a general periodic plasma density profile the effective on-axis longitudinal field is given by the integral over the modulation period λ_{mod} as

$$\bar{E}_z(\zeta) = \frac{1}{\lambda_{\mathrm{mod}}} \int_0^{\lambda_{\mathrm{mod}}} E_z(r=0,\zeta)\,\mathrm{d}z, \tag{5.1}$$

where $E_z(r=0,\zeta)$ is given by eq. (2.10) on page 14 for a linear plasma wakefield and depends, apart from the driver laser parameters, only on the plasma density. On-crest acceleration would be mimicked by choosing the distance ζ behind the driver laser such that the bunch is at the minimum of the effective longitudinal field $\bar{E}_z$.
A criterion for stable transport through the alternating focusing channel can be derived

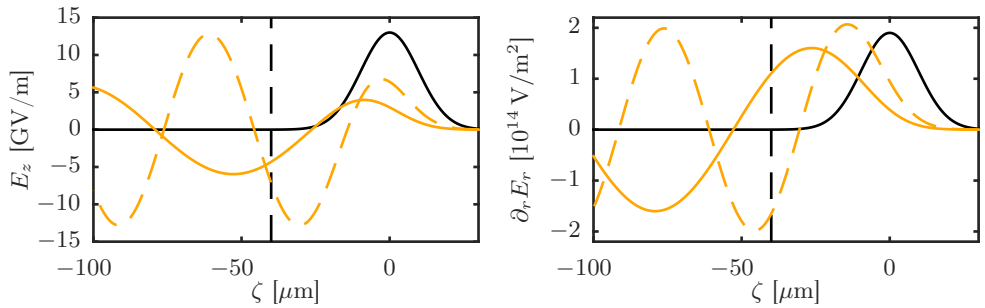

(a) Longitudinal field.

(b) Focusing field.

Figure 5.1 – Illustration of the modulated density concept. A laser ($a^2(\zeta)$ in arb. u. indicated by the solid black lines, $a_0 = 0.8$, $\tau_{\mathrm{FWHM}} = 76\,\mathrm{fs}$, $w_0 = 50\,\mu\mathrm{m}$) drives a linear wake in two different densities, $n_{\mathrm{min}} = 1 \cdot 10^{17}\,\mathrm{cm}^{-3}$ (solid) and $n_{\mathrm{max}} = 3 \cdot 10^{17}\,\mathrm{cm}^{-3}$ (dashed). The bunch position is marked by the dashed black line. Due to the different densities the bunch experiences accelerating fields of opposite slope (a), and also alternatingly focusing and defocusing fields (b).

with the help of beam transport matrices. The transport matrix for the propagation through a section with constant focusing strength K of length s is given by

$$M = \begin{pmatrix} \cos\left(\sqrt{K(\zeta)}s\right) & \sin\left(\sqrt{K(\zeta)}s\right)/\sqrt{K(\zeta)} \\ -\sqrt{K(\zeta)}\sin\left(\sqrt{K(\zeta)}s\right) & \cos\left(\sqrt{K(\zeta)}s\right) \end{pmatrix}. \tag{5.2}$$

The evolution of the focusing strength over one modulation period is approximated by N sections of individually constant focusing strength. The transport matrix over the complete period is given by the multiplication of all individual short matrices M_i as $T = M_N \cdot ... \cdot M_1$. If the trace of T fulfills $|\mathrm{Tr}(T)| < 2$, stable transport is possible [40], and the matched beta function can be calculated as

$$\beta_m(\zeta) = \frac{2\,T(1,2)}{\sqrt{4 - (T(1,1) + T(2,2))^2}}. \tag{5.3}$$

A bunch of this beta function as well as $\alpha_{\mathrm{CS}} = 0$ at the beginning of a modulation period will exit the modulation period with the same Courant-Snyder parameters, which is consequently a stable, periodic solution.

Depending on the shape of the density modulation, as well as on the laser parameters, the minimum of the effective longitudinal field can be at a position ζ where also stable transport is possible. Modulating the plasma density consequently allows to accelerate

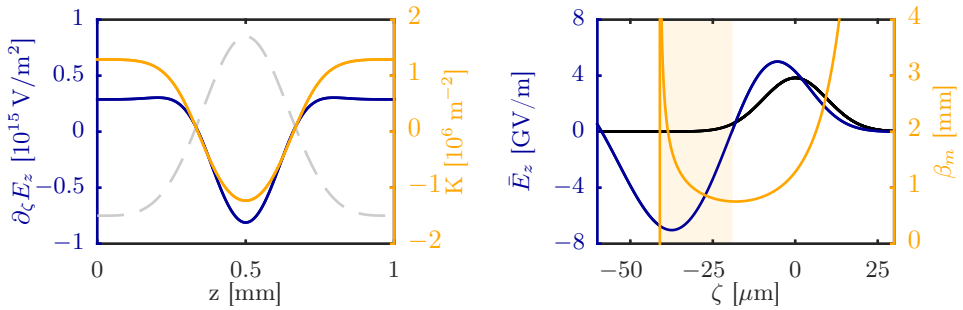

(a) Fields along one λ_{mod}.

(b) Average wakefield.

Figure 5.2 – (a) Evolution of the longitudinal slope of the accelerating field, $\partial_\zeta E_z(\zeta)$ (blue) and of the focusing strength K (yellow) along one modulation period (density profile indicated in arb. u. in dashed gray) at $\zeta = -37\,\mu$m. Both the slope of the longitudinal field and the focusing strength change sign during the modulation period. (b) Average accelerating field over one modulation period λ_{mod} (blue) and matched beta function (yellow) as a function of the distance behind the driver laser (a^2 in arb. u. in black). For $\zeta < -41\,\mu$m no stable transport is possible and the matched beta function diverges. The minimum of the effective longitudinal field $\bar{E}_z$ is within the region of stable transport at around $\zeta = -37\,\mu$m. The fields are calculated using the linear wakefield theory, with parameters from table 5.1.

a witness bunch on-crest in the plasma wakefield. For the parameter set motivated in the next section and summarized in table 5.1, the effective longitudinal field and the matched beta function can be seen in figure 5.2(b). The wakefield is calculated using the linear wakefield approximation, eqs. (2.10)-(2.12) on p. 14. The shaded yellow area covers the distance behind the driver laser where both energy gain and stable transport is possible. In contrast to the linear wakefield in a constant density plasma, compare fig. 2.1 on p. 15, also the minimum as well as part of the negative slope of the effective accelerating field are accessible. For the longitudinal position where the effective accelerating field is minimal, $\zeta = -37\,\mu$m, the evolution of the focusing strength, K, as well as the slope of the longitudinal field, $\partial_\zeta E_z$, over one density modulation period is shown in fig. 5.2(a). Both change sign in the high density region.

5.2 Identification of Demonstration Parameters

The modulated plasma density concept relies on the accessibility of a phase region where the slope of the accelerating field is negative, so that the bunch head is accelerated stronger than the bunch tail. This limits the applicability to the linear or quasi-linear wakefield regime, since in the bubble regime the region of negative slope is very short. Yet, internal injection strategies often operate in the bubble regime, except for some triggered injection schemes like colliding pulse injection [14, 15, 26]. The concept is therefore well suited for the acceleration of externally injected electron bunches. Another advantage of externally injected bunches is the freely tunable injection phase. This might also be possible for internally injected bunches by adjusting the plasma density. However, since this requires precise knowledge of the injection phase and further complicates the scheme, the simulations to demonstrate chirp prevention are performed with an externally injected bunch in the following.

Injected electron bunch

Even if on-crest acceleration is possible, the finite bunch length compared to the plasma period will still cause an increase of the projected energy spread due to the curvature of the effective longitudinal field. Short electron bunches are therefore favorable for the injection. The electron bunch parameters assumed here are similar to current proposed short-bunch machines [112, 113], with a bunch length of $\sigma_z = 1\,\mu\text{m}$ and a low charge of 1 pC, which is typically limited by space charge effects in the accelerator gun. The kinetic energy of 100 MeV is chosen large enough to be relativistic with $\beta \approx 1$ so that slippage is not a dominant effect, but low enough to keep the hypothetical injector comparably short. In conventional machines a low initial relative rms energy spread of $\sigma_\gamma/\gamma = 0.1\,\%$ is achievable, and provides the advantage that the imprinted energy spread from the LPA stage can be clearly identified. Owing to the low charge a normalized transverse emittance of, or even below, the assumed value of $\epsilon_{\text{n},x/y} = 0.5\,\text{mm mrad}$ is realistic.

Plasma density profile

The modulated density profile is given by an expression for the plasma wave number depending on z as

$$k_p(z) = k_{p,\min} + (k_{p,\max} - k_{p,\min}) \cdot \sin^4\left(\frac{\pi z}{\lambda_{\text{mod}}}\right). \tag{5.4}$$

The density then follows as $n(z) = k_p(z)^2 c^2 m_e \epsilon_0 / e^2$. Eq. (5.4) is obtained by a fit to a density profile simulated in the fluid dynamics simulation code OpenFOAM [114] by N. Delbos (CFEL/UHH). The exact modulation shape, however, is not a crucial parameter, as long as the minimum of the effective longitudinal field is still within the stable transport region. Typically, the low density region should be longer than the high density region, since the slope of the longitudinal field E_z is steeper for the higher density due to the shorter plasma period and larger wakefield amplitude there. Only for very long laser pulses the longitudinal field amplitude in the wakefield can be larger in the lower density compared to the high density region. If this effect is stronger than the effect of the plasma wavelength on the slope of the accelerating field, the low density region has to be shorter than the high density region. However, this is only the case if the pulse length is longer than the resonant pulse length of the low plasma density, which is not an efficient choice, and therefore will not be pursued here. The modulation period λ_{mod} is determined by the target design and has to be large enough so that machining of the target is still possible. Furthermore, the modulation period should be larger than the plasma period. Yet, the modulation period also needs to be short enough so that the bunch is not completely defocused in the high density region. The betatron period can be a measure for this limitation. In the plasma it is typically a few millimeters long for a kinetic energy of 100 MeV. Consequently, $\lambda_{\mathrm{mod}} = 1\,\mathrm{mm}$ is used here, and the total target length is 10 mm. For a larger kinetic energy the betatron period increases and the modulation period can also be longer.
The plasma density is chosen in the $10^{17}\,\mathrm{cm}^{-3}$ range, large enough to achieve an average accelerating gradient on the several GV/m level, while providing a long enough plasma period to minimize the contribution of the curvature to the energy spread. The minimum density is $n_{\mathrm{min}} = 1 \cdot 10^{17}\,\mathrm{cm}^{-3}$ and the maximum density is $n_{\mathrm{min}} = 3 \cdot 10^{17}\,\mathrm{cm}^{-3}$. A large difference between the minimum and maximum density shifts the minimum of the effective longitudinal field $\bar{E}_z$ further into the region of stable transport. However, it might also make the target susceptible to spurious density down ramp injection.

Driver Laser

In order to drive a (quasi-)linear wakefield the peak normalized laser vector potential $a_0 = eA/m_e c^2$ has to be around or below 1. It is chosen as $a_0 = 0.8$ here. Yet, as long as the bubble regime is avoided, this is not a sensitive parameter, and could also be larger to increase the accelerating gradient. The laser pulse length is 76 fs FWHM, which is the resonant driver length for the maximum density n_{max}. Like the peak normalized vector potential a_0, the pulse length is not a very sensitive parameter.
Laser guiding beyond the Rayleigh length is typically achieved by creating a preformed

Driver Laser	
spot size w_0	$50\,\mu$m
pulse energy	4 J
pulse length (FWHM)	76 fs
normalized vector potential a_0	0.8
Witness Bunch	
kinetic energy E_{kin}	100 MeV
rms energy spread $\sigma_E/E_{\mathrm{kin}}$	0.1 %
beam size $\sigma_x = \sigma_y$	2 μm
transverse emittance $\epsilon_{n,x} = \epsilon_{\mathrm{n},y}$	0.5 mm mrad
bunch charge Q	1 pC
bunch length σ_z	1 μm
Plasma Parameters	
minimum density n_{min}	$1 \cdot 10^{17}\,\mathrm{cm}^{-3}$
maximum density n_{max}	$3 \cdot 10^{17}\,\mathrm{cm}^{-3}$
modulation period λ_{mod}	1 mm
target length l	10 mm
modulation shape	eq. (5.4)

Table 5.1 – Laser, bunch and plasma parameters for demo simulations of the modulated density concept.

plasma density channel with a capillary discharge (see [115, 116, 31], and further references in [32]). The density in the plasma density channel increases radially, i.e., proportionally to $r = \sqrt{x^2 + y^2}$. This causes a radial change of refractive index, which has a focusing effect on the laser pulse. However, including a discharge into the modulated density target might pose an additional experimental challenge, so that laser guiding is not assumed here. Instead, the laser spot size is chosen as $w_0 = 50\,\mu\text{m}$, so that the Rayleigh length of ideally $z_R = 9.8\,\text{mm}$ is almost as long as the complete target. This also reduces the influence of laser self-focusing, which happens on the scale of the Rayleigh length.

The complete parameter set is summarized in table 5.1.

5.3 Particle-In-Cell Simulations

The setup defined above is simulated with the full 3D PIC code Warp [39]. The vacuum focal position of the laser is in the target center at $z = 5\,\text{mm}$. The position of the witness bunch behind the driver laser at the target entrance, $\zeta = -40\,\mu\text{m}$, is determined from the simulations to minimize the final correlated energy spread. This accounts both for slippage and for the deviations of the wakefield from the linear theory at $a_0 = 0.8$, and is therefore slightly different than the position of minimum effective longitudinal field, $\zeta = -37\,\mu\text{m}$, shown in fig. 5.2(b).
The simulation box volume of $122\,\mu\text{m} \times 200\,\mu\text{m} \times 200\,\mu\text{m}$ is divided into $4892 \times 100 \times 100$ cells with one particle per cell. The simulation is performed in the Lorentz-boosted frame [56] with $\gamma_{\text{boost}} = 8$. For comparison, a case with the same laser and bunch parameters and a constant, intermediate plasma density of $n = 2 \cdot 10^{17}\,\text{cm}^{-3}$ is simulated, where the bunch is positioned in the constant focusing region at $\zeta = -39\,\mu\text{m}$. This density is not only chosen for being in the middle between the minimum and maximum density, but also because the plasma wavelength there is $\lambda_p = 75\,\mu\text{m}$, which provides a similar longitudinal field period as given by the effective longitudinal field in the modulated density target. Also here, due to the onset of wakefield nonlinearities, the bunch position, $\zeta = -39\,\mu\text{m}$, can be chosen farther away from the laser than indicated by the plasma wavelength in the linear theory.

Figure 5.3 shows the bunch evolution through the 10 mm long target for the reference case and for the modulated density case. The beam size (fig. 5.3(b)) decreases and oscillates slowly and very similarly in both cases. The decrease can be attributed to a smaller matched beam size as the bunch slips towards the laser in combination with the energy gain. The oscillation might be caused by the matched beam size being slightly smaller than the injected beam size of $\sigma_x = 2\,\mu\text{m}$. However, the emittance

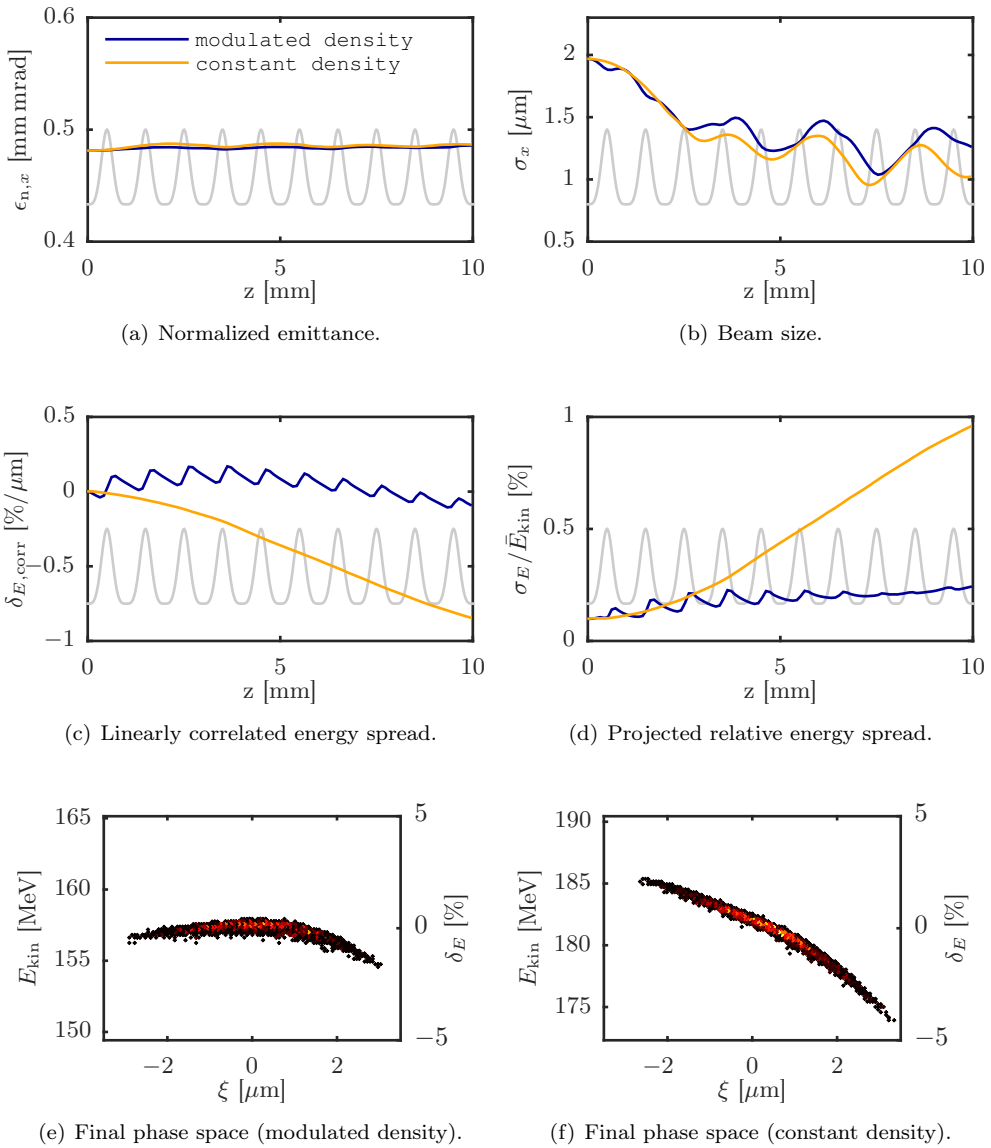

(a) Normalized emittance.

(b) Beam size.

(c) Linearly correlated energy spread.

(d) Projected relative energy spread.

(e) Final phase space (modulated density).

(f) Final phase space (constant density).

Figure 5.3 – Bunch evolution in the plasma target either for a constant density (yellow) or a modulated density (blue). For symmetry reasons only the x plane is shown in (a) and (b). The modulated plasma profile is sketched in gray. Figs. (e) and (f) show the final longitudinal phase space at the end of the target at $z = 10\,\mathrm{mm}$.

growth (fig. 5.3(a)) is negligible in both cases, as the deviation from the ideal matched beam size is very small, and also since only a few betatron periods fit into the target length.
The linearly correlated energy spread shown in fig. 5.3(c) is calculated like $\delta_{E,\mathrm{corr}} = \langle \xi E_{\mathrm{kin}} \rangle / (\bar{E}_{\mathrm{kin}} \sigma_z^2)$. The angle brackets are defined as

$$\langle \xi E_{\mathrm{kin}} \rangle = \frac{\sum_{i=1}^{N} \xi_i E_{\mathrm{kin},i}}{N} - \frac{\sum_{i=1}^{N} \xi_i \sum_{i=1}^{N} E_{\mathrm{kin},i}}{N^2}, \tag{5.5}$$

with the sums over all N particles of the bunch and ξ the internal longitudinal bunch coordinate. In the constant density case, the linearly correlated energy spread, or chirp, falls from initially 0 to $-0.8\,\%/\mu$m at the end of the target. The chirp decreases faster at the end of the target, when the bunch has left the region near the minimum of the longitudinal field and has slipped towards the driver laser. In the case of the modulated density, the chirp decreases in the low density regions and increases in the high density regions, which leads to a saw-tooth-like behaviour. At the end of the target, the correlated energy spread amounts to only $-0.09\,\%/\mu$m. Slippage causes a slow increase of the chirp in the first half and a slow decrease in the second half of the target, as the bunch is injected with a slightly larger than optimum distance to the driver laser and slips across the minimum of effective longitudinal field. The correlated energy spread crosses zero near the end of the target, which means that it can be completely eliminated by tuning the injection phase more precisely. Experimentally, the energy spread can be used as a feedback to optimize the injection phase. This assumes a small enough arrival time jitter, which is a prerequisite for any external injection experiment.
Note that this 3D simulation using a finite-difference time domain solver is resolved with 32 cells per laser wavelength, so that a slight overestimation of the slippage due to spurious numerical dispersion is possible. However, in any case slippage is not a dominant effect here, and could also be compensated experimentally by introducing an up ramp density taper [68] or by properly choosing the injection phase, as done here.

The projected final relative rms energy spread, fig. 5.3(d), is dominated by the chirp for a constant plasma density and rises to 0.96 %. In the modulated density case, it is reduced to 0.24 %, while the slice energy spread in the bunch center at $\xi = 0$ has increased only from 0.10 % to 0.11 %. The main contribution to the projected energy spread consequently is from the remaining chirp, as well as from higher order correlations in the energy spread, such as from the curvature. This can also be observed in the final longitudinal phase space shown in figure 5.3(e).
Compared to the constant density case, the net accelerating gradient is reduced by the density modulation. The initial mean energy was 100 MeV in both cases, while

the final mean energy after 10 mm propagation is 181 MeV or 157 MeV in the constant or modulated density case, respectively. Yet, this reduction appears acceptable considering the achieved beam quality.

5.4 Charge Limitation

In the example discussed above the bunch charge is low with 1 pC, and the peak current amounts to 120 A. Typically, the achievable charge is limited by space charge effects at the photocathode of the conventional, short bunch machine. However, especially for FEL applications, a large bunch charge and consequently high current is desirable. Therefore, the applicability of the modulated density concept to bunches carrying more charge is discussed in this section.
Higher charge will lead to more pronounced beam loading, i.e., to the modification of the wakefield due to the wake driven by the witness bunch itself. Inside the short bunch, the slope of the beam-driven longitudinal wakefield is always negative. It therefore counteracts the slope of the laser-driven wakefield in the focusing phase region. An example is shown in figure 5.4. The on-axis longitudinal field $E_z(\zeta)$ from 3D PIC simulations is given for a bunch charge of 1 pC and of 4 pC, and a constant plasma density of $n = 2 \cdot 10^{17}\,\mathrm{cm}^{-3}$. The wakefield behind the bunch is modified by beam loading. At the head of the bunch around $\zeta = -35\,\mu\mathrm{m}$ the beam-driven wakefield is not yet built up and no difference depending on the bunch charge is visible in the longitudinal field, while at the center of the bunch at $\zeta = -39\,\mu\mathrm{m}$ a change of the slope of the longitudinal field is clearly visible.

In order to compensate for larger beam loading in the case of a modulated density target, the distance of the bunch behind the laser can be decreased, so that the slope of the effective longitudinal field increases, compare fig. 5.2(b). An example for the bunch charge of 4 pC is shown in figure 5.5. In this 3D WARP simulation all parameters are the same as for the case shown in fig. 5.3, compare table 5.1, except for the bunch charge and the injection phase. The bunch is injected at $\zeta = -37\,\mu\mathrm{m}$, in contrast to the previously used $-40\,\mu\mathrm{m}$. The change of injection phase compensates for the increased beam loading and the linearly correlated energy spread is only $0.004\,\%/\mu\mathrm{m}$ at the end of the target. With $\sigma_E/\bar{E}_{\mathrm{kin}} = 0.31\,\%$ the final projected rms energy spread is slightly larger than in the case with 1 pC bunch charge ($\sigma_E/\bar{E}_{\mathrm{kin}} = 0.24\,\%$). This is caused by higher order correlations of the energy spread, which are visible in the longitudinal phase space in fig. 5.5(b).

However, a certain amount of beam loading can prevent the build-up of a chirp also for a constant density plasma, as has been proposed already in 1987 [108]. Ideally,

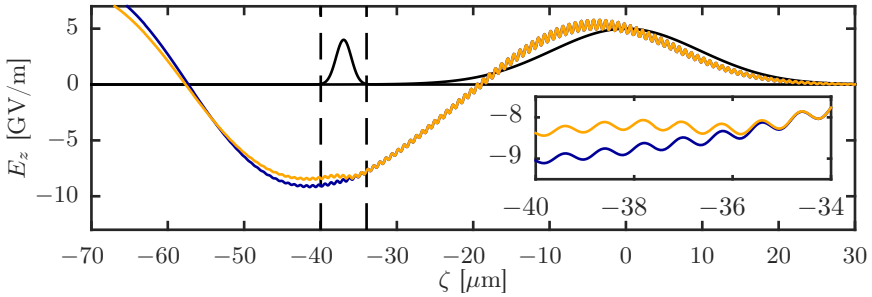

Figure 5.4 – Longitudinal on-axis field $E_z(r = 0, \zeta)$ in the center of the 10 mm long target for laser parameters given in table 5.1 and a constant density of $n = 2 \cdot 10^{17}\,\mathrm{cm}^{-3}$. The laser intensity and the bunch current profile are indicated in arb. u. in black. The bunch extent in $\pm 3\sigma_z$ is marked in dashed black. The inset shows the longitudinal field in $\pm 3\sigma_z$ of the bunch. The blue line corresponds to a bunch charge of 1 pC, and the yellow line corresponds to a bunch charge of 4 pC. From 3D WARP simulations.

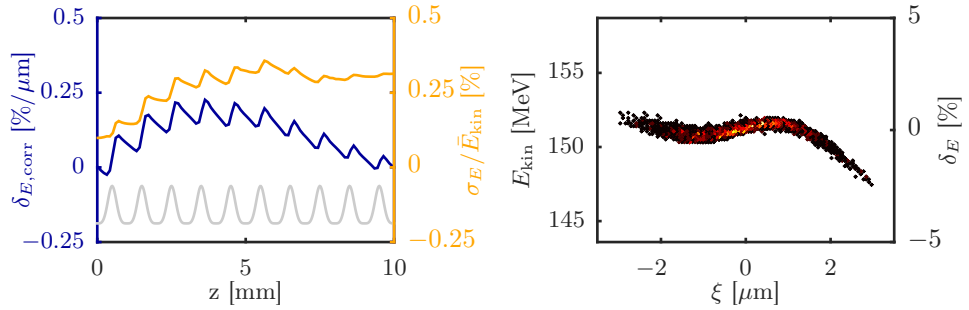

(a) Projected and linearly correlated energy spread.

(b) Final phase space.

Figure 5.5 – (a) Energy spread evolution and (b) final longitudinal phase space from a PIC simulation assuming 4 pC bunch charge (other parameters like in table 5.1). The bunch is injected nearer to the driver laser at $\zeta = -37\,\mu$m to compensate for the increased influence of beam loading. Higher order correlations of the energy spread are visible in the phase space, which originate from the wakefield modification due to the beam-driven wake, i.e., from beam loading.

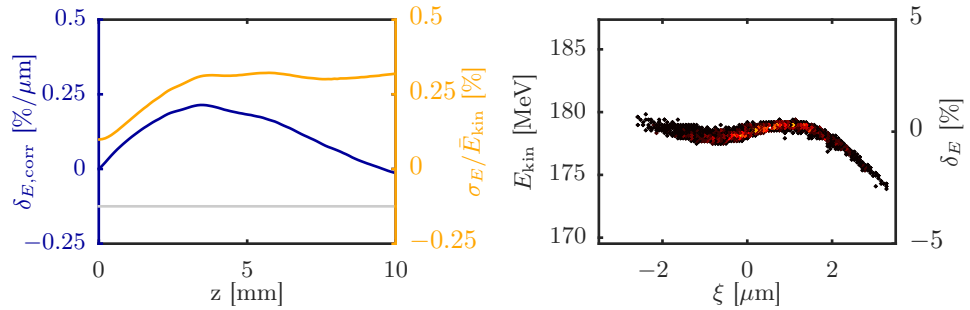

(a) Projected and linearly correlated energy spread.

(b) Final phase space.

Figure 5.6 – (a) Energy spread evolution and (b) final longitudinal phase space from a PIC simulation assuming 4 pC bunch charge and $n = 2 \cdot 10^{17}\,\mathrm{cm}^{-3}$. The bunch is injected at $\zeta = -39\,\mu$m, which is the same position as in the case with 1 pC charge (compare fig. 5.3). The higher order correlations of the energy spread visible in the longitudinal phase space are very similar to the case using a modulated density target shown in fig. 5.5.

this requires a triangular current profile to also cancel higher order correlations of the energy spread. For a Gaussian current profile some correlations will remain, but the linear correlation can still be avoided [108].
As the slope of the longitudinal field is smaller further away from the laser, i.e., nearer to the defocusing region, the witness bunch position where this can be expected to happen for the lowest bunch charge is previously used $\zeta = -39\,\mu$m in the reference case. The charge is scanned in 1 pC steps in PIC simulations for a constant density of $2 \cdot 10^{17}\,\mathrm{cm}^{-3}$, and the smallest final linearly correlated energy spread is obtained for 4 pC and amounts to $-0.01\,\%/\mu$m. Fig. 5.6 shows the energy spread evolution and the final longitudinal phase space. Like for the modulated density case, the slow rise of the linearly correlated energy spread $\delta_{E,\mathrm{corr}}$ during the first few mm and the compensation to almost 0 in the second half of the target is characteristic for slippage through the optimum phase region. The final projected rms energy spread amounts to 0.32 %. Also the shape of the longitudinal phase space is very similar to the one from the modulated density target, see fig. 5.5. As the slope of the longitudinal field depends on ζ, this result is strictly valid only for the chosen bunch position of $\zeta = -39\,\mu$m. For $\zeta > -39\,\mu$m the slope of the laser-driven wakefield is larger, which implies that at these phases also bunches carrying more charge can be accelerated without accumulating a large correlated energy spread. However, also the accelerating gradient is smaller there.

The injection phase consequently can be adjusted to the bunch charge to achieve a minimal final energy spread, at the cost of a reduced accelerating gradient.

For the parameters considered in this chapter, the bunch charge of 4 pC can be viewed as the limit for the applicability of the modulated density concept. While it is possible for this charge to obtain the same results with a modulated density target as with a constant density target, modulating the density does not provide an additional benefit. In contrast, for lower charge, where beam loading is not as pronounced, modulating the density does have the advantage of significantly reducing the linearly correlated energy spread and consequently also the projected energy spread.
Above 4 pC beam loading will increase even more. In this regime, the slope of the longitudinal field inside the bunch is dominated by the beam-driven wake. A positive chirp will be imprinted on the bunch for both plasma profiles, severely hampering the beam quality. In this regime, other approaches have to be found to increase the possible bunch charge, such as adjusting the bunch phase or relaxing the matched beam size by increasing the driver laser spot size or by shaping the driver laser pulse with a superposition of modes [117].

5.5 Summary

This chapter was concerned with a new approach to shape the wakefield and to thereby mitigate the build-up of an energy chirp on the witness bunch. A parameter set has been identified where the proposed density modulation [111] can significantly improve the beam quality in terms of energy spread, and numerical simulations to support this have been performed. As the modulated density concept relies on the linear wakefield regime, the considered parameter set assumes the external injection of an ultrashort electron bunch. It has been shown with PIC simulations that the projected relative rms energy spread can be reduced by a factor of four compared to a case with intermediate, constant plasma density. The price to pay is a reduction of the net accelerating gradient by 30 %.
The concept works well for the low charge bunches that can be expected for ultrashort bunches produced from state-of-the-art conventional accelerators [112, 113]. However, as soon as beam loading dominates, the slope of the accelerating field changes sign inside the bunch. This cannot be compensated by modulating the density. For the parameter set used here this threshold is around 4 pC.

6 Conclusion and Outlook

The beam quality of Laser-Plasma Accelerators, especially regarding energy spread and divergence, is one of the most critical open questions on the way to a laser-driven brilliant light source. This thesis therefore is concerned with the theoretical and numerical treatment of three different aspects how to tackle this issue.

Chapter 3 introduced a new technique to directly diagnose the longitudinal phase space that makes use of a laser-driven wakefield. This allows to gain access to the current profile and also to the slice energy spread, which are both crucial quantities for FEL performance. Due to the high gradients achievable in plasma wakefields a temporal resolution around one femtosecond or even in the attosecond range appears feasible. At the same time, the setup is short with only a few millimeters length and therefore well suited for compact accelerators. The technique does not require additional equipment in a laser-plasma acceleration environment, where a high-power laser system and a plasma target are needed for the acceleration in any case.
For experiments aiming at external injection the plasma-based transverse deflector offers the unique possibility to diagnose the injected bunch directly at the injection position – a feat that would be impossible with a transverse deflecting RF-cavity.
The REGAE external injection experiment is a promising candidate for a proof-of-principle experiment of the plasma-based streaking concept. The currently foreseen instrumentation at REGAE is sufficient to show a femtosecond resolution without any further modifications. However, a major challenge for the successful operation are timing jitters between the driver laser and the diagnosed bunch. Due to the strong slope of the deflecting field these are directly translated into a steering of the beam, making it hard to transport. While those shots that crossed the plasma at the correct phase do not steer and still reach the screen, a large arrival time jitter will hamper the experimental calibration. In such a case, the flexible adjustment of the used plasma density or laser intensity allows to increase the tolerance towards timing jitters at the cost of a loss of temporal resolution.
One of the experimental goals of the external injection experiment at REGAE is to gain information on the plasma wakefield, a capability that could also be used to calibrate the transverse deflection. By benchmarking numerical simulations to the calibration obtained for a more relaxed parameter set, it might then be possible to validate the

wakefield modeling. This could allow to scale the numerically obtained calibration to larger deflecting voltages, where a direct calibration is not possible.
Due to its high temporal resolution, the plasma-based transverse deflector is a promising candidate to diagnose a new phase space linearization concept proposed in [65, 24]. The demonstration of this concept is planned at REGAE, and in simulations ultrashort electron bunches of around 1 fs have been achieved at a very low charge of a few fC. The low charge makes a CTR measurement extremely challenging, if not impossible. Yet, the TDP does not have a low charge limit, as long as the transverse beam profile can be detected, which has been achieved even for single electrons at REGAE [118]. A possible issue might be the transverse electron beam size, which needs to be much smaller than the laser spot size for the TDP. For the phase space linearization, however, so far only designs for large electron beam sizes exist, and further studies are necessary to reduce the electron beam size while maintaining the short bunch length. Apart from the TDP, no other diagnostics has been proposed yet to demonstrate this phase space linearization concept.
Arrival time jitters are a challenge mainly for hybrid acceleration schemes where an RF to optical synchronization is needed. In all-optical plasma accelerators the electron bunch is intrinsically synchronized to the driver laser pulse. Consequently, a part of the laser that is split off to drive the transverse deflector stage is also synchronized to the bunch.
An all-optical staging setup, however, poses other challenges. In between the two stages, the first laser needs to be coupled out and the second laser has to be coupled into the electron beam line. In ref. [25] this is solved with a tape-based plasma-mirror, achieving a distance of only a few centimeters between the stages. However, the beam emittance deteriorates during the passage through the tape. To avoid this, a much longer emittance-conserving beam transport line between the two stages would be needed, so that enough space is available to place mirrors.

The issue of transporting LPA beams while conserving the emittance was subject of chapter 4. With the help of adiabatic matching sections at the exit and, for externally injected beams, also at the entrance of the plasma target the beam size could be significantly increased. This reduces the beam divergence before and after the target and thereby suppresses chromatic emittance growth.
Two different strategies how to achieve an adiabatic extraction have been proposed, either to taper the laser intensity or the plasma density. For low charge bunches, as in the example of a hybrid accelerator, increasing the laser spot size and consequently decreasing its intensity according to the ideal profile yields a divergence reduction of more than a factor of four. However, for higher bunch charge as is often the case for internal injection, the pure laser tapering is not a good option. The beam continues

to drive its own wakefield after the laser intensity has dropped, the beam size therefore remains small, and even additional emittance growth occurs. Consequently, the wakefield driven by the beam itself has to be reduced by tapering the plasma density. The bunch charge is only one aspect that influences the matching section design. For example, the bunch phase at the end of the target has to be taken into account, too, as a density down ramp causes different focusing strength profiles depending on the initial bunch phase. Practical considerations like the existence of a laser guiding channel or the total available target length may also play a role. The matching sections therefore have to be tailored to the specific setup. Furthermore, a real target can very well combine both strategies, the laser and the density tapering, like in the discussed internal injection example.
The application of adiabatic matching sections can be tested at the external injection experiment at the REGAE accelerator [24]. There, the tapering is mainly caused by the change of laser spot size as the laser undergoes its focus, which is a comparably slow process due to the long Rayleigh length.

Chapter 5 dealt with the correlated energy spread of LPA beams. The modulated plasma density concept aims at removing the negatively correlated energy spread. Such a chirp occurs for negligible beam loading as the bunch is accelerated on the slope of the longitudinal field in the focusing region of the laser-driven wake, so that the energy gain is larger in the bunch tail. By modulating the plasma density, the bunch is periodically shifted to the defocusing region and the chirp is canceled out.
The idea relies on the linear or quasi-linear regime, as only there a significantly long defocusing region is present in the wakefield. It is therefore well suited mainly for externally injected beams.
The method approaches its limits as soon as beam loading considerably deforms the laser-driven wakefield. This changes the slope of the accelerating field and eventually also the sign of the correlated energy spread. For the case considered here, a charge of 4 pC presents this limit, which corresponds to a peak current of 0.5 kA. On the one hand, such a beam current is high for state-of-the-art conventional short bunch machines that could be used as injectors for hybrid accelerators. The modulated density concept here is a good option to conserve the beam quality. On the other hand, keeping FEL applications in mind, the option to scale to higher currents is desirable. Further studies therefore are required to investigate how beam loading can be suppressed. This is a general issue that the modulated density concept shares also with concepts featuring constant plasma density targets. A way to increase the bunch charge that can be accelerated without accumulating a large correlated energy spread is to shift the witness bunch further towards the driver laser, as in this phase region the slope of the longitudinal field is larger. This option does not require a modulated density profile, comes at the cost of a reduced accelerating gradient, and causes higher

order correlations of the energy spread. Yet, since for an FEL application especially the beam shape in the current peak is of interest, this could be an option to maintain the beam quality specifically in this region. Another way is to shape the transverse laser profile to influence the focusing forces of the wakefield. This can be used to increase the matched beam size, as proposed in [117] for a constant plasma density target.
Furthermore, it is worth exploring what other applications of the modulated density methods are possible. Generally speaking, it provides a tool to shape the laser-driven wakefield. For example, with a suitable density profile it might be possible to remove also the remaining higher order correlations of the accelerating field, or to adjust the laser-driven wakefield shape to the expected beam-driven component. Another application could be the cancellation of a previously accumulated negative chirp, as – in contrast to a constant density target – the modulated density concept provides the freedom to accelerate the bunch at the negative slope of the longitudinal field.
The large energy spread is currently one of the main concerns regarding laser-plasma driven brilliant light sources. Even if the modulated density concept proves to be generally limited to comparably low bunch charge, it nevertheless provides another method towards the application of LPA beams.

It is an attractive option to test the modulated plasma density concept at the external injection experiment at REGAE. However, for the design of such a test a few issues still need to be investigated. First, to reduce the gas load in the target chamber, the density is in the $10^{16}\,\mathrm{cm}^{-3}$ range, and therefore the technical feasibility of a modulated density target in this density range needs to be explored. Furthermore, the low kinetic energy of the REGAE beam will lead to more pronounced slippage effects, so that the beam could slip out of the stable transport region. If this proves to be the case, slippage can be easily circumvented by shortening the target or by introducing an up ramp taper of the density [68]. The low kinetic energy also implies a short betatron period. As the modulation period of the plasma density has to be shorter than the betatron period to avoid emittance growth, this poses an additional challenge to the target design and fabrication. However, this requirement can be relaxed by reducing the laser intensity, which decreases the focusing strength in the wakefield. The laser intensity is also a critical parameter from another point of view, namely the wakefield regime. The modulated density concept relies on the (quasi-)linear regime. Due to the low density, however, it is possible to access the bubble regime already at comparably small a_0 [32]. To avoid this, the laser intensity can be reduced, which is experimentally straightforward.
In this way, the external injection experiment at REGAE can be a possible testbed for all three concepts discussed here, for the transverse deflecting plasma stage, for the adiabatic matching sections and also for the modulated plasma density concept.

List of Figures

Bibliography

[1] O. Lundh, J. Lim, C. Rechatin, L. Ammoura, A. Ben-Ismail, X. Davoine, G. Gallot, J.-P. Goddet, E. Lefebvre, V. Malka, and J. Faure, "Few femtosecond, few kiloampere electron bunch produced by a laser-plasma accelerator," *Nat. Phys.*, vol. 7, pp. 219–222, 2011. http://dx.doi.org/10.1038/nphys1872

[2] A. Buck, M. Nicolai, K. Schmid, C. M. S. Sears, A. Savert, J. M. Mikhailova, F. Krausz, M. C. Kaluza, and L. Veisz, "Real-time observation of laser-driven electron acceleration," *Nat. Phys.*, vol. 7, pp. 543–548, 2011. http://dx.doi.org/10.1038/nphys1942

[3] F. Grüner, S. Becker, U. Schramm, T. Eichner, M. Fuchs, R. Weingartner, D. Habs, J. Meyer-ter Vehn, M. Geissler, M. Ferrario, L. Serafini, B. van der Geer, H. Backe, W. Lauth, and S. Reiche, "Design considerations for table-top, laser-based VUV and X-ray free electron lasers," *Applied Physics B*, vol. 86, no. 3, pp. 431–435, 2007. http://dx.doi.org/10.1007/s00340-006-2565-7

[4] C. B. Schroeder, W. M. Fawley, F. Grüner, M. Bakeman, K. Nakamura, K. E. Robinson, C. Tóth, E. Esarey, and L. W. P., "Free-electron laser driven by the LBNL laser-plasma accelerator," *AIP Conference Proceedings*, vol. 1086, no. 1, p. 637, 2009. http://scitation.aip.org/content/aip/proceeding/aipcp/10.1063/1.3080982

[5] A. R. Maier, A. Meseck, S. Reiche, C. B. Schroeder, T. Seggebrock, and F. Grüner, "Demonstration Scheme for a Laser-Plasma-Driven Free-Electron Laser," *Phys. Rev. X*, vol. 2, p. 031019, 2012. http://link.aps.org/doi/10.1103/PhysRevX.2.031019

[6] Z. Huang, Y. Ding, and C. B. Schroeder, "Compact X-ray Free-Electron Laser from a Laser-Plasma Accelerator Using a Transverse-Gradient Undulator," *Phys. Rev. Lett.*, vol. 109, p. 204801, 2012. http://link.aps.org/doi/10.1103/PhysRevLett.109.204801

[7] M. Fuchs, R. Weingartner, A. Popp, Z. Major, S. Becker, J. Osterhoff, I. Cortrie, B. Zeitler, R. Hörlein, G. D. Tsakiris, U. Schramm, T. P. Rowlands-Rees, S. M. Hooker, D. Habs, F. Krausz, S. Karsch, and F. Grüner,

"Laser-driven soft-X-ray undulator source," *Nat. Phys.*, vol. 5, p. 826, 2009. http://www.nature.com/nphys/journal/v5/n11/full/nphys1404.html

[8] A. R. Maier, "Generation and Characterization of Few-Fs X-Ray Pulses," Ph.D. dissertation, Universität Hamburg, 2012.

[9] W. P. Leemans, A. J. Gonsalves, H.-S. Mao, K. Nakamura, C. Benedetti, C. B. Schroeder, C. Tóth, J. Daniels, D. E. Mittelberger, S. S. Bulanov, J.-L. Vay, C. G. R. Geddes, and E. Esarey, "Multi-GeV Electron Beams from Capillary-Discharge-Guided Subpetawatt Laser Pulses in the Self-Trapping Regime," *Phys. Rev. Lett.*, vol. 113, p. 245002, Dec 2014. http://link.aps.org/doi/10.1103/PhysRevLett.113.245002

[10] X. Wang, R. Zgadzaj, N. Fazel, Z. Li, S. A. Yi, W. Henderson, Y.-Y. Chang, R. Korzekwa, H.-E. Tsai, C. Pai, H. Quevedo, G. Dyer, E. Gaul, M. Martinez, A. C. Bernstein, T. Borger, M. Spinks, M. Donovan, V. Khudik, G. Shvets, T. Ditmire, and M. C. Downer, "Quasi-monoenergetic laser-plasma acceleration of electrons to 2 GeV," *Nat. Commun.*, vol. 4, p. 1988, 2013. http://dx.doi.org/10.1038/ncomms2988

[11] H. T. Kim, K. H. Pae, H. J. Cha, I. J. Kim, T. J. Yu, J. H. Sung, S. K. Lee, T. M. Jeong, and J. Lee, "Enhancement of Electron Energy to the Multi-GeV Regime by a Dual-Stage Laser-Wakefield Accelerator Pumped by Petawatt Laser Pulses," *Phys. Rev. Lett.*, vol. 111, p. 165002, 2013. http://link.aps.org/doi/10.1103/PhysRevLett.111.165002

[12] S. Bulanov, N. Naumova, F. Pegoraro, and J. Sakai, "Particle injection into the wave acceleration phase due to nonlinear wake wave breaking," *Phys. Rev. E*, vol. 58, pp. R5257–R5260, 1998. http://link.aps.org/doi/10.1103/PhysRevE.58.R5257

[13] D. Umstadter, J. K. Kim, and E. Dodd, "Laser Injection of Ultrashort Electron Pulses into Wakefield Plasma Waves," *Phys. Rev. Lett.*, vol. 76, pp. 2073–2076, 1996. http://link.aps.org/doi/10.1103/PhysRevLett.76.2073

[14] E. Esarey, R. F. Hubbard, W. P. Leemans, A. Ting, and P. Sprangle, "Electron Injection into Plasma Wakefields by Colliding Laser Pulses," *Phys. Rev. Lett.*, vol. 79, p. 2682, 1997. http://link.aps.org/doi/10.1103/PhysRevLett.79.2682

[15] J. Faure, C. Rechatin, A. Norlin, A. Lifschitz, Y. Glinec, and V. Malka, "Controlled injection and acceleration of electrons in plasma wakefields by colliding laser pulses," *Nature*, vol. 444, p. 737, 2006. http://dx.doi.org/10.1038/nature05393

[16] E. Oz, S. Deng, T. Katsouleas, P. Muggli, C. D. Barnes, I. Blumenfeld, F. J. Decker, P. Emma, M. J. Hogan, R. Ischebeck, R. H. Iverson, N. Kirby, P. Krejcik, C. O'Connell, R. H. Siemann, D. Walz, D. Auerbach, C. E. Clayton, C. Huang, D. K. Johnson, C. Joshi, W. Lu, K. A. Marsh, W. B. Mori, and M. Zhou, "Ionization-Induced Electron Trapping in Ultrarelativistic Plasma Wakes," *Phys. Rev. Lett.*, vol. 98, p. 084801, 2007. http://link.aps.org/doi/10.1103/PhysRevLett.98.084801

[17] T. P. Rowlands-Rees, C. Kamperidis, S. Kneip, A. J. Gonsalves, S. P. D. Mangles, J. G. Gallacher, E. Brunetti, T. Ibbotson, C. D. Murphy, P. S. Foster, M. J. V. Streeter, F. Budde, P. A. Norreys, D. A. Jaroszynski, K. Krushelnick, Z. Najmudin, and S. M. Hooker, "Laser-Driven Acceleration of Electrons in a Partially Ionized Plasma Channel," *Phys. Rev. Lett.*, vol. 100, p. 105005, 2008. http://link.aps.org/doi/10.1103/PhysRevLett.100.105005

[18] A. Pak, K. A. Marsh, S. F. Martins, W. Lu, W. B. Mori, and C. Joshi, "Injection and trapping of tunnel-ionized electrons into laser-produced wakes," *Phys. Rev. Lett.*, vol. 104, p. 025003, 2010. http://link.aps.org/doi/10.1103/PhysRevLett.104.025003

[19] C. McGuffey, A. G. R. Thomas, W. Schumaker, T. Matsuoka, V. Chvykov, F. J. Dollar, G. Kalintchenko, V. Yanovsky, A. Maksimchuk, K. Krushelnick, V. Y. Bychenkov, I. V. Glazyrin, and A. V. Karpeev, "Ionization Induced Trapping in a Laser Wakefield Accelerator," *Phys. Rev. Lett.*, vol. 104, p. 025004, 2010. http://link.aps.org/doi/10.1103/PhysRevLett.104.025004

[20] B. B. Pollock, C. E. Clayton, J. E. Ralph, F. Albert, A. Davidson, L. Divol, C. Filip, S. H. Glenzer, K. Herpoldt, W. Lu, K. A. Marsh, J. Meinecke, W. B. Mori, A. Pak, T. C. Rensink, J. S. Ross, J. Shaw, G. R. Tynan, C. Joshi, and D. H. Froula, "Demonstration of a Narrow Energy Spread, ~ 0.5 GeV Electron Beam from a Two-Stage Laser Wakefield Accelerator," *Phys. Rev. Lett.*, vol. 107, p. 045001, 2011. http://link.aps.org/doi/10.1103/PhysRevLett.107.045001

[21] B. Zeitler, I. Dornmair, T. Gehrke, M. Titberidze, A. R. Maier, B. Hidding, K. Flöttmann, and F. Grüner, "Merging conventional and laser wakefield accelerators," in *SPIE Optics + Optoelectronics*, E. Esarey, C. B. Schroeder, W. P. Leemans, K. W. D. Ledingham, and D. A. Jaroszynski, Eds., vol. 8779. SPIE, May 2013, p. 877904. http://dx.doi.org/10.1117/12.2019339

[22] A. R. Rossi, A. Bacci, M. Belleveglia, E. Chiadroni, A. Cianchi, G. D. Pirro, M. Ferrario, A. Gallo, G. Gatti, C. Maroli, A. Mostacci, V. Petrillo, L. Serafini, P. Tomassini, and C. Vaccarezza, "The External-Injection experiment at the SPARC_LAB facility," *Nuclear Instruments and Methods*

in Physics Research Section A: Accelerators, Spectrometers, Detectors and Associated Equipment, vol. 740, pp. 60 – 66, 2014, proceedings of the first European Advanced Accelerator Concepts Workshop 2013. http://www.sciencedirect.com/science/article/pii/S016890021301454X

[23] R. Assmann, C. Behrens, R. Brinkmann, U. Dorda, K. Flöttmann, B. Foster, J. Grebenyuk, M. Gross, I. Hartl, M. Hüning, F. Kärtner, B. Marchetti, Y. Nie, J. Osterhoff, A. Rühl, H. Schlarb, B. Schmidt, F. Stephan, A. S. Müller, M. Schuh, F. Grüner, B. Hidding, A. R. Maier, and B. Zeitler, "SINBAD - A proposal for a dedicated accelerator research facility at DESY," *Proceedings of IPAC2014, Dresden, Germany*, p. TUPME047, 2014.

[24] B. Zeitler, "Phase Space Linearization and External Injection of Electron Bunches into Laser-Driven Plasma Wakefields at REGAE," Ph.D. dissertation, Universität Hamburg, 2016.

[25] S. Steinke, J. van Tilborg, C. Benedetti, C. G. R. Geddes, C. B. Schroeder, J. Daniels, K. K. Swanson, A. J. Gonsalves, K. Nakamura, N. H. Matlis, B. H. Shaw, E. Esarey, and W. P. Leemans, "Multistage coupling of independent laser-plasma accelerators," *Nature*, vol. 530, p. 190, 2016. http://dx.doi.org/10.1038/nature16525

[26] C. Rechatin, J. Faure, A. Ben-Ismail, J. Lim, R. Fitour, A. Specka, H. Videau, A. Tafzi, F. Burgy, and V. Malka, "Controlling the Phase-Space Volume of Injected Electrons in a Laser-Plasma Accelerator," *Phys. Rev. Lett.*, vol. 102, p. 164801, 2009. http://link.aps.org/doi/10.1103/PhysRevLett.102.164801

[27] A. J. Gonsalves, K. Nakamura, C. Lin, D. Panasenko, S. Shiraishi, T. Sokollik, C. Benedetti, C. B. Schroeder, C. G. R. Geddes, J. van Tilborg, J. Osterhoff, E. Esarey, C. Toth, and W. P. Leemans, "Tunable laser plasma accelerator based on longitudinal density tailoring," *Nat. Phys.*, vol. 7, no. 11, pp. 862–866, 2011. http://dx.doi.org/10.1038/nphys2071

[28] C. Behrens, F.-J. Decker, Y. Ding, V. A. Dolgashev, J. Frisch, Z. Huang, P. Krejcik, H. Loos, A. Lutman, T. J. Maxwell, J. Turner, J. Wang, M.-H. Wang, J. Welch, and J. Wu, "Few-femtosecond time-resolved measurements of X-ray free-electron lasers," *Nat. Commun.*, vol. 5, 2014. http://dx.doi.org/10.1038/ncomms476210.1038/ncomms4762

[29] K. Floettmann, "Some basic features of the beam emittance," *Phys. Rev. ST Accel. Beams*, vol. 6, p. 034202, 2003. http://link.aps.org/doi/10.1103/PhysRevSTAB.6.034202

[30] R. J. Goldston and P. H. Rutherford, *Introduction to Plasma Physics*. New York: Taylor & Francis Group, 1995.

[31] A. J. Gonsalves, T. P. Rowlands-Rees, B. H. P. Broks, J. J. A. M. van der Mullen, and S. M. Hooker, "Transverse Interferometry of a Hydrogen-Filled Capillary Discharge Waveguide," *Phys. Rev. Lett.*, vol. 98, p. 025002, 2007. http://link.aps.org/doi/10.1103/PhysRevLett.98.025002

[32] E. Esarey, C. B. Schroeder, and W. P. Leemans, "Physics of laser-driven plasma-based electron accelerators," *Rev. Mod. Phys.*, vol. 81, p. 1229, 2009. http://dx.doi.org/10.1103/RevModPhys.81.1229

[33] M. Fuchs, "Laser-Driven Soft-X-Ray Undulator Source," Ph.D. dissertation, Ludwig-Maximilians-Universität München, 2010.

[34] P. Gibbon, *Short Pulse Laser Interactions with Matter*. London: Imperial College Press, 2005.

[35] T. J. Mehrling, "Theoretical and Numerical Studies on the Transport of Transverse Beam Quality in Plasma-Based Accelerators," Ph.D. dissertation, Universität Hamburg, 2014.

[36] L. Gorbunov, P. Mora, and T. M. Antonsen, Jr., "Magnetic Field of a Plasma Wake Driven by a Laser Pulse," *Phys. Rev. Lett.*, vol. 76, pp. 2495–2498, 1996. http://link.aps.org/doi/10.1103/PhysRevLett.76.2495

[37] R. Keinigs and M. E. Jones, "Two-dimensional dynamics of the plasma wakefield accelerator," *Phys. Fluids*, vol. 30, p. 252, 1987. http://dx.doi.org/10.1063/1.866183

[38] P. Sprangle, E. Esarey, and A. Ting, "Nonlinear theory of intense laser-plasma interactions," *Phys. Rev. Lett.*, vol. 64, pp. 2011–2014, 1990. http://link.aps.org/doi/10.1103/PhysRevLett.64.2011

[39] A. Friedman, R. H. Cohen, D. P. Grote, S. M. Lund, W. M. Sharp, J.-L. Vay, I. Haber, and R. A. Kishek, "Computational Methods in the Warp Code Framework for Kinetic Simulations of Particle Beams and Plasmas," *IEEE Trans. Plasma Sci.*, vol. 42, p. 1321, 2014. http://ieeexplore.ieee.org/xpl/articleDetails.jsp?arnumber=6774976

[40] E. Courant and H. Snyder, "Theory of the alternating-gradient synchrotron," *Annals of Physics*, vol. 3, no. 1, p. 1, 1958. http://www.sciencedirect.com/science/article/pii/0003491658900125

[41] F. Hinterberger, *Physik der Teilchenbeschleuniger und Ionenoptik*. Berlin: Springer-Verlag, 2008.

[42] G. Berden, W. A. Gillespie, S. P. Jamison, E.-A. Knabbe, A. M. MacLeod, A. F. G. van der Meer, P. J. Phillips, H. Schlarb, B. Schmidt, P. Schmüser, and B. Steffen, "Benchmarking of Electro-Optic Monitors for Femtosecond Electron Bunches," *Phys. Rev. Lett.*, vol. 99, p. 164801, 2007. http://link.aps.org/doi/10.1103/PhysRevLett.99.164801

[43] R. Pompili, A. Cianchi, D. Alesini, M. Anania, A. Bacci, M. Bellaveglia, M. Castellano, E. Chiadroni, D. D. Giovenale, G. D. Pirro, G. Gatti, F. Giorgianni, M. Ferrario, S. Lupi, F. Massimo, A. Mostacci, A. Rossi, C. Vaccarezza, and F. Villa, "First single-shot and non-intercepting longitudinal bunch diagnostics for comb-like beam by means of Electro-Optic Sampling," *Nucl. Instrum. Methods A*, vol. 740, p. 216, 2014. http://www.sciencedirect.com/science/article/pii/S0168900213013776

[44] S. I. Bajlekov, M. Heigoldt, A. Popp, J. Wenz, K. Khrennikov, S. Karsch, and S. M. Hooker, "Longitudinal electron bunch profile reconstruction by performing phase retrieval on coherent transition radiation spectra," *Phys. Rev. ST Accel. Beams*, vol. 16, p. 040701, 2013. http://link.aps.org/doi/10.1103/PhysRevSTAB.16.040701

[45] S. Bettoni, P. Craievich, A. A. Lutman, and M. Pedrozzi, "Temporal profile measurements of relativistic electron bunch based on wakefield generation," *Phys. Rev. Accel. Beams*, vol. 19, p. 021304, 2016. http://link.aps.org/doi/10.1103/PhysRevAccelBeams.19.021304

[46] P. Emma, J. Frisch, and P. Kejcik, "A transverse RF deflecting structure for bunch length and phase space diagnostics," *SLAC Report No. LCLS-TN-00-12*, 2000.

[47] M. Röhrs, C. Gerth, H. Schlarb, B. Schmidt, and P. Schmüser, "Time-resolved electron beam phase space tomography at a soft x-ray free-electron laser," *Phys. Rev. ST Accel. Beams*, vol. 12, p. 050704, 2009. http://link.aps.org/doi/10.1103/PhysRevSTAB.12.050704

[48] V. A. Dolgashev and J. Wang, "RF design of X-band RF deflector for femtosecond diagnostics of LCLS electron beam," *AIP Conference Proceedings*, vol. 1507, pp. 682–687, 2012. http://scitation.aip.org/content/aip/proceeding/aipcp/10.1063/1.4773780

[49] G. L. Orlandi, M. Aiba, F. Baerenbold, S. Bettoni, B. Beutner, H. Brands, P. Craievich, F. Frei, R. Ischebeck, M. Pedrozzi, E. Prat, T. Schietinger, and

V. Schlott, "Characterization of compressed bunches in the SwissFEL injector test facility," *Proceedings of IBIC2013, Oxford, UK*, p. TUPF08, 2013.

[50] K. Floettmann and V. V. Paramonov, "Beam dynamics in transverse deflecting rf structures," *Phys. Rev. ST Accel. Beams*, vol. 17, p. 024001, 2014. http://link.aps.org/doi/10.1103/PhysRevSTAB.17.024001

[51] I. Dornmair, C. B. Schroeder, K. Floettmann, B. Marchetti, and A. R. Maier, "Plasma-driven ultrashort bunch diagnostics," *Phys. Rev. Accel. Beams*, vol. 19, p. 062801, 2016. http://link.aps.org/doi/10.1103/PhysRevAccelBeams.19.062801

[52] C. Behrens and C. Gerth, "On the limitations of longitudinal phase space measurements using a transverse deflecting structure," *Proceedings of DIPAC2009, Basel, Switzerland*, p. TUPB44, 2009.

[53] B. Marchetti, R. W. Assmann, U. Dorda, J. Grebenyuk, and J. Zhu, "Compression of an electron-bunch by means of velocity bunching at ARES," *Proceedings of IPAC2015, Richmond, VA, USA*, p. TUPWA030, 2015. http://jacow.org/IPAC2015/papers/tupwa030.pdf

[54] B. Marchetti, private communication, 2015.

[55] K. Floettmann, "ASTRA - A Space Charge Tracking Algorithm," http://www.desy.de/∼mpyflo/. http://www.desy.de/~mpyflo/

[56] J.-L. Vay, "Noninvariance of Space- and Time-Scale Ranges under a Lorentz Transformation and the Implications for the Study of Relativistic Interactions," *Phys. Rev. Lett.*, vol. 98, p. 130405, Mar 2007. http://link.aps.org/doi/10.1103/PhysRevLett.98.130405

[57] C. B. Schroeder, private communication, 2015.

[58] S. Schulz, I. Grguraš, C. Behrens, H. Bromberger, J. T. Costello, M. K. Czwalinna, M. Felber, M. C. Hoffmann, M. Ilchen, H. Y. Liu, T. Mazza, M. Meyer, S. Pfeiffer, P. Prędki, S. Schefer, C. Schmidt, U. Wegner, H. Schlarb, and A. L. Cavalieri, "Femtosecond all-optical synchronization of an X-ray free-electron laser," *Nat. Commun.*, vol. 6, 2015. http://dx.doi.org/10.1038/ncomms6938

[59] M. B. Danailov, F. Bencivenga, F. Capotondi, F. Casolari, P. Cinquegrana, A. Demidovich, E. Giangrisostomi, M. P. Kiskinova, G. Kurdi, M. Manfredda, C. Masciovecchio, R. Mincigrucci, I. P. Nikolov, E. Pedersoli, E. Principi, and P. Sigalotti, "Towards jitter-free pump-probe measurements at seeded

free electron laser facilities," *Opt. Express*, vol. 22, no. 11, p. 12869, 2014. http://www.opticsexpress.org/abstract.cfm?URI=oe-22-11-12869

[60] G. Fubiani, E. Esarey, C. B. Schroeder, and W. P. Leemans, "Improvement of electron beam quality in optical injection schemes using negative plasma density gradients," *Phys. Rev. E*, vol. 73, p. 026402, 2006. http://link.aps.org/doi/10.1103/PhysRevE.73.026402

[61] http://regae.desy.de

[62] M. Hada, J. Hirscht, D. Zhang, S. Manz, K. Pichugin, D. Mazurenko, S. Bayesteh, H. Delsim-Hashemi, K. Floettmann, M. Huening, S. Lederer, G. Moriena, C. Mueller, G. Sciaini, and D. Miller, "REGAE: New Source for Atomically Resolved Dynamics," in *Hilas*, OSA, Washington, D.C., 2012, p. JT2A.47. http://www.osapublishing.org/abstract.cfm?URI=ICUSD-2012-JT2A.47

[63] S. Manz, A. Casandruc, D. Zhang, Y. Zhong, R. A. Loch, A. Marx, T. Hasegawa, L. C. Liu, S. Bayesteh, H. Delsim-Hashemi, M. Hoffmann, M. Felber, M. Hachmann, F. Mayet, J. Hirscht, S. Keskin, M. Hada, S. W. Epp, K. Flottmann, and R. J. D. Miller, "Mapping atomic motions with ultrabright electrons: towards fundamental limits in space-time resolution," *Faraday Discuss.*, vol. 177, pp. 467–491, 2015. http://dx.doi.org/10.1039/C4FD00204K

[64] M. Hachmann and K. Flöttmann, "Measurement of ultra low transverse emittance at REGAE," *Nucl. Instr. Meth. Phys. Res. A*, 2016. http://www.sciencedirect.com/science/article/pii/S0168900216000930

[65] B. Zeitler, K. Floettmann, and F. Grüner, "Linearization of the longitudinal phase space without higher harmonic field," *Phys. Rev. ST Accel. Beams*, vol. 18, 2015. http://link.aps.org/doi/10.1103/PhysRevSTAB.18.120102

[66] J. Maxson, D. Cesar, G. Calmasini, A. Ody, P. Musumeci, and D. Alesini, "Direct Measurement of Sub-10 fs Relativistic Electron Beams with Ultralow Emittance," *Phys. Rev. Lett.*, vol. 118, p. 154802, 2017. https://link.aps.org/doi/10.1103/PhysRevLett.118.154802

[67] T. Gehrke, "Design of Permanent Magnetic Solenoids for REGAE," Master's Thesis, University of Hamburg, Germany, Jul. 2013.

[68] W. Rittershofer, C. B. Schroeder, E. Esarey, F. J. Grüner, and W. P. Leemans, "Tapered plasma channels to phase-lock accelerating and focusing forces in laser-plasma accelerators," *Physics of Plasmas*, vol. 17, no. 6, p. 063104, 2010. http://scitation.aip.org/content/aip/journal/pop/17/6/10.1063/1.3430638

[69] T. Mehrling, J. Grebenyuk, F. S. Tsung, K. Floettmann, and J. Osterhoff, "Transverse emittance growth in staged laser-wakefield acceleration," *Phys. Rev. ST. Accel. Beams*, vol. 15, p. 111303, 2012. http://dx.doi.org/10.1103/PhysRevSTAB.15.111303

[70] G. R. Plateau, C. G. R. Geddes, D. B. Thorn, M. Chen, C. Benedetti, E. Esarey, A. J. Gonsalves, N. H. Matlis, K. Nakamura, C. B. Schroeder, S. Shiraishi, T. Sokollik, J. van Tilborg, C. Toth, S. Trotsenko, T. S. Kim, M. Battaglia, T. Stöhlker, and W. P. Leemans, "Low-Emittance Electron Bunches from a Laser-Plasma Accelerator Measured using Single-Shot X-Ray Spectroscopy," *Phys. Rev. Lett.*, vol. 109, p. 064802, 2012. http://link.aps.org/doi/10.1103/PhysRevLett.109.064802

[71] R. Weingartner, S. Raith, A. Popp, S. Chou, J. Wenz, K. Khrennikov, M. Heigoldt, A. R. Maier, N. Kajumba, M. Fuchs, B. Zeitler, F. Krausz, S. Karsch, and F. Grüner, "Ultra-low emittance electron beams from a laser-wakefield accelerator," *Phys. Rev. ST. Accel. Beams*, vol. 15, p. 111302, 2012. http://dx.doi.org/10.1103/PhysRevSTAB.15.111302

[72] T. Eichner, F. Grüner, S. Becker, M. Fuchs, D. Habs, R. Weingartner, U. Schramm, H. Backe, P. Kunz, and W. Lauth, "Miniature magnetic devices for laser-based, table-top free-electron lasers," *Phys. Rev. ST Accel. Beams*, vol. 10, p. 082401, 2007. http://link.aps.org/doi/10.1103/PhysRevSTAB.10.082401

[73] J. van Tilborg, S. Steinke, C. G. R. Geddes, N. H. Matlis, B. H. Shaw, A. J. Gonsalves, J. V. Huijts, K. Nakamura, J. Daniels, C. B. Schroeder, C. Benedetti, E. Esarey, S. S. Bulanov, N. A. Bobrova, P. V. Sasorov, and W. P. Leemans, "Active plasma lensing for relativistic laser-plasma-accelerated electron beams," *Phys. Rev. Lett.*, vol. 115, p. 184802, 2015. http://link.aps.org/doi/10.1103/PhysRevLett.115.184802

[74] W. K. H. Panofsky and W. R. Baker, "A Focusing Device for the External 350-MeV Proton Beam of the 184-Inch Cyclotron at Berkeley," *Review of Scientific Instruments*, vol. 21, no. 5, p. 445, 1950. http://scitation.aip.org/content/aip/journal/rsi/21/5/10.1063/1.1745611

[75] R. Lehe, C. Thaury, E. Guillaume, A. Lifschitz, and V. Malka, "Laser-plasma lens for laser-wakefield accelerators," *Phys. Rev. ST Accel. Beams*, vol. 17, p. 121301, 2014. http://link.aps.org/doi/10.1103/PhysRevSTAB.17.121301

[76] C. Thaury, E. Guillaume, A. Döpp, R. Lehe, A. Lifschitz, K. Ta Phuoc, J. Gautier, J.-P. Goddet, A. Tafzi, A. Flacco, F. Tissandier, S. Sebban, A. Rousse, and V. Malka, "Demonstration of relativistic electron beam

focusing by a laser-plasma lens," *Nat. Commun.*, vol. 6, p. 6860, 2015. http://dx.doi.org/10.1038/ncomms7860

[77] G. Hairapetian, P. Davis, C. E. Clayton, C. Joshi, S. C. Hartman, C. Pellegrini, and T. Katsouleas, "Experimental demonstration of dynamic focusing of a relativistic electron bunch by an overdense plasma lens," *Phys. Rev. Lett.*, vol. 72, p. 2403, 1994. http://link.aps.org/doi/10.1103/PhysRevLett.72.2403

[78] R. Govil, W. P. Leemans, E. Y. Backhaus, and J. S. Wurtele, "Observation of Return Current Effects in a Passive Plasma Lens," *Phys. Rev. Lett.*, vol. 83, p. 3202, 1999. http://link.aps.org/doi/10.1103/PhysRevLett.83.3202

[79] S. Kuschel, D. Hollatz, T. Heinemann, O. Karger, M. B. Schwab, D. Ullmann, A. Knetsch, A. Seidel, C. Rödel, M. Yeung, M. Leier, A. Blinne, H. Ding, T. Kurz, D. J. Corvan, A. Sävert, S. Karsch, M. C. Kaluza, B. Hidding, and M. Zepf, "Demonstration of passive plasma lensing of a laser wakefield accelerated electron bunch," *Phys. Rev. Accel. Beams*, vol. 19, p. 071301, 2016. http://link.aps.org/doi/10.1103/PhysRevAccelBeams.19.071301

[80] I. Dornmair, K. Floettmann, and A. R. Maier, "Emittance conservation by tailored focusing profiles in a plasma accelerator," *Phys. Rev. ST Accel. Beams*, vol. 18, p. 041302, 2015. http://link.aps.org/doi/10.1103/PhysRevSTAB.18.041302

[81] P. Antici, A. Bacci, C. Benedetti, E. Chiadroni, M. Ferrario, A. R. Rossi, L. Lancia, M. Migliorati, A. Mostacci, L. Palumbo, and L. Serafini, "Laser-driven electron beamlines generated by coupling laser-plasma sources with conventional transport systems," *Journal of Applied Physics*, vol. 112, p. 044902, 2012. http://scitation.aip.org/content/aip/journal/jap/112/4/10.1063/1.4740456

[82] K. Wille, *Physik der Teilchenbeschleuniger und Synchrotronstrahlungsquellen.* Stuttgart: B. G. Teubner, 1996.

[83] M. Migliorati, A. Bacci, C. Benedetti, E. Chiadroni, M. Ferrario, A. Mostacci, L. Palumbo, A. R. Rossi, L. Serafini, and P. Antici, "Intrinsic normalized emittance growth in laser-driven electron accelerators," *Phys. Rev. ST. Accel. Beams*, vol. 16, p. 011302, 2013. http://dx.doi.org/10.1103/PhysRevSTAB.16.011302

[84] R. Assmann and K. Yokoya, "Transverse beam dynamics in plasma-based linacs," *Nucl. Instrum. Meth. A*, vol. 410, p. 544, 1998. http://dx.doi.org/10.1016/S0168-9002(98)00187-9

[85] C. M. S. Sears, A. Buck, K. Schmid, J. Mikhailova, F. Krausz, and L. Veisz, "Emittance and divergence of laser wakefield accelerated electrons," *Phys. Rev. ST. Accel. Beams*, vol. 13, p. 092803, 2010. http://dx.doi.org/10.1103/PhysRevSTAB.13.092803

[86] K. Floettmann, "Adiabatic matching section for plasma accelerated beams," *Phys. Rev. ST. Accel. Beams*, vol. 17, p. 054402, 2014. http://dx.doi.org/10.1103/PhysRevSTAB.17.054402

[87] R. Lehe, M. Kirchen, I. A. Andriyash, B. B. Godfrey, and J.-L. Vay, "A spectral, quasi-cylindrical and dispersion-free Particle-In-Cell algorithm," *Comput. Phys. Comm.*, vol. 203, p. 66, 2016. http://www.sciencedirect.com/science/article/pii/S0010465516300224

[88] R. Courant, K. Friedrichs, and H. Lewy, "Über die partiellen Differenzengleichungen der mathematischen Physik," *Mathematische Annalen*, vol. 100, no. 1, pp. 32–74, 1928. http://dx.doi.org/10.1007/BF01448839

[89] B. B. Godfrey, "Numerical Cherenkov instabilities in electromagnetic particle codes," *Journal of Computational Physics*, vol. 15, no. 4, p. 504, 1974. http://www.sciencedirect.com/science/article/pii/002199917490076X

[90] B. B. Godfrey, "Canonical momenta and numerical instabilities in particle codes," *Journal of Computational Physics*, vol. 19, no. 1, p. 58, 1975. http://www.sciencedirect.com/science/article/pii/0021999175901163

[91] B. B. Godfrey and J.-L. Vay, "Numerical stability of relativistic beam multidimensional PIC simulations employing the Esirkepov algorithm," *Journal of Computational Physics*, vol. 248, p. 33, 2013. http://www.sciencedirect.com/science/article/pii/S0021999113002556

[92] X. Xu, P. Yu, S. F. Martins, F. S. Tsung, V. K. Decyk, J. Vieira, R. A. Fonseca, W. Lu, L. O. Silva, and W. B. Mori, "Numerical instability due to relativistic plasma drift in EM-PIC simulations," *Computer Physics Communications*, vol. 184, no. 11, p. 2503, 2013. http://www.sciencedirect.com/science/article/pii/S0010465513002312

[93] J.-L. Vay, C. G. R. Geddes, C. Benedetti, D. L. Bruhwiler, E. Cormier-Michel, B. M. Cowan, J. R. Cary, and D. P. Grote, "Modeling Laser Wakefield Accelerators in a Lorentz Boosted Frame," *AIP Conference Proceedings*, vol. 1299, no. 1, p. 244, 2010. http://scitation.aip.org/content/aip/proceeding/aipcp/10.1063/1.3520322

[94] S. F. Martins, R. A. Fonseca, L. O. Silva, W. Lu, and W. B. Mori, ""numerical simulations of laser wakefield accelerators in optimal lorentz frames"," *Computer Physics Communications*, vol. 181, no. 5, pp. 869 – 875, 2010. http://www.sciencedirect.com/science/article/pii/S0010465509004159

[95] J.-L. Vay, C. G. R. Geddes, E. Cormier-Michel, and D. P. Grote, "Numerical methods for instability mitigation in the modeling of laser wakefield accelerators in a Lorentz-boosted frame," *Journal of Computational Physics*, vol. 230, no. 15, p. 5908, 2011. http://www.sciencedirect.com/science/article/pii/S0021999111002270

[96] J.-L. Vay, C. G. R. Geddes, E. Cormier-Michel, and D. P. Grote, "Effects of hyperbolic rotation in Minkowski space on the modeling of plasma accelerators in a Lorentz boosted frame," *Physics of Plasmas*, vol. 18, no. 3, p. 030701, 2011. http://scitation.aip.org/content/aip/journal/pop/18/3/10.1063/1.3559483

[97] P. Yu, X. Xu, V. K. Decyk, F. Fiuza, J. Vieira, F. S. Tsung, R. A. Fonseca, W. Lu, L. O. Silva, and W. B. Mori, "Elimination of the numerical Cerenkov instability for spectral EM-PIC codes," *Computer Physics Communications*, vol. 192, pp. 32 – 47, 2015. http://www.sciencedirect.com/science/article/pii/S0010465515000752

[98] P. Yu, X. Xu, A. Tableman, V. K. Decyk, F. S. Tsung, F. Fiuza, A. Davidson, J. Vieira, R. A. Fonseca, W. Lu, L. O. Silva, and W. B. Mori, "Mitigation of numerical Cerenkov radiation and instability using a hybrid finite difference-FFT Maxwell solver and a local charge conserving current deposit," *Computer Physics Communications*, vol. 197, pp. 144 – 152, 2015. http://www.sciencedirect.com/science/article/pii/S0010465515003252

[99] F. Li, P. Yu, X. Xu, F. Fiuza, V. K. Decyk, T. Dalichaouch, A. Davidson, A. Tableman, W. An, F. S. Tsung, R. A. Fonseca, W. Lu, and W. B. Mori, "Controlling the Numerical Cerenkov Instability in PIC simulations using a customized finite difference Maxwell solver and a local FFT based current correction," *arXiv:1605.01496*, 2016. https://arxiv.org/abs/1605.01496

[100] M. Kirchen, "Parallelization of a spectral, quasi-cylindrical Particle-In-Cell code," Master's Thesis, University of Hamburg, Germany, Sep. 2015.

[101] A. F. Lifschitz, X. Davoine, E. Lefebvre, J. Faure, C. Rechatin, and V. Malka, "Particle-In-Cell modelling of laser-plasma interaction using Fourier decomposition," *J. Comput. Phys.*, vol. 228, p. 1803, 2008. http://www.sciencedirect.com/science/article/pii/S0021999108005950

[102] M. Kirchen, R. Lehe, B. B. Godfrey, I. Dornmair, S. Jalas, K. Peters, J.-L. Vay, and A. R. Maier, "Stable discrete representation of relativistically drifting plasmas," *Physics of Plasmas*, vol. 23, no. 10, p. 100704, 2016. http://scitation.aip.org/content/aip/journal/pop/23/10/10.1063/1.4964770

[103] R. Lehe, M. Kirchen, B. B. Godfrey, A. R. Maier, and J.-L. Vay, "Elimination of numerical Cherenkov instability in flowing-plasma particle-in-cell simulations by using Galilean coordinates," *Phys. Rev. E*, vol. 94, p. 053305, 2016. http://link.aps.org/doi/10.1103/PhysRevE.94.053305

[104] A. Buck, J. Wenz, J. Xu, K. Khrennikov, K. Schmid, M. Heigoldt, J. M. Mikhailova, M. Geissler, B. Shen, F. Krausz, S. Karsch, and L. Veisz, "Shock-Front Injector for High-Quality Laser-Plasma Acceleration," *Phys. Rev. Lett.*, vol. 110, p. 185006, 2013. http://link.aps.org/doi/10.1103/PhysRevLett.110.185006

[105] P. Tomassini and A. R. Rossi, "Matching strategies for a plasma booster," *Plasma Phys. Control. Fusion*, vol. 58, p. 034001, 2016. http://stacks.iop.org/0741-3335/58/i=3/a=034001

[106] J.-L. Vay, C. G. R. Geddes, C. B. Schroeder, E. Esarey, and W. P. Leemans, "Beam emittance conservation in multiple consecutive laser-plasma accelerator stages," *AIP Conference Proceedings*, vol. 1777, no. 1, p. 040018, 2016. http://scitation.aip.org/content/aip/proceeding/aipcp/10.1063/1.4965620

[107] X. L. Xu, J. F. Hua, Y. P. Wu, C. J. Zhang, F. Li, Y. Wan, C.-H. Pai, W. Lu, W. An, P. Yu, M. J. Hogan, C. Joshi, and W. B. Mori, "Physics of Phase Space Matching for Staging Plasma and Traditional Accelerator Components Using Longitudinally Tailored Plasma Profiles," *Phys. Rev. Lett.*, vol. 116, p. 124801, 2016. http://link.aps.org/doi/10.1103/PhysRevLett.116.124801

[108] T. Katsouleas, S. Wilks, P. Chen, J. M. Dawson, and J. J. Su, "Beam Loading in Plasma Accelerators," *Particle Accelerators*, vol. 22, p. 81, 1987.

[109] T. C. Chiou and T. Katsouleas, "High Beam Quality and Efficiency in Plasma-Based Accelerators," *Phys. Rev. Lett.*, vol. 81, p. 3411, 1998. http://link.aps.org/doi/10.1103/PhysRevLett.81.3411

[110] J. Faure, B. van der Geer, B. Beaurepaire, G. Gallé, A. Vernier, and A. Lifschitz, "Concept of a laser-plasma-based electron source for sub-10-fs electron diffraction," *Phys. Rev. Accel. Beams*, vol. 19, p. 021302, 2016. http://link.aps.org/doi/10.1103/PhysRevAccelBeams.19.021302

[111] R. Brinkmann, N. Delbos, I. Dornmair, M. Kirchen, R. Assmann, C. Behrens, K. Floettmann, J. Grebenyuk, M. Gross, S. Jalas, T. Mehrling, A. M. de la Ossa, J. Osterhoff, B. Schmidt, V. Wacker, and A. R. Maier, "Chirp mitigation of plasma-accelerated beams using an alternating-focusing scheme," 2017, accepted for publication at Phys. Rev. Lett.

[112] M. J. Nasse, A. Bernhard, I. Birkel, A. Böhm, A. Borysenko, S. Hillenbrand, N. Hiller, S. Höninger, S. Marsching, A.-S. Müller, R. Rossmanith, R. Ruprecht, M. Schuh, M. Schwarz, B. Smit, S. Walther, M. Weber, P. Wesolowski, R. W. Assmann, M. Felber, K. Floettmann, C. Gerth, P. Peier, H. Schlarb, B. Steffen, R. Ischebeck, B. Keil, V. Schlott, and L. Stingelin, "Status of the Accelerator Test Facility FLUTE," in *Proceedings of IPAC2015, Richmond, VA, USA*, 2015, TUPWA042.

[113] J. Zhu, R. W. Assmann, M. Dohlus, U. Dorda, and B. Marchetti, "Sub-fs electron bunch generation with sub-10-fs bunch arrival-time jitter via bunch slicing in a magnetic chicane," *Phys. Rev. Accel. Beams*, vol. 19, p. 054401, 2016. http://link.aps.org/doi/10.1103/PhysRevAccelBeams.19.054401

[114] OpenFOAM. http://www.openfoam.org

[115] Y. Ehrlich, C. Cohen, A. Zigler, J. Krall, P. Sprangle, and E. Esarey, "Guiding of high intensity laser pulses in straight and curved plasma channel experiments," *Phys. Rev. Lett.*, vol. 77, pp. 4186–4189, 1996. http://link.aps.org/doi/10.1103/PhysRevLett.77.4186

[116] D. J. Spence and S. M. Hooker, "Investigation of a hydrogen plasma waveguide," *Phys. Rev. E*, vol. 63, p. 015401, 2000. http://link.aps.org/doi/10.1103/PhysRevE.63.015401

[117] E. Cormier-Michel, E. Esarey, C. G. R. Geddes, C. B. Schroeder, K. Paul, P. J. Mullowney, J. R. Cary, and W. P. Leemans, "Control of focusing fields in laser-plasma accelerators using higher-order modes," *Phys. Rev. ST Accel. Beams*, vol. 14, p. 031303, 2011. http://link.aps.org/doi/10.1103/PhysRevSTAB.14.031303

[118] H. Delsim-Hashemi, "Single Shot Transversal Profile Monitoring of Ultra Low Charge Relativistic Electron Bunches at REGAE," *Proceedings of IBIC2016, Barcelona, Spain*, p. MOPG75, 2016.

Acknowledgments

Surely this thesis would not have been possible without the support and encouragement offered by many people.

I'd like to express my gratitude to my doctoral supervisor, **Prof. Florian Grüner**, who recruited me in the first place – what feels like a long time ago back in Munich – and later gave me the opportunity to join his new group here in Hamburg for the PhD. He was always an inspiration, regarding physical insight, but also owing to his seemingly inexhaustible energy.
I'd also like to thank my doctoral supervisor and adviser **Dr. Klaus Floettmann** for answering my countless questions, and for many fruitful discussions over cake. Special thanks also for patiently bearing with me and my peculiar ideas when implementing the linear wakefield model in ASTRA, which has proven an invaluable tool for countless ultrafast estimates.
Dr. Andreas Maier, as my more direct adviser, always pushed me in the right direction. With his physical understanding and sheer hard work he was a constant source of motivation. With his optimism and enthusiasm he keeps the team together.
Furthermore, I'd like to thank **Prof. Kwang-Je Kim** for agreeing to examine my thesis, and not least also for finding the hopefully last and now removed flaws.
I had the pleasure to receive priceless advice from **Dr. Carl B. Schroeder** on the TDP project. Also, he hosted me for a short and very enjoyable stay at LBNL in Berkeley. I learned a lot.
I am indebted to **Dr. Jean-Luc Vay** for patiently answering questions on PIC codes in general and on WARP more specifically, which is a truly universal plasma simulations tool. The same is true for **Dr. Rémi Lehe** and **Manuel Kirchen**, developers of FBPIC (a.k.a. SpyderPIC). I'm still stunned by how fast this code is.
Dr. Reinhard Brinkmann triggered the project on the modulated plasma density by providing the initial idea. With his expertise on and his experience from what plasma people like to call "conventional" accelerators, he fostered the further investigation of this idea.
Special thanks go to my fellow laser plasma theoreticians and PIC developers here in Hamburg, **Manuel Kirchen**, **Sören Jalas** and **Kevin Peters**. I enjoyed countless coffee-enhanced discussions not only on physics and algorithms. I'd also like to thank

Arne Müller and **Lukas Broers**, who had the courage to join our little theory group as Bachelor students.
The **members (and friends) of the LUX group** made the last few years a very enjoyable time. Taking the risk of forgetting somebody, I'd like to mention in no specific order Benno Zeitler, Niels Delbos, Chris Werle, Matthias Schnepp, Spencer Jolly, Vincent Leroux, Andreas Walker, Max Trunk, Paul Winkler, Philipp Messner, Theresa Brümmer, Mikheil Titberidze, Max Hachmann, Henning Groth, Nils Plambeck, Vaclav Hanus, Hannes Wittern and Martin Stieben. Thank you for funny, fruitful, rich, and thoughtful discussions over coffee (and cake). Without you, this whole encounter would not nearly have been as much fun. And also, I learned a lot from you guys.
Without our team assistants **Fenna Reinhold** and **Heike Kaminski** this bunch of physicists would surely be lost. Thank you.
Furthermore, I am grateful to the **IMPRS UFAST** graduate school for offering great courses and for providing a platform to get in touch with the many excellent PhD students working at CFEL.
Finally, I'd like to thank **my parents and family** for their constant support and confidence, and I'd like to thank Janos, for following me to this sometimes dark, but always windy city.

I'd like to gratefully acknowledge the computing time provided on the supercomputers **Jureca** and formerly **Juropa** under project HHH20.